THESIS FOR THE DEGREE OF DOCTOR OF PHILOSOPHY

Hybrid organic-inorganic nanomaterials for applications at the biointerfaces

Patrizia Di Pietro

Supervisor: Prof. Cristina Satriano

PhD Coordinator: Prof. Salvatore Sortino

Department of Chemical Sciences

University of Catania

Catania, Italy, December 2016

Hybrid organic-inorganic nanomaterials for applications at the biointerfaces

Patrizia Di Pietro

Abstract

In the last few years, the application of nanomaterials (NMs) as theranostic devices, which combine diagnostic and therapeutic features, has gained a tremendous interest and development. Still, the major challenge is the understanding of the many and often complex processes that occur during the interaction of biological compounds with nanomaterials, in order to modulate their responses to the fixed target. A fine development of such smart nanosystems could occur only by a critical control of chemical/physical properties of NMs at the biological interfaces.

According to such premises, this thesis deals with the investigation of NMs at the biointerfaces for potential theranostic applications. Specifically, the work has been addressed to the synthesis and characterization of several inorganic and organic nanomaterials, including gold and silver nanoparticles, hydroxyapatite, graphene and graphene oxide nanosheets tailored at the surface with stimuli-responsive polymers (polyacrylate and/or polyacrylamide) or specific chemical functionalities (amine functionalisation, sulphur functionalisation). As to the biomolecular counterpart, the performed study involved proteins (ferritin and albumin), drugs

(curcumin), peptides mimicking proteins of relevant biomedical interest (such as RGD - the cell adhesive sequence of several extracellular matrix proteins-, neurotrophin peptides, fragments of the vascular endothelial growth factor), artificial membranes (lipid liposomes and supported lipid bilayers), and cells (neuroblastoma, endothelial cells, retinal pigment epithelial cells).

The hybrid nano-bio-interface between the chosen NMs and biomolecules was scrutinized by a multi-technique approach, which relies on various physico-chemical spectroscopic (UV-visible, FT-IR, RAMAN, X-ray photoelectron spectroscopy), microscopic (atomic force microscopy, scanning electron microscopy, transmission electron microscopy, laser scanning confocal microscopy) and spectrometric (Time-of-Flight secondary ion mass spectrometry) methods. The research methodology used was interdisciplinary as well as the performed research, also including some biological assays on cell viability, nanoparticle internalisation by cellular uptake and nanotoxicity.

The obtained results suggest promising applications for further development of these smart nanosystems for theranostic purposes.

Keywords: theranostics, hybrid bio-nanointerface, metallic nanoparticle, graphene, lipid bilayers, peptides

Dissemination activities

The results of three years of Ph.D. activity are reported in the manuscripts and oral/poster presentations* listed below.

Oral presentations:

1) **Polymer-modified Graphene Oxide For Sensing and Drug Delivery Application.**
   Cristina Satriano, Patrizia Di Pietro, Giuseppe Consiglio, Giuseppe Forte, Giuseppe Grasso, Carmelo Sgarlata, and Luisa D'Urso. *XLIV Congresso della Divisione di Chimica Fisica della SCI.* Napoli, 20-23 September, 2016.

2) **A ToF-SIMS study of graphene oxide functionalization for biosensing and drug delivery applications.**
   Patrizia Di Pietro, Damien Cossement, Luisa D'Urso, Giuseppe Consiglio, Carla Bittencourt, Rony Snyders, Cristina Satriano. *Réunion francophone ION-TOF des utilisateurs ToF-SIMS*. Mons (Belgium), 9-10 March 2016.

* The underlined name stands for presenting author.

3) **Multi-functionalization of graphene oxide for sensing application.**
Alessandro Catanzaro, Patrizia Di Pietro, Luisa D'Urso, Giuseppe Consiglio, Giuseppe Forte, Giuseppe Grasso, Carmelo Sgarlata, Thomas Godfroid, Rony Snyders, Cristina Satriano.
FisMat2015. Palermo (Italy), 28 September – 02 October 2015.

4) **Neurotrophin-mimicking peptides and gold nanoparticles: two different immobilization approaches for controlled interaction with cells.**
Patrizia Di Pietro, Giuseppe Pandini, Alessio Travaglia, Antonio Magrì, Diego La Mendola, Cristina Satriano, Enrico Rizzarelli. *E-MRS 2015 Spring Meeting*. Lille (France), 11-15 May 2015.

5) **Supported lipid bilayer-driven nanoparticle cellular uptake for theranostic applications.**
Lidia Zuccarello, Patrizia Di Pietro, Enrico Rampazzo, Massimo Sgarzi, Luca Prodi, Enrico Rizzarelli, Cristina Satriano. *E-MRS 2015 Spring Meeting.* Lille (France), 11-15 May 2015.

6) ***Functionalized Graphene Oxide*** **for theranostics applications.**
Cristina Satriano, Patrizia Di Pietro, Luisa D'Urso, Giuseppe Compagnini, Giuseppe Forte.
E-MRS 2014 Spring Meeting. Lille (France), 26-30 May 2014.

Poster presentations:

1) **The functionalisation of hydroxyapatite nanocrystals by pro- and anti-angiogenic peptide fragments.**
Patrizia Di Pietro, Rosario Alemanni, Giulia Grasso, Cristina Satriano, Marco Lelli, Norberto Roveri, Diego La Mendola, Enrico Rizzarelli. *BIOMET 2016*. 28-29 October 2016.

2) **Stimuli-responsive polymer-modified graphene oxide as versatile platform for (bio)sensing.**
Carmelo Sgarlata, Giuseppe Consiglio, Luisa D'Urso, Patrizia Di Pietro, Giuseppe Forte, Giuseppe Grasso, Cristina Satriano. *XXVI Congresso della Divisione di Chimica Analitica della Società Chimica Italiana*. Giardini, 18-22 September 2016.

3) **Plasma sulphur-functionalized graphene oxide/metallic nanoparticles nanoassemblies for the immobilization of biomolecules.**
Patrizia Di Pietro, Damien Thiry, Thomas Godfroid, Rony Snyders, Cristina Satriano, Carla Bittencourt. *ChemOnTubes 2016*. Brussels, 3-7 April 2016.

4) **Lipid wrapped polymeric cyclodextrin nanoparticles for encapsulation of curcumin and smart delivery to cells.**
Lidia Zuccarello, Patrizia Di Pietro, Francesco Bellia, Graziella Vecchio, Elena Solfato, Anna Rita Blanco, Cristina Satriano. *FisMat2015*. Palermo (Italy), 28 September – 02 October 2015.

5) **Plasma functionalization of gold nanoparticle for biosensing application.**
   Vittorio Ferrara, Patrizia Di Pietro, Cèdric Vandenabeele, Rony Snyders, Cristina Satriano.
   FisMat2015. Palermo (Italy), 28 September – 02 October 2015.

6) **Multi-Stimuli Responsive Graphene Oxide For Sensing Application.**
   Giuseppe Consiglio, Patrizia Di Pietro, Giuseppe Forte, Giuseppe Grasso, Carmelo Sgarlata, Cristina Satriano, Luisa D'Urso. *GraphITA 2015*. CNR Bologna (Italy), 14-18 September 2015.

7) **Amino-Functionalized Graphene Oxide for drug delivery applications.**
   Patrizia Di Pietro, Giuseppe Forte, Alessandro Catanzaro, Thomas Godfroid, Rony Snyders, Giuseppe Compagnini, Luisa D'Urso, Cristina Satriano. *GraphITA 2015*. CNR Bologna (Italy), 14-18 September 2015.

8) **Multi stimuli-responsive grafene oxide for biosensing application.**
   Luisa D'Urso, Giuseppe Consiglio, Giuseppe Forte, Giuseppe Grasso, Carmelo Sgarlata, Patrizia Di Pietro, Cristina Satriano. *E-MRS 2015 Spring Meeting*. Lille (France), 11-15 May 2015.

9) **Graphene–Derivatives Prepared By Chemical And Physical Approaches For Investigation At The Biointerfaces With Artificial Membranes.**
Patrizia Di Pietro, Luisa D'Urso, Giuseppe Forte and Cristina Satriano. *XXV Congresso Nazionale della Società Chimica Italiana (SCI 2014)*. Rende (CS), 7 - 12 September 2014.

10) **The adsorption of neurotrophin-derived peptides on gold surfaces: the pH and copper effect.**
Cristina Satriano, Patrizia Di Pietro, Alessio Travaglia, Antonio Magrì, Diego La Mendola, Enrico Rizzarelli.
Euro AFM Forum 2014. Göttingen (Germany), 17-19 March 2014.

Manuscripts (published or in preparation) included in this thesis:

PAPER I

Neurotrophin-mimicking peptides at the biointerface with gold respond to copper ions stimuli.

C. Satriano, G. Forte, A. Magrì, P. Di Pietro, A. Travaglia, G. Pandini, F. Gianì, D. La Mendola. *Phys. Chem. Chem. Phys.* 2016, 18, 30595-30604.

PAPER II

Lipid bilayer-mediated immobilisation of neurotrophin peptides on gold nanoparticles: a new multipotential therapeutic nanoplatform for CNS disorders.

P. Di Pietro, N. Caporarello, C. D. Anfuso, G. Lupo, A. Magrì, D. La Mendola, C. Satriano. [Submitted to Chem. Comm.]

PAPER III

The balance of pro-/anti-angiogenic properties of gold nanoparticles functionalised with a VEGF peptide.

P. Di Pietro, S. Zimbone, G. Grasso, C. Satriano [in preparation for submission to Acta Biomaterialia].

PAPER IV

Silver nanoparticles functionalized with a fluorescent cyclic RGD peptide: a versatile integrin targeting platform for cells and bacteria.

P. Di Pietro, L. Zaccaro, D. Comegna, A. Del Gatto, M. Saviano, R. Snyders, D. Cossement, C. Satriano, E. Rizzarelli. *RSC Adv*. 2016, 6, 112381-112392.

PAPER V

The hybrid nanobiointerface between amine-functionalized graphene oxide and lipid membranes: a theoretical and experimental study.

P. Di Pietro, G. Forte, L. D'Urso, C. Satriano. *Special topic "Graphene" - AIMS Materials Science* 2017, 4(1), 43-60.

PAPER VI

Lateral-size controlled graphene oxide functionalised by polyacrylate grafting: an experimental and theoretical study for applications in theranostics.

P. Di Pietro, G. Consiglio, L. D'Urso, G. Forte, G. Grasso, C. Sgarlata, D. Cossement, R. Snyders, C. Satriano. [submitted to RSC Advances]

PAPER VII

Gold and Silver Nanoparticles for Applications in Theranostics. *Review*

P. Di Pietro, G. Strano, L. Zuccarello, C. Satriano.
Curr. Top. Med. Chem., 2016, 16 (27), 3069-3102.

Manuscripts (published or in preparation) not included in this thesis:

1) Ferritin-supported lipid bilayers for triggering the endothelial cell response.

C. Satriano, G. Lupo, C. Motta, C.D. Anfuso, P. Di Pietro, B. Kasemo.
Colloids and Surfaces B: Biointerfaces, 2017, 149, 48-55.

2) Sulphur functionalization of graphene oxide by radiofrequency plasma.
P. Di Pietro, L. D'Urso, G. Consiglio, G. Forte, C. Sgarlata, G. Grasso, D. Thiry, R. Snyders, C. Bittencourt, C. Satriano. [in preparation for submission to Carbon]

3) Curcumin-loaded cyclodextrin nanoparticles for intracellular drug delivery.
L. Cucci, A.R. Blanco, L.R. La Rosa, L. Zuccarello, P. Di Pietro, F. Bellia, C. Satriano, G. Vecchio. [in preparation]

4) Nanohydroxyapatite functionalised by pro- and anti-angiogenic peptide fragments.
P. Di Pietro, R. Alemanni, G. Grasso, C. Satriano, M. Lelli, N. Roveri, D. La Mendola, E. Rizzarelli. [in preparation for submission to Acta Biomaterialia].

Table of Contents

1. Introduction

1.1 Overview and aim of this work

In last few years, nanoscience and nanotechnology have raised significant developments thanks to the availability of new strategies for the synthesis of nanomaterials (NMs) and new tools for characterizations and manipulations at the nano- and micro-meter scale. The "unique properties" of NMs, which depend on their small sizes, arise a tremendous interest for applications in many different science fields, *e.g.*, physics, chemistry, biology and medicine.

The application of nanotechnology to diseases treatment, diagnosis, monitoring, and to the control of biological systems has recently been referred to as "nanomedicine".[1] Modern NMs-based biomedical applications that combine both "imaging" and "therapeutic" aspects are recognized as "theranostic" NMs.[2] Since the new term "theranostic" was coined in 2002 by Funkhouser,[3] it has been increasingly recognized as a promising approach for a variety of oncological, cardiovascular, dermatological, and ophthalmic diseases.

However, the major challenge is the understanding of processes involved during the interaction of biological compounds with NMs and to modulate their responses to reach the fixed purpose.

A fine development of such smart nanosystems could occur only by a critical control of chemical/physical properties of NMs at the biological interfaces.

According to such premises, the aim of this thesis work is the investigation of NMs at the biointerface for potential theranostic applications. Specifically, the research and study activity has been addressed to the synthesis and characterization of different nanomaterials belonging to the two wide classes of inorganic (metal gold and silver colloids - chapter 2) and organic (graphene and its derivatives - chapter 3) nanoparticles. This study involved the use of different biomolecules, including peptides mimicking proteins of relevant biomedical interest, *e.g.*, neurotrophic factors (Nerve Growth Factor, NGF, and Brain Derived Neurotrophic Factor, BDNF) and growth factors (Vascular Endothelial Growth Factor, VEGF), the cell adhesive Arg-Gly-Asp (RGD) peptide selective for integrins, model proteins (human serum albumin, HSA) and drugs (curcumin) as well as artificial biomembranes that mimic the cell membrane (e.g., lipid vesicles and solid-supported lipid bilayers). The hybrid nano-bio-interface between the chosen NMs and biomolecules was scrutinized by a multi-technique approach, which relies on various physic-chemical characterization methods such as spectroscopic (UV, FT-IR, RAMAN, XPS), microscopic (AFM and Confocal fluorescence) and a surface sensitive techniques as ToF-SIMS.

This introductive chapter aims to review the NM properties particularly focusing at the biointerfaces (Chapter 1). Chapter 2 widely discuss on the metallic nanoparticles as gold and silver, and finally Chapter 3 give a description of organic nanomaterials here afforded, the graphene and its derivatives

2. Nanomaterials at the biointerfaces

NMs are defined as small materials having at least one of the three dimensions. According to Siegel, [4] nanostructured materials are classified as Zero dimensional (0-D), one dimensional (1-D), two dimensional (2-D), three-dimensional (3-D) nanostructures depending on their morphologies: single, fused, aggregated or agglomerated forms with spherical, tubular, and irregular shapes, respectively (Figure 1).

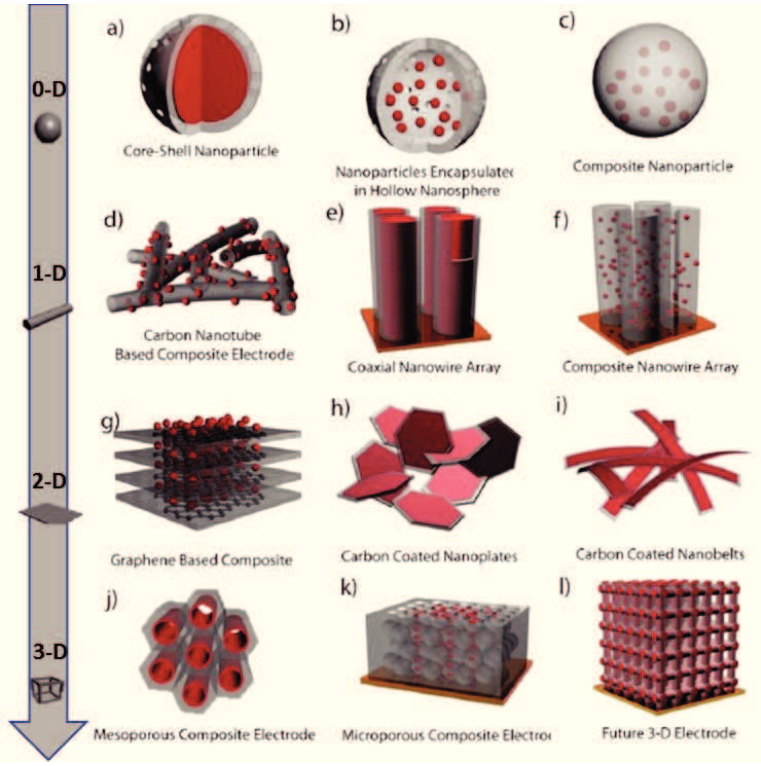

Figure 1. Different heterogeneous nanostructured materials based on structural complexity. Adapted from ref. 5

NMs have the structural features in between of those of atoms and the bulk materials. While most microstructured materials have similar properties to the corresponding bulk materials, the properties of materials with nanometer dimensions are significantly different from those of atoms and bulks materials. Specifically, two different reasons confer them these unique properties: *i)* a greater surface area-to-volume ratio than their bulk that leads to a higher chemical reactivity; *ii)* quantum effects leading to novel optical, electrical and magnetic behaviours.

2.1 Physico/chemical properties of nanomaterials at the biointerfaces

2.1.1 Size and shape properties

Nanometer-scaled dimensions influence drastically the interaction of an artificial material with biosystems and therefore its final fate for *in vivo* applications.[6,7] NPs can be synthesized into structures with a myriad of shapes and sizes, based on a variety of synthesis methods. The shape of NMs has a direct effect on how NPs function *in vivo*.[8] Also, researchers have shown that NPs with a hydrodynamic diameter smaller than 5.5 nm effectively clear the renal system, providing a unique opportunity for balancing efficacy with minimal toxicity.[9,10]

2.1.2 Electrical properties

Electrical properties of NPs encompass the properties of electrical conductivity in nanotubes and nanorods, carbon nanotubes, photoconductivity of nanorods, electrical conductivity of nanocomposites, including the appearance of new features in the electronic structure. The important point here is that, with decreasing diameter of the system, the number of electron wave modes contributing to the electrical conductivity is becoming increasingly smaller by well-defined quantized steps. The energy band structure and charge carrier density in the materials can be modified quite differently from their bulk and in turn will modify the electronic and optical properties of the materials.[11]

Bio-electronics faces challenges associated with the mismatch between the hard, planar surfaces of conventional electronics and the soft, 3-dimensional (3D) tissues of biological systems. For example, the brain-machine interface presents the most significant challenges, in that the brain is very soft (elastic modulus <500 Pa) unlike rigid conventional electronics (>100 GPa).[12] Another case is about graphene-based materials; superb electromechanical properties of graphene, where more than 20% of elastic deformation is achievable without perturbation of the electrical properties, have been recently explored as flexible electrode materials.[13,14] Practical applications, such as graphene-based transparent electrodes, [15] have been implemented,

demonstrating potential for flexible touch screens. Such unique electromechanical properties can be applied to biological systems, in particular the biointerfaces, where mechanical flexibility and electrical functions (*e.g.*, stimulation and detection) of graphene membrane can be fully utilized. Recently, an unconventional approach for the single-step synthesis of monolithically-integrated electronic devices based on graphene and graphite for all-carbon bio-electronics have demonstrated. These all-carbon structures were transferrable onto both rigid and flexible substrates. The integrated transistor arrays were used to demonstrate real-time, multiplexed chemical sensing, and furthermore, flexible and conformal interface for bio-electronic applications.[16]

2.1.3 Mechanical properties

The mechanical behaviour of materials at the nanoscale is often different from that at macroscopic scale. Indeed, the continuum mechanics applies when sizes are above the 10 nm range, whereas surface effects may control the deformation properties. For structures with micrometer sizes, the mechanical properties are controlled by the elastic strain energy. At the nanometer length scale, due to the increasing surface-to-volume ratio, surface effects become predominant and can significantly modify the macroscopic properties. For the smaller diameters, in the case of metallic nanowires and polymer nanotubes, the

measured elastic modulus significantly differs from that of the bulk materials. Calculation of an apparent elastic modulus taking into account the surface effect shows that the observed increase of the elastic modulus with decreasing diameter is essentially due to surface tension effects.[17] The typical observed trend is the decreasing values of the mechanical parameters with decreasing size of the nanostructure.

Carbon nanotube (CNT)-reinforced polymer composites have been extensively studied for their applications as biomedical materials but in the recent time the interest in graphene based materials is growing more and more.[18] The CNT-based scaffolds are mechanically strong and electro-active and are useful for stimulated/guided growth of cells. However, because of the metal catalyst used in the fabrication of CNT can be trapped inside carbon nanotubes, metal-free carbon nanotubes are only obtained after extensive and time-consuming purification processes. On the other hand, graphene platelets significantly out-performed carbon nanotubes as a reinforced additive. For instance, graphene sheets demonstrated ultra-strong and biocompatible properties, which are highly desirable for scaffolds in bone tissue engineering. Fan et al. measured the mechanical properties of graphene/chitosan composite films by the nanoindentation method and found that chitosan was significantly reinforced upon the addition of a small amount of graphene sheets.[19]

2.1.4 Optical properties

The optical properties need to be tuned in order to fit the narrow window in which light is able to penetrate tissue, for *in vivo* applications of NMs such as photothermal and photodynamic therapies. The main challenge for successful intravital imaging is achieving a better signal to noise ratio at greater depth. For the best performance both the excitation and emission maxima of the NM used should lie in the range of 650 to 900 nm, called the "near–infrared optical window", which is characterized by the lowest tissue absorbance.[20,21] Although this window often poses a problem for effective excitation of organic fluorophores, the use of NPs presents a versatile opportunity for exploiting this spectral regime.

In general, inorganic NPs with optical properties can be divided into two classes: semiconductor and metallic nanostructures. In both cases, the *physical confinement* of the material on the order of nanometers induces specific optical properties. For *semiconductor materials*, this "quantum effect" can be described by treating electronic excitation as a particle in a three-dimensional box. Thus, a physical change in NP characteristics directly changes its electronic structure, enabling highly selective rational designs. The resulting change in absorption also corresponds to a shift in its photoluminescence (PL), allowing for effective "tuning" for a desired application.[22] For *metallic nanostructures*, the strong absorption of light is due to

a quite different phenomenon known as the surface plasmon resonance (SPR). In metals, the conduction electrons at the surface of the NP collectively oscillate with a corresponding excitation of a resonant wavelength of light. This collective oscillation results in a strong absorption of typically 10^9 M^{-1} cm^{-1} OD for a 40 nm gold NP and ultrafast electronic relaxation.[23] As the shape of the metal is extended, the radiation needed to excite the SPR gradually shifts towards longer wavelengths. Also, with an increase in NP size, the amount of light scattering increases according to Mie theory,[24] and variations in shape (nanorods, nanocubes, nanocages, nanoplates, etc.) lead to unique scattering properties. The scattering is coupled to the unique SPR phenomenon of metallic nanostructures, resulting in a dramatic enhancement, which can be used for biomedical imaging applications.

2.1.5 Magnetic properties

Bulk gold and Pt are non-magnetic, but at the nanosize they are magnetic. This phenomenon opens the possibility to modify the physical properties of the NPs by capping them with appropriate molecules. Non-ferromagnetic bulk materials can exhibit a ferromagnetic-like behaviour when prepared in nanorange. For example, one can obtain magnetic NPs of Pd, Pt and the surprising case of Au (that is diamagnetic in bulk) from non-magnetic bulk materials. In the case of Pt and Pd, the

ferromagnetism arises from the structural changes associated with size effects. Au NPs become ferromagnetic when capped with appropriate molecules: the charge localized at the particle surface gives rise to ferromagnetic-like behaviour. Thus, the surface and the core of AuNPs of 2 nm in diameter show ferromagnetic and paramagnetic character, respectively.[25] The large spin-orbit coupling of noble metals can yield to a large anisotropy and therefore high ordering temperatures. More surprisingly, permanent magnetism was observed up to room temperature for thiol-capped Au nanoparticles. For nanoparticles with sizes below 2 nm the localized carriers were identified in the 5d band. On the other hand, for bulk Au an extremely low density of states and diamagnetic properties were determined, as is also the case for bare Au nanoparticles. This observation suggested that modification of the d band structure by chemical bonding could induce ferromagnetic like character in metallic clusters. [26]

Due to the possibility of converting the dissipated magnetic energy into thermal energy, the field of magnetic nanoparticles (MNPs) has been the subject of deep investigations in nanomedicine applications. MNP-based hyperthermia treatment has a number of advantages compared to conventional hyperthermia treatment. These are schematically summarised here: 1) MNPs uptake by the cancer cells increases the effectiveness of hyperthermia by delivering therapeutic heat

directly to them; 2) MNPs can be targeted through cancer-specific binding agents making the treatment much more selective and effective; 3) the frequencies of oscillating magnetic fields generally employed pass harmlessly through the body, generating heat only in tissues containing the MNPs; 4) MNPs can also effectively cross the blood-brain barrier (BBB) and hence be used for treating brain tumours; 5) effective and externally stimulated heating can be delivered at cellular levels through an alternating magnetic field (AMF); 6) stable colloidal nanoparticles obtained by using MNPs, can be administered through a number of drug delivery routes; 7) MNPs used for hyperthermia are only few tens of nanometres in size and therefore, allow for easy passage into several tumours whose pore sizes are in the range of hundreds of nanometres; 8) compared to macroscopic implants, the MNP-based heat generation is much more efficient and homogeneous; 9) the MNP-based hyperthermia treatment may induce antitumor immunity; 10) last, but most importantly, the MNP-based hyperthermia can also be exploited for controlled delivery of drugs. The first nano-construct of such a type was made by using a layer-by-layer self-assembly approach.[27]

2.2 Fabrication methods of nanomaterials

The preparation of nanoscale structures and devices can be accomplished through either "bottom-up" or "top-down" methods. The difference between these two approaches can be explained simply by using the example of powder production, where chemical synthesis represents the bottom-up approach while crushing and milling of chunks represents the equivalent top-down process. On examining these technologies more closely, the expression "top-down" means the starting from large pieces of material and producing the intended structure by lithographic techniques (*e.g.*, UV, electron or ion beam, scanning probe, optical near field), film deposition and growth, laser beam processing, and mechanical techniques (e.g., machining, grinding, and polishing). As long as the structures are within a range of sizes that are accessible by either mechanical tools or photolithographic processes, then top-down processes have an unmatched flexibility in their application.[28]

In the bottom-up approach, small building blocks (such as atoms or molecules) are assembled into larger structures to produce NPs, nanotubes, nanorods, thin films or layered structures; examples of this approach include chemical synthesis, laser-induced assembly (i.e., laser trapping), self-assembly, colloidal aggregation, and two-photon confocal processing.[29]

While bottom-up techniques can provide access to extremely fine features and state-of-the-art structures, the complexities

associated with these techniques still limit large-scale production. Ultimate physical limits may also be encountered, such as perturbations (e.g., molecular vibrations) that disrupt the smallest of nanoscopic structures. Many top-down techniques have been developed on the industrial scale, and optimization of this processes has produced well-defined structures on scales previously thought unreachable. However, these techniques have an inherent size limit that is larger than that of bottom-up techniques. Thus, to produce devices with extraordinarily fine detail on the molecular level, self-assembly and directed assembly approaches must become integrated into the industrial process.

2.3 Targeting strategies of nanoparticles.

Surface-functionalized NPs are able to specifically internalize within cancer cells. This strategy represents an elegant solution to the problem of non-specific biodistribution and poor bioavailability of conventional drugs. Indeed, most chemotherapeutic drugs target non-specifically within the body, which account for much of their toxicity and side effects.

Generally, solid tumours contain leaky blood vessels with cell junction gaps ranging from 100 nm to 780 nm, compared with pore diameters of up to 20 nm in normal capillaries.[30] This phenomenon is known as enhanced permeability and retention (EPR) effect and represents the passive targeting of NPs at the

tumour site.[31] However, the sizes of these endothelial fenestrations are known to vary with tumour type and microenvironment.

On the contrary, an active targeting can help the NPs to selectively recognize specific membrane receptors or antigens on target cells when conjugated with specific molecules. Such ligands can also facilitate the cell surface adsorption/internalization through specific interactions. Also, the type of targeting molecule used will largely determine the physicochemical properties of the NP-ligand conjugates in term of stability, biocompatibility and prolonged circulation time.[32]

Among many kinds of targeting molecules employed, the most used include proteins (mainly antibodies and their fragments), nucleic acids (aptamers) and other receptor ligands (proteins, peptides, small molecules, etc.) which is over-expressed in cancer cells.[33] For example, small peptide arginine-glycine-aspartic acid (RGD) can bind to cell adhesion integrin receptor $\alpha_v\beta_3$ that is abundant on the surface of endothelial cells and other various cancer cells, and thus can be used to specifically deliver NPs to tumour (Figure 2).[34]

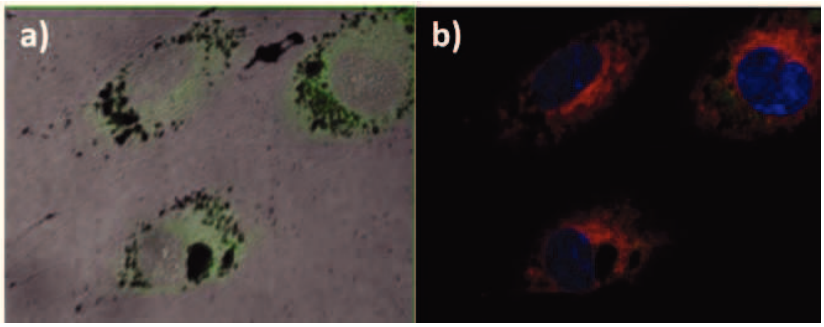

Figure 2. Confocal microscopy images of neuroblastoma cells after 2h of treatment with 3 nM AuNPs functionalized through cysteine bonds with a fluorescein-labelled RGD peptide (green). In the panel *a)*: the correspondent merge of the green fluorescence image and the optical bright field micrograph (AuNPs aggregates are visible as dark spots); *b)*: merged fluorescence micrographs of nuclei (blue), lysosomes (red) and AuNP-peptide (green). Adapted from ref. 35

Folate conjugation can significantly promote their targeted delivery of NPs into cancer cells that overexpress folate receptors.[36]

2.4 Biosystems of interest at the hybrid interface with NMs.

Different type of biosystems are involved in the interaction with the NMs.[37] Generally, it is possible to distinguish two different level of interactions:

- Cellular interactions. NMs affect cell machinery including cell surface molecules and intracellular organelles.[38]

- Biomolecules interactions. NMs interact with proteins in biological media,[39] modulate the biological activity of growth factors in competition with antibodies.[40]

The biological identity of a nanomaterial is a function of its synthetic identity (size, shape, and surface chemistry post-synthesis), the physiological environment, and the duration of exposure. Due to relatively large surface area compared to the size and positive/negative surface charge, nanoparticles without surface modification are an easy target of the proteins of the biological media. Various types of intermolecular forces occur between NMs and proteins: Van der Waals interactions, hydrogen bonds, electrostatic forces, hydrostatic interactions, π–π stacking interactions, and salt bridges.[41] These interactions initiate and reinforce the binding between nanoparticles and proteins.

The addition of ligands or receptors onto the surface of nanoparticles enhances target-specificity. In this contest, well-designed nanosystems modulate the biological response. Indeed, physicochemical characteristics of NMs can affect cellular uptake, biological distribution, penetration into biological barriers, and resultant therapeutic effects.[42,43]

In this context, in this thesis work several biosystems interacting with NMs have been investigated. Firstly, peptides that mimic specific biological activities as the receptors recognition (RGD-peptide), growth factors (VEGF) and neurotrophic factors

(NGF-BDNF). Secondly, a model protein that typically interact by hydrophobic forces (HSA) and a natural compound with antioxidative properties and low solubility in aqueous solution (curcumin). Thirdly, phospholipid unilamellar vesicles that mimic the cellular biomembranes for biosensors applications. The following subchapters describe the principal characteristics, and the possible main applications of these biosystems in hybrid assembly with NMs as therapeutics and sensors.

Tumour early diagnosis, therapy, and imaging are main goals of nanomedicine and theranostics. [44,45]

The progression of a normal somatic cell to the metastasis state involves many steps. [46] The typical cancer growth is characterized by a state of hypoxia when its dimension reaches approximately 2 mm^3. At this stage, the inner high interstitial pressure inhibits the diffusion of metabolites and nutrients necessary for its development. Therefore, the formation of new blood vessels from pre-existing vessels begin with the degradation of the endothelial cell basement membrane and extracellular matrix, a process regulated by the matrix metalloproteinases (MMPs). After this degradation, endothelial cells proliferate and migrate until they form unstable microvessels. Mesenchymal cells differentiate into pericytes, which allow the stability of new formatted vessels and the re-established of blood flow. [47] This phenomenon is named *angiogenesis*, which is considered a key process for the

development of tumor condition.[48] Normal angiogenesis is known as a vascular development for the essential process of foetal, wound healing, ovulation and growth. On contrary, tumor angiogenesis carries oxygen and nutrients to tumor cells for their survival and proliferation. During this stage, the tumor is in a "dormancy state", meaning the tumor mass expands slowly, resulting in an asymptomatic and non-metastatic state.[49] The develop of the tumor from a non-angiogenic to an angiogenic phenotype is called the "angiogenic switch",[50] which is characterized by signals such as metabolic stress (low pH, low oxygen pressure), mechanical stress, inflammatory response, and genetic mutations. These signals lead to increased expression of angiogenic proteins by tumor cells (such as VEGF), by stromal cells and a decreased expression of angiogenic inhibitors by tumor cells and stromal cells (such as thrombospondin-1), which directly governed the angiogenic switch. However, after the angiogenic switch the tumor mass expands rapidly.[51] Various classes of adhesion molecules are involved in tumor angiogenesis, such as the integrin,[52,53] cadherin, selectin, and immunoglobulin families.[54]

2.5 Pathways of NPs Cellular Internalization

When NPs are incubated with cells *in vitro*, the serum proteins (such as albumin, fibrinogen, globulins) supplemented to the culture medium interact with the NPs. Such a process results into

a non-specific adsorption of serum proteins on NPs, which mediates the cellular uptake *via* receptor-mediated endocytosis pathways.[55] The structure and composition of such protein adlayer, named "protein corona", depends on various parameters: *i)* the physicochemical properties of the nanomaterial (size, shape, composition, surface functional groups, and surface charges); *ii)* the nature of the physiological environment (blood, interstitial fluid, cell cytoplasm, etc.); *iii)* the exposure duration.

The adsorbed protein molecules can change their conformation due to interactions with the nanoparticle surface, which, in turn, may affect the overall bio-reactivity of the nanoparticle, *e.g.*, including the change in the hydrodynamic diameter of NPs conjugates (that could affect extravasation); the interaction of NPs with cells (uptake and intracellular trafficking mechanisms); inflammation; accumulation; degradation and clearance of the nanoparticles. Both phagocytic and non-phagocytic cell types can capture the sizeable NP-protein complexes.[56]

Cells have a maximum receptor density on the membrane: the unbound or available receptors determine whether and how much a molecule or structure enters a cell *via* this mechanism. Nanoparticle size and shape can mediate receptor-ligand binding constants, receptor recycling rates, and exocytosis. Ligand density, membrane adhesion areas, membrane stretching and

bending are all factors potentially involved in the size (and shape)-dependent uptake of NPs.

Generally, nanoparticles, in the size range from a few to several hundreds of nanometers, not able to cross the cell membrane by diffusion either can still internalized by cells through several parallel series of routes, termed endocytosis.[57] Endocytosis is involved in the cellular uptake of NPs for the majority of cases, particularly for AuNPs.

Finally, it is noteworthy that the pathway of cellular internalization strictly affects the cytotoxicity of metallic nanoparticles. In particular, AuNPs and AgNPs, forced through the cell membrane bypassing any forms of active mechanism such as endocytosis, showed a different distribution within the cytosol compared to NPs entering the cell by active endocytosis. Specifically, they did not accumulate in lysosomes, suggesting that intracellular accumulation of metallic nanoparticles into endolysosomal compartments is the leading cause of nanotoxicity.[58]

The most relevant properties of GFNs for their biological effects include surface area, layers number and lateral dimension. Small nanoparticles theoretically have a significant surface area exposed; monolayer graphene represents the optimum in which every atom is surrounded by medium on two sides. Obviously, the number of the layers in a GFNs is important because it determines specific surface area and bending stiffness. The

lower is the number of layers, the better is the adsorptive capacity for biological molecules. On the contrary, multilayer materials may act as rigid bodies during their cellular interactions.

Moreover, lateral dimension determines the maximum dimension of materials which is relevant for cell uptake, renal clearance and blood-brain barrier transport. Particularly, lateral dimensions should affect the type of receptors involved in the uptake and also the size of the endosome or lysosome into which the material must be packaged within the cell.[59] Mu et al.[60] demonstrated that the GO internalization was mediated by clathrin endocytosis for dimension layers of ≈ 500 nm, whereas larger GO layers (≈ 1μm) exhibited uptake by phagocytosis. Furthermore, the internalization process of GNFs can directly occur either the membrane damage or a potentially enhancement of cell growth and shielding effect with no cell damage.[61]

2.6 Nanotoxicity

When introduced within the body, nanoparticles are often perceived by the cells as adverse agents, inducing the cell generation of reactive oxygen species (ROS) and nitrogen oxygen species (NOS) under irradiation.[62] Generally, cells are able to buffer small and transient increases of these reactive species while an excessive increasing of them can lead the cells to various negative effects. The creation of an oxidative

environment drives cells to respond to the changes in order to avoid oxidative stress death, for example by the formation of autophagosomes.

The high surface area/volume ratio of nanoparticles, which is their peculiar feature, seems to be the first cause of toxicity. Both *in vivo* and *in vitro*, nanoparticles have a tendency to accumulate within various types of cells, producing vary degrees of bioaccumulation in such tissues as lymph nodes, spleen, bone marrow, liver, adrenals and kidneys.[63]

The NPs size plays an important role in avoiding immune activation and renal clearance, thus enhancing their circulating time and availability for effective therapy. NPs can stimulate and/or suppress the immune responses and that their compatibility with the immune system is largely determined by their surface chemistry.[64]

A third essential aspect to consider for toxicity is the nanoparticles surface functionalization with biomolecules, stabilizers, etc. The surface coating can contribute to unspecific adsorption or specific recognition by the immune system, thus generating toxicity effects.[64]

A general discussion on the toxicity of GFNs it is not possible, since it depends on several parameters: dimensions and concentration,[65] superficial coating,[155] type of cell target,[66] and so on.[67]

Oxidative stress is considered one of the main causes of the mechanisms involved in the toxic effects of carbon nanomaterials.[68] Also, due to its hydrophobic surface, graphene can significantly interact with cell membrane lipids, causing toxicity. Furthermore, cell membrane damage through physical interaction with graphene sheets possessing sharp edges is another possible mechanism of toxicity.[69] Pristine graphene seems to decrease cell adhesion, inducing cell apoptosis and increasing the accumulation of these nanomaterials into various cellular compartments. Moreover, biomolecular modification plays an important role because it might reduce the strong hydrophobic interaction of graphene or GO with cells and tissues.

In vivo studies indicated chronic toxicity associated with GO.[70] After intravenous injections, GO and functionalized GO seem to deposit in the lung occurring inflammation in dose-dependent manner,[71] in the RES such as the liver and spleen.[72]

3 Metal surfaces at the biointerface with neurotrophin peptides, vascular endothelial growth factor peptides, RGD peptides.

3.1 Silver and Gold Nanoparticles in theranostics

Therapeutic uses of silver and gold are known since ancient times.[73] Nowadays, these materials at the nanoscale dimensions demonstrate further therapeutic properties depending on several factors including their size, shape, particle concentration and their superficial charge. Silver nanoparticles (AgNPs) are known to have significant inhibitory effects against pathogens and are used as antimicrobial agents in different fields. Similarly, gold nanoparticles (AuNPs) are widely employed in the treatment of bacterial infections, rheumatoid arthritis, cancer.[74,75]

Gold and silver are known to bind strongly to soft bases like thiols and, moderately strongly, to amine functionalities.[76] Such affinities cause these NMs the selective binding to biomolecules (e.g., proteins, DNA, etc.).

With the rapid development of nanotechnology, the application of AuNPs and AgNPs have been further extended. In the last decades, AuNPs and AgNPs nanoparticles have obtained a lot of interest as smart devices in various fields ranging from chemical sensing[77] to catalysis[78] and optics.[79] These particles have also gained many applications in the specific biomedical field such

as for medical imaging,[80] nanocomposites[81] and drug delivery[82] (Figure 3).

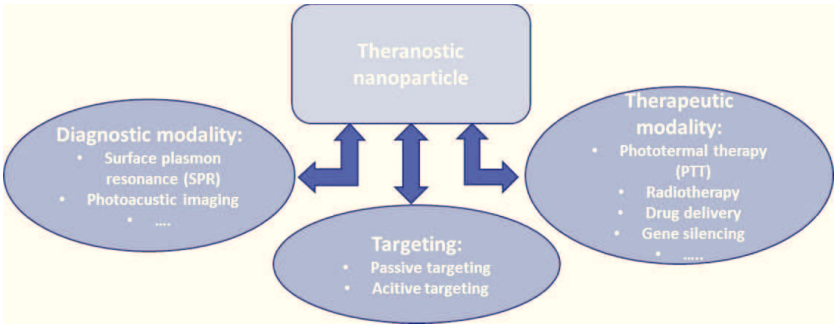

Figure 3. A schematic view of the multimodal working principle of a theranostic platform based on metal nanoparticle. Adapted from ref. 35

Although numerous studies collected in various recent reviews,[83,35] the application of these nanoparticles in theranostic fields suffer of many opened questions, e.g., the nanomaterials interaction with cells at the molecular level; their biodistribution and pharmacokinetics; their actual therapeutic efficacy; the mechanism of detoxification/clearance and the potentially nanoparticle toxicity. AuNPs and AgNPs are considered emerging theranostic agents for in vitro but also in vivo applications.

The versatility in the metal surface functionalization for immobilizing various drugs and targeting agents make AuNPs and AgNPs innovative therapeutic nanoplatforms for drug delivery[84] and gene silence[85], reinforcing their well-known intrinsic biological properties.

Hyperthermia and photothermal therapies can be considered potential therapeutic applications of NPs. In nanoparticle-mediated hyperthermia for cancer, NPs heat up cancerous cells beyond their temperature tolerance limits, which are lower than normal healthy tissue due to their poor blood supply, killing them selectively.[86] Photothermal therapy (PTT) exploits the hyperthermia phenomenon. In fact, when NPs are excited with a precisely laser energy tuned to the specific surface plasmon resonance (SPR) of the metal nanoparticle, surface electrons become excited and resonate vigorously. When these electrons return to the ground state, they emit energy in the form of heat and the surrounding temperature is raised.[87] This photothermal reaction can be applied to kill cells within tumours, specifically in places that are difficult to reach surgically or require a palliative procedure.

Also, the plasmonic properties of silver and gold nanoparticles as well as their extremely high extinction coefficients make them a novel class of materials for biological sensing and colorimetric sensors.[88]

The colorimetric approach is based on the shift of the optical absorbance of nanoparticles in dispersion upon their aggregation. For example, AgNPs change colour from yellow to red and AuNPs from red to blue.[89] It has been demonstrated as a very simple method for the use of metal nanoparticles as sensors

highly selective towards sulphur-containing compounds such as cysteine.[90]

Furthermore, gold and silver nanoparticles are considered smart sensors exploiting localized surface plasmon resonance (LSPR) frequency shift, due to the interaction between nanoparticle and target molecule.[91]

In the electromagnetic mechanism, the surface plasmon excitation enhance the local electric fields in the surroundings of the metal nanoparticle, leading to more intense electronic transitions in molecules located near the nanoparticle and enhanced Raman scattering. This phenomenon is called Surface Enhanced Raman Spectroscopy (SERS) effect. In the chemical mechanism, the charge transfer interaction between electronic states of the molecule and the metal nanoparticle surface changes the polarizability of the molecule, which results in increased Raman signals. This effect is exploited to well design sensors. The most active metal in SERS is silver (with enhancement factors as high as 10^{14}-10^{15}), followed by gold and copper, enabling detection limits as low as a single molecule.[92]

Finally, metal nanoparticles are known to interact with nearby fluorophores affecting their emission intensity. When this interaction results in a fluorescence enhancement, the effect is known as Metal Enhanced Fluorescence (MEF). [93] This enhanced sensitivity has been recently applied to detect the binding of different drugs to human cytochrome P450.[94]

3.2 Synthetic strategies of Gold and Silver Nanoparticles.

Metal NPs can be synthesized by different approaches classified in three wide classes: chemical, physical and biological.

For many years, wet chemical methods have been the most employed strategy for the synthesis of metal nanoparticles, based on a "bottom up" principle process. In 1857, Michael Faraday synthesized for the first time "fine gold particles".[95] From then on, many alternative methods were discovered. The most popular was invented by Turkevich *et al.* in 1951.[96] The preparation regarded water dispersed AuNPs of 20 nm in diameter after the reduction of $AuCl_4^-$ in a boiling sodium citrate solution. Since then, the Turkevich's method has been improved and extended to other metals, including silver.[97,98] Generally, metal salts are reduced to give zerovalent metal atoms in the embryonic stage of nucleation. These can collide in solution with further metal ions, atoms, or clusters to form an irreversible "seed" of stable metal nuclei. These clusters eventually lead to formation of metallic colloidal particles. Furthermore, different mechanisms of growth particles have been proposed depending on the reduction method, e.g., La Mer' growth;[99] Ostwald ripening;[100] Polte's model;[101] Pong's model.[102]

The reducing agents can act both to reduce the metal cations and as capping agent, preventing aggregation of the particles and

stabilizing the resulting nanoparticles by electrostatic and/or physical repulsion.

Using different reducing agents and stabilizers is possible to tune the particle sizes and morphologies of metal nanoparticles; also, small changes in synthetic factors lead to dramatic modifications in nanoparticle stability, self-assembly patterns, average size and size distribution width.[103] It was showed that strong reductants such as borohydride result in small monodisperse particles, but also in the generation, difficult to control, of larger particles; instead, weaker reductants, such as citrate, result in a slower reduction rate, but a wide size distribution. Also, a two-step reduction process has been developed for the controlled synthesis of metal nanoparticles.[104]

In order to stabilize and to prevent unwanted agglomeration of the colloids during the synthesis, nanostructured colloidal metals require protective agents. A large variety of stabilizers are used to control the growth of the primarily formed nanoclusters and to prevent them from agglomerating. The main classes of protective groups are: polymers and block copolymers such as poly(vinyl alcohol) (PVA), poly(vinylpyrrolidone) (PVP), poly(ethylene glycol) (PEG), poly(methacrylic acid) (PMAA) and polymethylmethacrylate (PMMA);[105] P, N, S donors (*e.g.,* phosphines, amines, thioethers); [106] surfactants [107] and organometallics.[108] In general, lipophilic protective agents give metal colloids that are soluble in organic media ("organosols")

while hydrophilic agents yield water-soluble colloids ("hydrosols"). Several other methods based on wet chemistry have developed to make stabilized nanoparticles of different sizes and shapes. Among them, it is important to mention electrochemical and sonoelectrochemical methods;[109] polyol methods[110] and microemulsion techniques,[111] and so on.

A wide variety of physical method synthesis of metal nanoparticles have been also studied, including: thermal reduction and photochemical reduction,[112] radiolysis[113] and laser ablation.[114]

Biological methods are green approaches where nanoparticles are synthesized by utilizing extracts from bio-organisms as reductant, capping agents or both. Such extracts can include microorganisms, proteins, amino acids, polysaccharides, and vitamins.[115] These approaches have been suggested as possible ecofriendly alternatives to chemical and physical methods, to synthesize gold and silver nanoparticles without using any harsh, toxic and expensive chemical substances.

3.3 Surface functionalization of metal nanoparticles.

The surface functionalization of AuNPs and AgNPs enables to change their surface structures, morphologies and charges. All these properties will affect the response of the NMs at the hybrid biointerface with the biological environment.[116] *In general, the strategies for nanoparticle functionalization with biomolecules follow two main approaches: physical adsorption and chemisorption (Figure 4).*

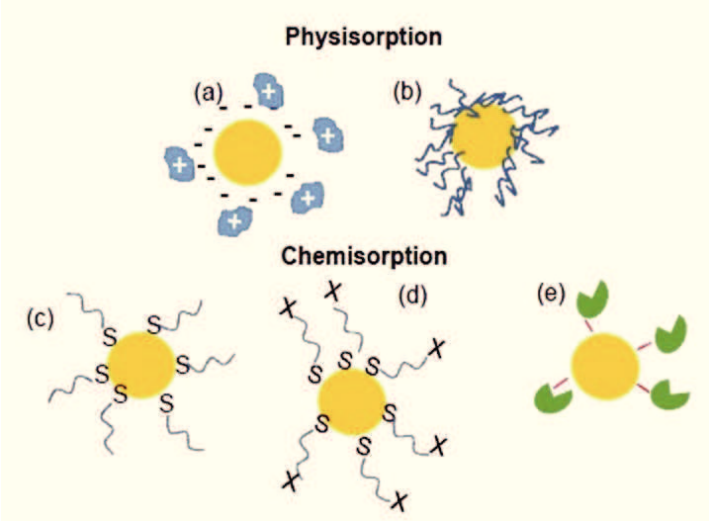

Figure 4. A schematic representation of different approaches for the metal nanoparticle surface functionalization by physical adsorption (a: driven by electrostatics; b) macromolecule adsorption) or by chemical adsorption (c: direct chemisorption of thiol derivatives; d: covalent binding through bifunctional linkers; e: binding by specific affinity interactions). Adapted from ref. 35

The physisorption method includes all forms of functionalization that does not involve a direct chemical bond between the biomolecule and the surface of the nanoparticles: including hydrogen bonding, electrostatic and hydrophobic interactions. Among all ligands, proteins and antibodies have been used to functionalize nanoparticles. For example, gold and silver nanoparticles produced by chemical, reduction have been functionalized with IgG molecules exploiting the binding capability of the positively charged amino acid side chains of the protein to the negatively charged citrate groups on the colloids.[117]

The surface functionalization by chemisorption approach is based on the formation of actual covalent bonds to graft ligands to the nanoparticles. Some functional groups, such as cyano (-CN), mercapto (-SH), and amino ($-NH_2$) are known to have high affinity for gold[118] and silver[119] nanoparticles.

The non-covalent approach of surface functionalization has several advantages with respect to the covalent grafting. Firstly, the biomolecules to be physisorbed do not need derivatization and therefore modification or alteration of their macromolecular structure to proceed with the conjugation to the nanoparticles.[120] Secondly, simple electrostatics and/or hydrophobic mechanism can be used to trigger the adsorption/release of the biomolecules on the material surface.[121] Thirdly, the material surface can be tailored to finely tune the interactions with the biomolecule.[122]

Eventually, in the perspective of the controlled release of the biomolecule used to functionalize the nanoparticles, strong chemical stimuli (such as enzymes) are not necessary to break the bonds, but typically mild conditions are sufficient, *e.g.,* local environmental changes of pH, temperature, ionic strength and so on.[123]

3.4 Neurotrophin-mimicking peptides at the biointerface with gold respond to copper ions stimuli

The study of assembled hybrid nano-biointerfaces as metal surfaces offers several advantages in the initial phases of design and surface engineering for potential applications in theranostic field. For these reasons, in this work we investigated the interactions of the peptide fragments NGF_{1-14} and $BDNF_{1-12}$, encompassing the N-terminal domains respectively of the proteins nerve growth factor (NGF) and brain-derived neurotrophic factor (BDNF), for the fabrication of a hybrid gold/peptide biointerface. The results of this work were published and here named PAPER I.

A brief description of the biological importance of neurotrophic factors was given in the following section.

3.4.1 Nerve Growth Factor (NGF) and Brain Derived Neurotrophic Factor (BDNF)

Brain Derived Neurotrophic Factor (BDNF) and Nerve Growth Factor (NGF) are recognised as important neurotrophic trophic factors in adulthood as well as development, and each is required by certain subsets of neurones for optimum function. [124]

NGF is a secreted growth factor, important in survival, growth and maintenance of specific types of neurons in the central and

peripheral nervous system. It was first investigated in a series of experiments, begun over sixty years ago, when a soluble growth factor, released from sarcoma tissue, was found to be able to cause outgrowth of fibres from sensory or sympathetic nerve cells placed nearby.[125,126]

BDNF supports the survival and maintenance of sensory neurons, retinal ganglia, certain cholinergic neurons, spinal motor neurons and some dopaminergic neurons.[127]

The mature neurotrophins NGF and BDNF each bind with picomolar affinity to their specific tyrosine kinase receptor TrkA and TrkB, respectively. For each Trk receptor, only the domain closest to the membrane (called d5 or Ig2) is required to bind to its neurotrophin ligand (Figure 5).[128,129] The binding to these receptors initiates dimerization of two receptors and trans-phosphorylation of certain tyrosine residues within the intracellular domains. Adapter proteins which have phosphotyrosine-binding motifs are then recruited to these sites of phosphorylation. These initiate intracellular signalling cascades which may lead to neuronal differentiation and/or survival and gene expression.

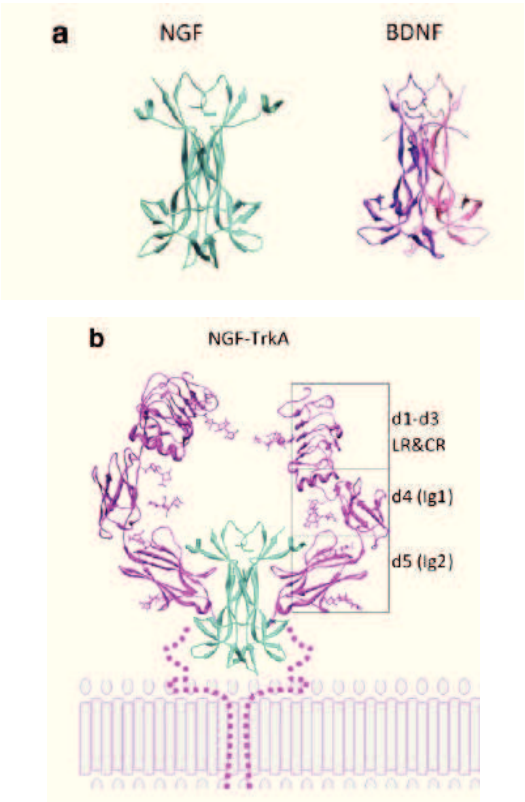

Figure 5. X-ray crystal structures of the neurotrophins and their receptors. (a) The X-ray crystal structures of the neurotrophins. (a) NGF (cyan, on the left side) and the BDNF (pink, on the right side). (b) Structures of receptors: TrkA (pink)–NGF (cyan). Apart from TrkA, only the d5 (Ig2) domain of each of the Trk receptors has been solved. However, it is assumed that the full 3D structure of the other Trk extracellular domains will be similar to TrkA. The extracellular region of the Trk receptors can be sub-divided (by amino acid sequence) into different domains (d1−d3 is a leucine-rich, cysteine-rich (LR&CR) region). Domains 4 and 5 are immunoglobulin-like domains. d5, the domain closest to the membrane, binds the mature neurotrophin directly. Dotted lines represent unknown protein conformation between the crystal structure and the plasma membrane (~40 residues for TrkA).Adapted from ref. 128,129

A reduction in level of one or more of these proteins may be responsible for at least some of the symptoms of neurological diseases such as AD (Alzheimer's Disease), PD (Parkinson's Disease), ALS (Amyotrophic lateral sclerosis), HD (Huntington's disease) and Rett syndrome.[124]

Recently, the N-terminal domains of NGF and BDNF have discovered to play a crucial role in the selective binding and the activation of TrkA and TrkB, involved in triggering pro-survival signals, respectively.[130] Accordingly, NGF_{1-14} and $BDNF_{1-12}$ peptides, encompassing the N-terminal sequences, respectively, of NGF and BDNF, designed and synthesized according to a peptide-mimetic strategy for the NGF and BDNF, have been reported to induce a cellular proliferation comparable to that found by using the respective whole proteins.[131,132]

Forte et al.[133] addressed the immobilization of NGF_{1-14} and $BDNF_{1-12}$ peptides on gold surfaces by a simple approach of spontaneous irreversible physical adsorption. Experimental findings highlight the different interactions between each peptide and the gold surface, which affect, in turn, hydrodynamic thickness and related viscoelastic properties of the adlayer. Moreover, the differences found under the two different pH conditions (7.4 and 5.5) investigated, suggest the possibility of fine tuning and triggering of the viscoelastic properties of the peptide adlayers, including shear modulus, viscosity, effective thickness and water content. In particular, a

synergic play of the two peptides in the adsorption on the gold is found at physiological pH, mostly related to the strong interaction between NGF_{1-14} and $BDNF_{1-12}$ molecules in the bulk solution, whereas a predominance of $BDNF_{1-12}$ in the adlayer is highlighted at the acid pH of 5.5, thus indicating a competitive peptide adsorption process under these conditions.

3.4.2 Copper role in the neurotrophin bioavailability

Copper is an essential metal in living organisms and its dynamic homeostasis, [134] i.e., the complex interplay of intra- and extracellular metal distribution and trafficking processes, can be a marker as well as a key regulator in different diseases such as cancer and neurodegeneration.[135]

Both NGF_{1-14} and $BDNF_{1-12}$ exhibit the capability of response to the stimulus induced by copper addition. Noteworthy, a strong decrease of the proliferative activity of both $BDNF_{1-12}$ and the whole protein on a SY-SH5H neuroblastoma cell line was found after treatment in the presence of Cu^{2+}.[136] The effect of metal addition is opposite to that observed for the analogous fragment of NGF protein, highlighting the role of specific domains, and suggesting that Cu^{2+} may drive different pathways for the BDNF and NGF in physiological as well as pathological conditions.

Accordingly, the combined action of copper and neurotrophin-like peptides, not only might result either in physiological or

pathological outcomes[137] but its understanding and modulation can have a high potential in therapeutics.

In order to develop nanobiointerfaces using gold and NGF, BDNF (or related peptides), we demonstrated the maintenance of peptide-specific responses on different pH values as well as in the copper binding also for the adlayers formed upon physisorption at the gold surface. The results obtained for the adsorption at the physiological pH (7.4) were compared with those obtained at acid pH (5.5), the latter taken as model microenvironment for pathological conditions, including hypoxia, ischemia and cancer. [138]

3.4.3 Results and Discussion

In the first part of the study, we focused on the response in solution towards copper ions of NGF_{1-14} and $BDNF_{1-12}$ in the pH range of 3-8, to be compared with response of the hybrid solid-liquid interface of peptide adlayer exposed to copper solution. The distribution diagram in Figure 6 displays the competitive binding to copper by the two peptides. In fact, at acid pH, $BDNF_{1-12}$ binds a single copper ion more tightly than NGF_{1-14}. Increasing the pH, there is an inversion trend, and the metal binds prevalently to NGF_{1-14}. Therefore, the relative weight of

the formed complex species, for both NGF_{1-14} and $BDNF_{1-12}$, depends on the pH range.

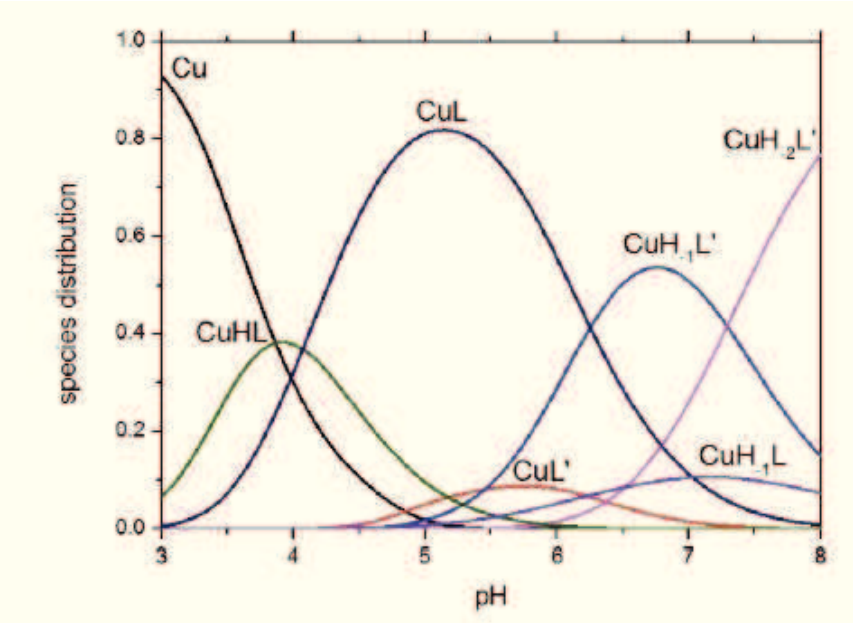

Figure 6. Distribution diagrams for Cu^{2+} complexes with NGF1-14 (=L') and BDNF1-12 (=L) peptides in aqueous solution at 1:1:1 molar ratio ($1x10^{-3}$ M). Reproduced from Ref. 138 with permission from the PCCP Owner Societies.

These finding were also confirmed by far-UV CD spectra reported in Figure 2 (PAPER I).

In order to study both the viscoelastic behaviour of the adlayer and competitive *vs.* synergic interactions in sequential adsorption processes, quartz crystal microbalance with dissipation monitoring (QCM-D) were addressed.

3.4.3.1 QCM-D analysis

QCM-D technique allows for in-situ monitoring of the adsorption kinetics of biomolecules at a solid surface. The principle of analysis of QCM is based on the resonance frequency of a quartz crystal induced by applying an alternating electric field across the crystal. Deposition of mass on the quartz surface decreases the crystal's oscillation frequency (negative frequency shift). For thin, rigid, and uniformly distributed layers, frequency shift is proportional to the mass change and can be calculated using the Sauerbrey equation.[139] However, when a soft or thick layer is bound to the crystal, there is also a change of dissipation and when this dissipation is large enough the mass can be underestimated by using only frequency and the Sauerbrey relation. In fact, the combined information from changes in frequency and dissipation is superior to frequency measurements alone.[140] Therefore, in all the other cases, which are the most common in soft-wet biointerfaces, for a correct determination of mass uptake, viscoelastic models (e.g., Voigt) are used to take into account both viscous and elastic contributions.[141]

In this study, the hybrid biointerface of Au/peptide/metal was tracked through experiments of peptide physisorption at the gold surface followed by the exposure of the peptides adlayer to copper ions solutions at pH=7.4 and pH 5.5. A simplified

scheme of various scenario which figured out from the QCM-D experiments is given in the Scheme 1 (Scheme1 in the paper I).

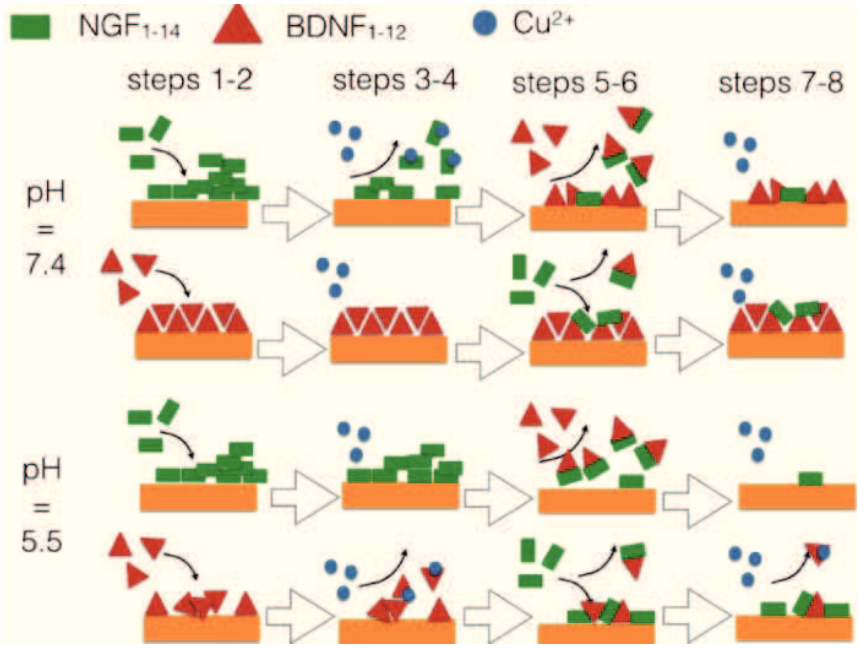

Scheme 1. Graphical picture of the processes deduced from QCM-D study of the sequential adsorption processes at the pH values of 7.4 and 5.5: Au-> NGF_{1-14}->Cu^{2+}-> $BDNF_{1-12}$-> Cu^{2+} and Au-> $BDNF_{1-12}$->Cu^{2+}-> NGF_{1-14}-> Cu^{2+}. Reproduced from Ref.138 with permission from the PCCP Owner Societies.

Accordingly, each QCM-D run consisted of the following the four-macro steps at the two-different pH: *i)* single peptide adsorption NGF_{1-14} (or $BDNF_{1-12}$) on Au surface (Step 1-2); *ii)* addition of copper ions to the peptide adlayer (Step 3-4); *iii)* addition of $BDNF_{1-12}$ (or NGF_{1-14}) (Step 5-6); *iv)* addition of copper ions to the double peptide adlayer (Step 7-8).

The response of Au/peptide systems to the addition of copper ions for pH=7.4 and pH= 5.5 was respectively shown in Figure 7. (Figure 3 and 4 in the PAPER I)

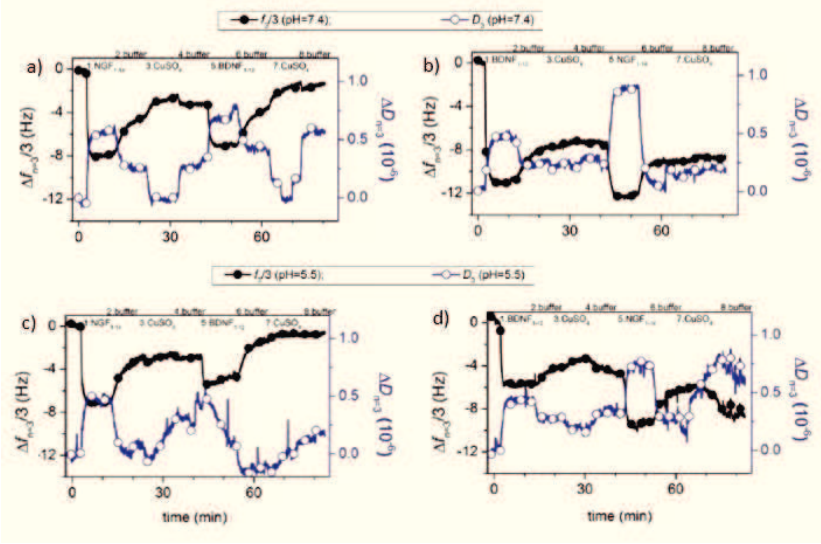

Figure 7. QCM-D curves recorded at the third overtone (n=3) of normalized frequency (Δf) and dissipation (ΔD) for experiments performed at pH 7.4 (at the top) and at pH 5.5 (at the bottom) of sequential peptide additions (a, c: first NGF1-14 and then BDNF1-12; b, d: first BDNF1-12 and then NGF1-14). In between the two sequential peptide additions there are steps of buffer rinsing and exposure to copper ions, respectively. Reproduced from Ref.138 with permission from the PCCP Owner Societies.

The figure above displays that the two peptides exhibited significant differences in Δf and ΔD, notwithstanding the similarities in isoelectric points and molecular weights, as well as the analogies in the C-terminus of the primary sequence (scheme 2). In fact, at physiological pH, the adsorption of NGF_{1-}

$_{14}$ on gold resulted in a relatively viscoelastic adlayer, whereas $BDNF_{1-12}$ formed a rigid adlayer.

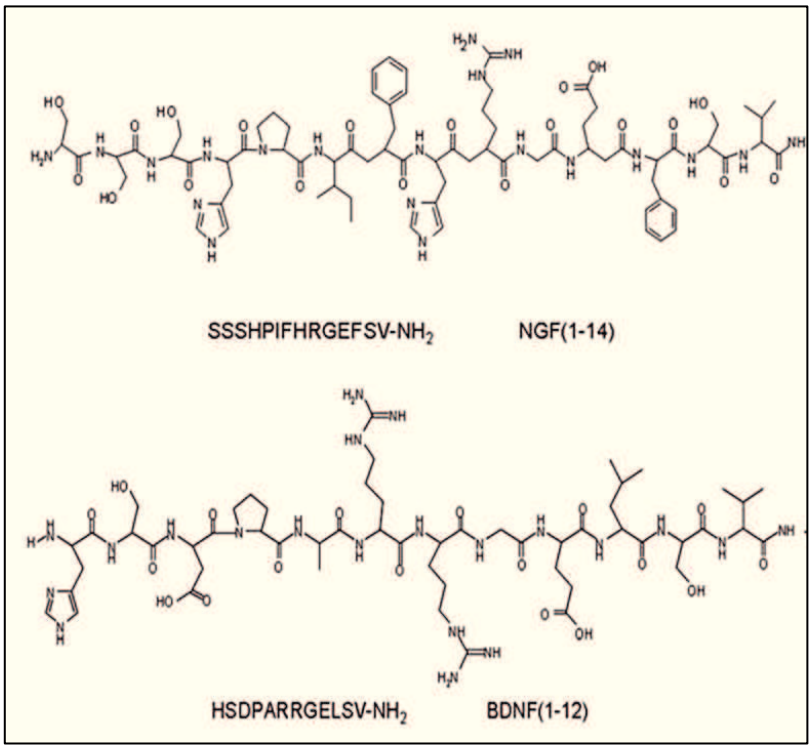

Scheme 2. Primary sequence of NGF (1-14) and BDNF (1-12).

Interestingly, the trend of copper binding affinity for the two peptides in solution discussed in Figure 7 was observed also at the solid-liquid interface, after the exposure to copper ions of the peptide molecules immobilized at the gold surface. Indeed, at pH=7.4, a strong interaction of Au/NGF_{1-14} with Cu^{2+} ions was evidenced by visible changes in both dissipation and frequency curves, while no significant shifts were observed for $Au/BDNF_{1-12}$. Such a finding can be related to the high tendency of NGF_{1-}

$_{14}$, at pH 7.4, to complex Cu^{2+} ions, favoured by a certain mobility of the NGF_{1-14} molecules within the viscoelastic adlayer. The curve trend is therefore interpreted as copper-induced desorption of the NGF_{1-14} from the gold surface. At the acid pH 5.5, the adsorption of NGF_{1-14} was similar in frequency and dissipation curves to what found at physiological pH (Step 3-4, Scheme 1).

On the other hand, the $BDNF_{1-12}$ adsorption exhibited a significant reduction both in the adsorbed mass and in the rigidity of the adlayer, as deduced from the frequency and dissipation shift values. As to the copper addition, shifts of both frequency and dissipation curves were obtained for Au/$BDNF_{1-12}$ but not for Au/NGF_{1-14}. This result is the opposite of what observed at pH 7.4.

The addition of the second peptide (step 5-6, Scheme 1) to the first adlayer (i.e., $BDNF_{1-12}$ to Au/NGF_{1-14} and vice versa) showed other interesting findings. For both the peptides and the pH values scrutinised, although more than a monolayer coverage is formed for the single peptide adlayer,[133] the addition of the second peptide still induced a significant mass uptake. This finding can be interpreted as the result of two opposite contributions. On the one side, the strong binding of $BDNF_{1-12}$ to the NGF_{1-14}, resulting in the formation of a heterodimer NGF_{1-14}-$BDNF_{1-12}$, as previously demonstrated,[133] which induces the adsorbed NGF_{1-14} to detach from the gold surface. On the other

side, the high affinity of $BDNF_{1-12}$ to adsorb onto gold at pH 7.4[133] would likely result in the replacement of the formerly adsorbed NGF_{1-14} peptide.

At pH = 5.5, the lower tendency of $BDNF_{1-12}$ to adsorb at the gold surface[133] compared to pH 7.4 prompts, upon its addition to Au/NGF_{1-14}, the almost complete detachment of NGF_{1-14} previously adsorbed, without any significant competitive/replacement effect towards the gold substrate.

For both pHs of 7.4 and 5.5, the final addition of Cu^{2+} ions (steps 7-8) did not produce any significant curve shift. This finding points to a minimal perturbation of the resulting Au/NGF_{1-14}->$BDNF_{1-12}$ adlayer to the copper stimulus.

The experiment of opposite sequential peptide adsorption, i.e., when NGF_{1-14} was added to $Au/BDNF_{1-12}$, showed a final extra mass uptake for both pH 7.4 and 5.5. Moreover, the following copper addition induced noticeable shifts only in dissipation at pH=7.4, and in both frequency and dissipation at pH=5.5. These findings can be interpreted as due to either molecule rearrangement within the adlayer[142] and their partial desorption from the surface (most likely NGF_{1-14} peptide). Therefore, the resulting $Au/BDNF_{1-12}$->NGF_{1-14} adlayer was responsive to the stimulus induced by copper ions addition much more than the Au/NGF_{1-14}->$BDNF_{1-12}$ case.

The QCM-D experiments of simultaneous peptides adsorption from the binary solution of NGF_{1-14} and $BDNF_{1-12}$ at both pH

values (see Figure 5 in the PAPER I) showed the Au/peptide interface exhibited a viscoelastic response. However, results at acid pH differ from physiological pH, where a synergic behaviour from both peptides contribute to the final properties of the Au/NGF_{1-14}-$BDNF_{1-12}$ adlayer. Indeed, at physiological pH, the Voigt modelling of QCM-D curves resulted in a viscoelastic mass; on the other hand, at acid pH, the similarity of QCM-D curves with those of $BDNF_{1-12}$ at the same pH suggests a predominant role played by this peptide in the mixed Au/NGF_{1-14}-$BDNF_{1-12}$ adlayer. According to these findings, the second part of the experiment, i.e. the addition of Cu^{2+} ions to the Au/peptides adlayer suggested, at pH 7.4, a peptide desorption and a lack of any apparent response at pH=5.

The binding stability between the adsorbed peptide molecules and the gold substrate were scrutinized also by molecular dynamics calculations. In agreement with the QCM-D data, a strong perturbative effect induced by addition of the copper ions to the peptide adlayers for NGF_{1-14} at physiological pH and $BDNF_{1-12}$ at acid pH was found, respectively. Moreover, strong similarities were found for the configurations Au/NGF_{1-14}/copper in the interaction, at the two-different pH, with free $BDNF_{1-12}$. Specifically, the metal was always released from the complex with the physisorbed peptide, owing to the NGF_{1-14}-$BDNF_{1-12}$ heterodimer entanglement. The only slight difference

with respect to Au/$BDNF_{1-12}$/copper, was a weaker release of the copper calculated at physiological pH.

3.4.3.2 Cellular response to the Au/peptide /copper systems.

The hybrid Au/peptide(s) systems assembled in the different combinations of peptide, pH of the solution during the peptide adsorption and sequence of peptide addition (for the sequential adsorption), were investigated at the biointerface with neuroblastoma cells. In this experiment the viability assay was used as indirect parameter to assess the biological response to the different hybrid biointerfaces for the various Au/peptide substrates well characterised by QCM-D and MD studies. Moreover, the cellular response to the various peptide adlayers in the presence of copper ions was investigated by supplementing the cell culture medium with a metal salt.

The results (in Figure 8 – PAPER I) pointed to significant substrate-dependent features. For samples prepared at pH=7.4, slight changes pointed to: *(i)* a general increase of viability response by Au/NGF_{1-14}+$BDNF_{1-12}$ in comparison to the single peptide adlayers (Au/NGF_{1-14} and Au/ $BDNF_{1-12}$) and the binary peptide adlayers prepared by sequential adsorption (Au/NGF_{1-14}->$BDNF_{1-12}$ and Au/$BDNF_{1-12}$->NGF_{1-14}); *(ii)* in the presence of copper, an increase of cells viability on single peptide, while a decrease on the binary peptide adlayers.

For Au/peptide samples prepared at pH=5.5 a significant difference was observed in the cases of Au/NGF_{1-14}, Au/NGF_{1-14}/Cu and Au/$BDNF_{1-12}$/Cu samples, which showed a visible decrease of cell viability in comparison with the control.

These findings could be related with the different scenarios of the hybrid Au/peptide/copper interface figured out by QCM-D and MD results, also if a direct correlation is not obvious.

In particular, the demonstrated maintenance, at pH=5.5, of peptide copper binding affinity for Au/$BDNF_{1-12}$ might explain a resultant copper-induced release of $BDNF_{1-12}$ from the adlayer, which was expected to decrease cell proliferation and then viability, according to previous results in solution.[17]

The present preliminary cellular results were, however, very interesting on the way of a general modulation of the cellular viability by an inorganic substrate.[143] In fact, a viability increase was observed at physiological pH, in the case of Au/peptides and Au/peptide/copper, while a viability decrease was found at pH 7.4 for Au/peptides/copper and, at pH 5.5, for Au/peptide/copper systems.

3.4.4 Conclusions.

Establishing the role of copper on the stability of these hybrid material, as well as the effect of copper on the biological property of the adsorbed biomolecule it was considered very important. In fact, it is known that copper is very abundant in the

extracellular space, and it is also released following activity dependent biological process, such as neurotransmission and neurorepair.[144]

In this study, we addressed the immobilization on gold surfaces by physisorption of NGF_{1-14} and $BDNF_{1-12}$ peptides, to investigate their responsiveness to pH and Cu^{2+} ions exposure. Experimental findings by QCM-D and CD analyses, as well as theoretical MD calculations, emphasised the different interaction between each peptide and the gold surface. The peptide-specific sensitivity during the adsorption process to two different pH conditions (physiologic and slightly acid) as well as to the exposure to copper ions, allowed for the tuning of viscoelastic properties, including shear modulus, viscosity, hydrodynamic thickness and water content. Preliminary cellular assays demonstrated a certain maintenance of relevant physicochemical and biological properties of the peptides adsorbed on gold with respect to their behaviour in bulk solution.

3.4.5 Future perspectives

Further cellular experiments are necessary to fully elucidate on the observed findings. For example, different peptide orientations/conformations in the various Au/peptide interfaces could be investigated by the use of receptor recognition assays,[145] thus allowing for a fine correlation between the cellular response and the physicochemical properties of the

neurotrophin-mimicking peptide adlayers at the gold surfaces, including viscoelastic properties and pH-tuned copper binding affinities.

Furthermore, the choice of the gold surface as substrate for the peptide immobilisation offers many advantages in the perspective of the drug delivery application, and, due to the plasmonic properties of gold, is a promising platform to implement, e.g., at the nanomaterial scale, for theranostic application.[35]

Results were very promising for the implementation of the proposed approach and systems to nanoparticles loaded with such neurotrophin-mimicking peptides, able to maintain biological properties and metal ion binding capability

3.5 Lipid bilayer-mediated immobilisation of neurotrophin peptides on gold nanoparticles: a new multipotential therapeutic nanoplatform for CNS disorders.

3.5.1 The peptide-mimetic approach and the nanoparticle-driven crossing of the blood brain barrier (BBB)

Neurodegenerative diseases represent a major socioeconomic burden and unimaginable misery for millions of sufferers and their families around the world. With an ageing population, the number affected is set to rise even further, creating an urgent need for therapeutic strategies which can reverse or halt the degenerative process.

The neutrophic factors as NGF and BDNF have been used as a neuro-restorative therapy in some form or other in clinical trials. For examples intrathecally in ALS (Amytrophic lateral sclerosis), NGF given in AD as an infused protein, and implanted cells secreting NGF, or by AAV delivery (Adeno-associated viral vector). [124] As this regard, the delivery of proteins into the human brain has inherent difficulties, and it is likely that the low success rate has been largely due to the protein not reaching the target at a sufficient concentration.

In fact, the blood brain barrier (BBB) is the essential interface between the central nervous system and the periphery. In the normal brain (as displayed in the figure 8), microvascular anatomy results from the interactions of endothelial cells (EC) with the basement membrane and neighboring cells,[146] such as

pericytes (PC), astrocytes, neurons and microglia (neurovascular unit).[147] All together, these cells contribute to create a selective permeability for the entry of molecules between the systemic circulation and nervous tissue, maintaining the homeostasis of the CNS. Particularly, EC are connected by highly structured tight junctions (TJs) and adherent junctions (Ajs),[148] which are constituted by cytoplasmic and trans-membrane proteins conferring either a very high trans-endothelial electrical resistance (TEER) compared to peripheral capillaries and rigorously narrow the passage of substances into the CNS.

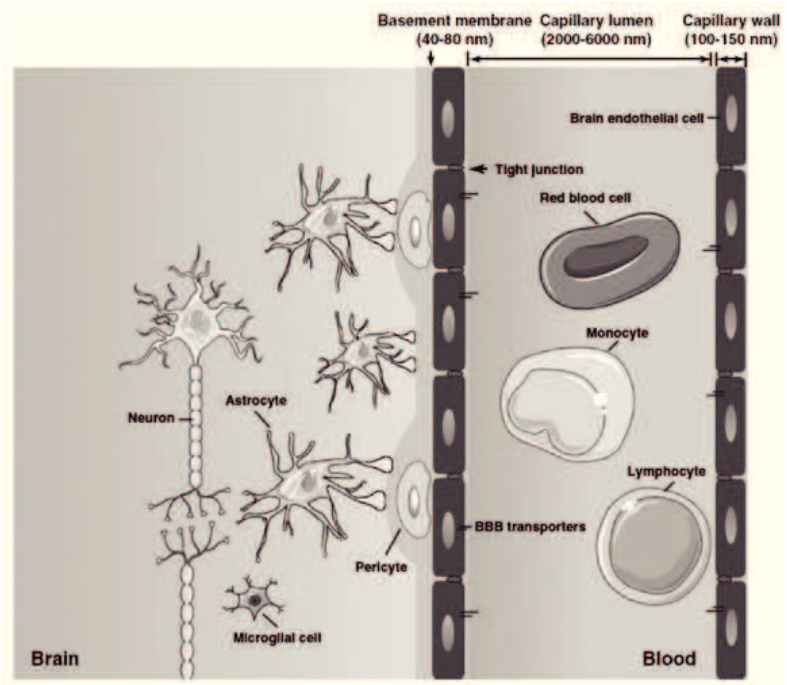

Figure 8. Schematic representation of the neurovascular unit (NVU) at the site of the brain capillaries. Adapted from ref. 149

In some brain pathologies, such as neurodegenerative disorders, tumours, bacterial infections, and stroke, the BBB is altered and becomes more permeable allowing the entry of molecules that can induce inflammatory responses and neuronal damage.[150] Actually, the mechanisms of transcytosis which occur in EC of BBB are being currently explored in order to allow the transport of therapeutic drugs into the brain. In fact, a considerable number of drugs targeted for CNS disorders, neurodegenerations, certain types of epilepsy, brain cancer, and neurological diseases have limited efficacy or even fail. For these reasons, new strategies for the delivery of drugs, neuroprotective and regenerative molecules that in normal conditions cannot pass the BBB are going to be developed nowadays. Perhaps the greatest potential that might be realized through the use of nanotechnology is the capacity of NPs to cross the BBB offering a new way for drug delivery into the brain.[151] NPs can transport drugs by adsorbing or bounding covalently to them, in such a way as to allow the drug delivery, and the control over their size, surface charge, hydrophobicity, shape, coating, and chemistry can enhance the ability of NPs to enhance BBB crossing efficiency.[152] NPs can be able to open TJs or induce short toxic effects which leads to a temporary permeabilization of the BBB, allowing the penetration of the drug,[153] or can pass through endothelium by transcytosis.[154] In this last case, several receptors have been targeted by NPs including low-density

lipoprotein receptors[155] and transferrin.[156] Moreover, they can be transported through EC by endocytosis, so that their content is released into the cell.[157]

In the present work, we move a step forward on the fabrication and biological validation of the hybrid-nanobio interface established between neurotrophin peptides and gold nanoparticles (AuNPs), which represent an attractive scaffold to construct a multifaceted drug delivery platform (Scheme 3). To enhance the image-contrast capability of the theranostic platform, the NGF- and BDNF-like peptides were dye-labelled with carboxyfluorescein (Fam) through an additional lysine (K) residue at the C-terminus, to obtain SSSHPIFHRGEFSV-K-Fam (NGFpF) and HSDPARRGELSV-K-Fam (BDNFpF), respectively.

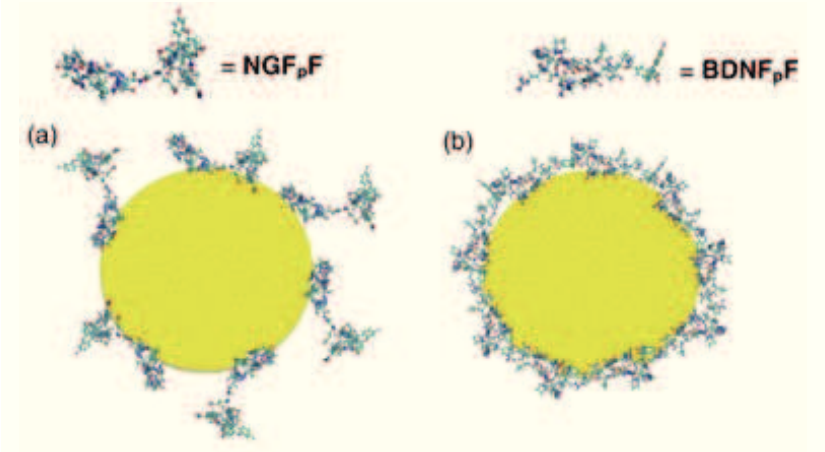

Scheme 3. Representative picture of the hybrid gold nanoparticle-peptide interface for NGFpF (a) and BDNFpF (b) peptides.

In fact, over the last decades, the interest of researchers has shifted from the study of purely molecular aspects to supramolecular architectures and nanostructures. Multicomponent systems are, in fact, an ideal platform for making nanosized functional photochemical systems that mix elementary processes (light absorption and emission, energy transfer and electron transfer) to obtain more complex processes (directional excitation energy migration, or multielectron photoinjection). In this contest, a new type of composite nanomaterial, which is a hybrid between vesicles and nanoporous silica NPs namely "*protocells*", has been described (Figure 9).[158]

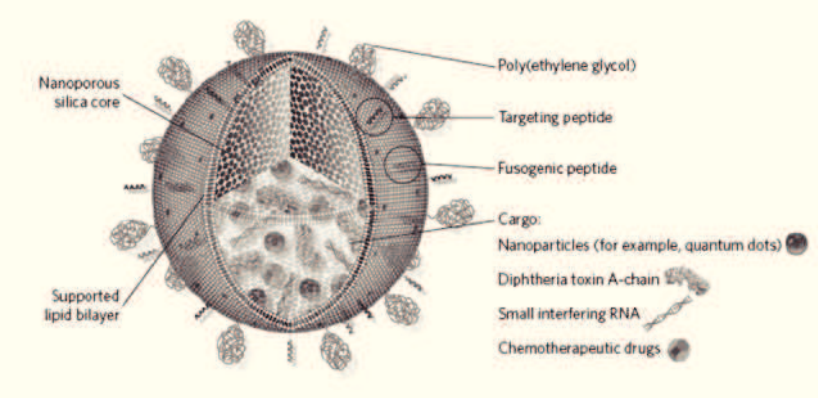

Figure 9. The design of lipid-bilayer-wrapped nanoporous silica, termed protocells. Adapted from ref. 158.

Protocells are synthesized by liposome fusion to a spherical, high-surface-area, nanoporous silica core (100 – 150 nm in diameter after size separation) characterized by an isotropic, wormlike nanoporosity to be loaded with multivariate drug cargos. The drug-loaded core is then enveloped by a single lipid bilayer (SLB), which is further functionalized with poly(ethylene glycol) (to reduce nonspecific interactions with its environment), ligands or peptides (to direct binding to distinct target cells) and pH responsive peptides, which cause disruption of endosomes and the bilayer coating on particle internalization into acidic intracellular compartments, allowing drug delivery into the cytosol of the target cell.[159] Theoretically, the protocells can absorb combinations of diverse drug cargos (quantum dots, small molecules and oligonucleotides) into their nanoporous silica cores, with reversible binding to the silica providing the means to soak up high levels of each drug cargo before enveloping the particle with its lipid shell. Targeted delivery is achieved by functionalizing the surface of NPs with ligands (proteins, nucleic acids or small molecules) that will bind to specific molecules on target cells while avoiding nonspecific binding to other cells, blood or tissue components.[160]

Many applications of these nanostructures have developed as potential application in theranostics fields. A study of hybrid interfaces established between lipids vesicles, made of cationic, anionic or zwitterionic lipids dye-doped by rhodamine and/or

nitrobenzoxadiazole, and core–shell silica NPs, dye-doped in the core with coumarin and functionalized on the outer shell with polyethylene glycol (PEG), amino-PEG and carboxyl-PEG derivatives, were prepared to scrutinize the energy-transfer processes. Promising results for the potential application of these systems as an implemented theranostic platforms have obtained.[161]

Recently, both planar silica and core–shell nanoparticles (NPs) were used as polar hydrophilic substrates to form SLBs functionalized with the $NGF_{(1–14)}$ peptide, mimicking nerve growth factors. Accordingly, a model of predominant electrostatic interactions, zwitterionic and anionic lipid vesicles were used to optimize the peptide association with the lipid membranes. Moreover, the implementation of the hybrid nanoplatforms from planar silica surfaces to 3D silica nanoparticles doped in the core with coumarin dye molecules allowed to demonstrate, by energy transfer processes, the actual wrapping of the nanoparticles by the peptide-associated supported lipid membrane.[162]

Therefore, to modulate the peptide-metal surface interaction, a dual approach was used: *(i)* the direct adsorption and, *(ii)* a lipid-mediated interaction between the peptide and the gold surfaces. In the latter case either NGF_pP or $BDNF_pF$ were loaded in small unilamellar lipid

vesicles (SUVs) of zwitterionic 1-palmitoyl-2-oleoyl-sn-glycero-3-phosphorylcholine (POPC), in order to obtain NGF_pF-PC and $BDNF_pF$-PC, respectively.

In order to test the transport of our neurotrophin peptide-functionalised gold nanoparticles across the BBB, a cellular model of immortalized Human Brain Microvascular Endothelial Cells (iHBMEC) was used. The promising potentialities in theranostics and the capability to cross the blood brain barrier have been addressed in this work.[163]

3.5.2 Samples Preparation

3.5.2.1 Gold nanoparticle synthesis.

Gold nanoparticles were synthesized in a one-step aqueous preparation by reduction method, starting from hydrogen tetrachloroaurate ($HAuCl_4$) followed by the addition of trisodium citrate dihydrate ($Na_3C_6H_5O_7$). This preparation yielded ~12 nm diameter particles with plasmonic peak at 520 nm.[164,165] Figure 10 show the fresh prepared AuNP dispersion.

Figure 10. Photograph of the AuNP dispersion obtained by a reduction method.

3.5.2.2 Lipid vesicle preparation.

Fluorescent vesicles-peptides (POPC-Rhod-peptides) were prepared from chloroform solutions of 1-palmitoyl-2-oleoyl-*sn-glycero*-3-phosphocholine (POPC) and as fluorescent probe, rhodamine-DHPE (1,2-dihexadecanoyl-*sn-glycero*-3-phosfoethanolamine) was added to solutions of lipid in a round-bottomed flask. The solvent was evaporated under a flow of argon, while rotating the round-bottomed flask, to form a film on the wall of the flask. The lipid film was emulsified in a buffer at room temperature, vortexed and extruded 13 times through a 100 nm polycarbonate membrane, followed by another 13 times through a 30 nm membrane (Figure 11).

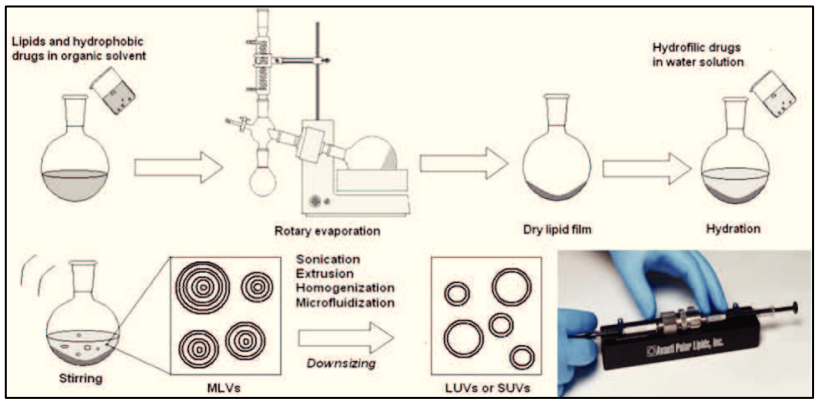

Figure 11. Lipid vesicle (POPC- Rhod) preparation. Adapted from ref. 166

To prepare small unilamellar vesicles and neurotrophin-peptides/SUV systems, the dried lipid film formed on the wall of the flask was emulsified in PBS (to obtain SUV) or 0.5 mM

peptide solution in PBS (to obtain N-Fam/SUV or B-Fam/SUV) and vortexed. The lipid dispersions were therefore extruded 13 times through a 100-nm polycarbonate membrane, followed by another 13 times through a 30-nm membrane (Avanti Polar Lipids Inc., AL, US).

To remove unloaded peptide molecules from the peptide/SUV systems, Amicon 0.5 ultracentrifuge filters (Sigma-Aldrich)[167] were used to centrifuge (14,000 r.p.m. for 30 min at 25°C) and the recovered solutions were characterized (Figure 13). The SUV and peptide/SUVs were stored under Ar and used within two weeks, according to an established protocol.[168]

Figure 12 show the obtained unloaded vesicles (in red) and the peptide-loaded vesicles (in orange).

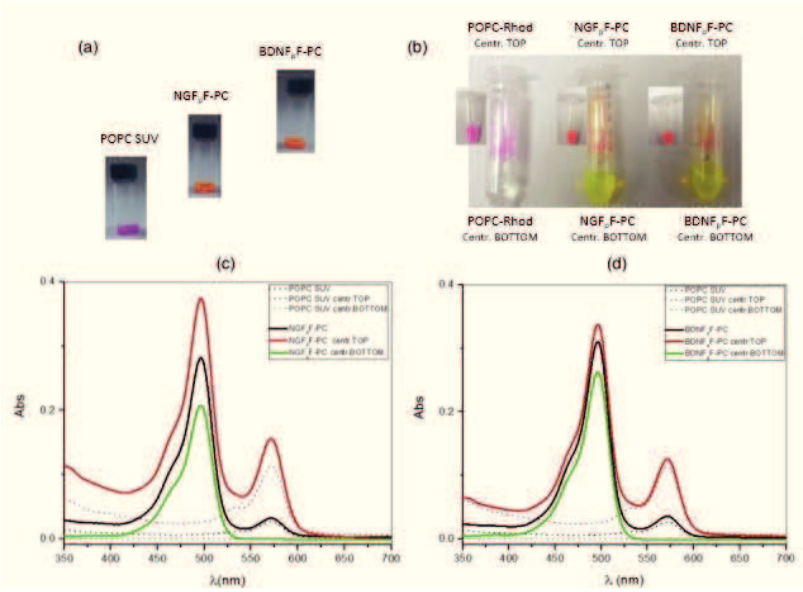

Figure 12. Preparation and optical characterisation of the Rhodamine labelled-lipid small unilamellar vesicles (SUVs) and peptide-loaded NGF$_p$F-PC and BDNF$_p$F-PC. In (a) and (b) are shown the photographs of the samples before (a) and after (b) the centrifugation with Amicon® Pro Purification System. The UV-vis spectra of the different samples are displayed in (c) for NGF$_p$F-PC and in (d) for BDNF$_p$F-PC, respectively. Submitted to Chem.Com. Ref. 163.

3.5.3 Results and discussion: characterization of peptide-AuNP nanoassemblies.

In order to study the interaction of a biomolecule with metallic nanoparticle dispersion, the shift and the shape of the gold plasmonic peak can be monitored by the UV-vis spectra as the graph below described (Figure 13).[169]

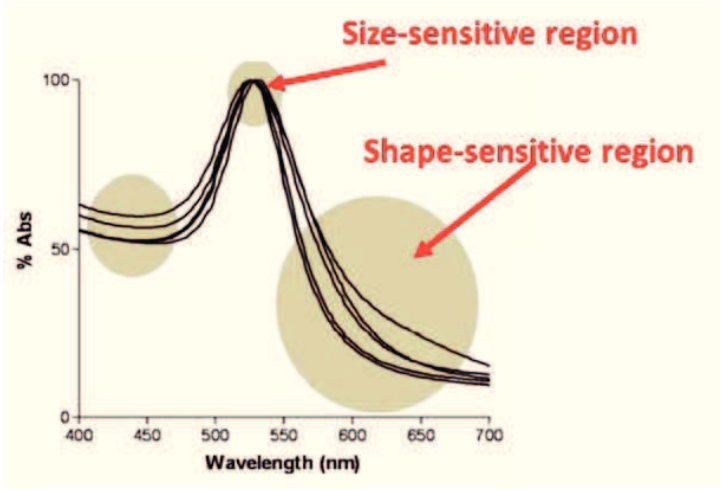

Figure 13. Typical spectra of AuNPs upon increasing concentration of a ligand which determin the changing of sizes and shapes. Adapted from ref.169.

The UV-visible titration spectra in Figure 14 show that, by the peptide addition at increasing concentrations, a red-shift of plasmonic band associated with a hyperchromic effect is obtained.

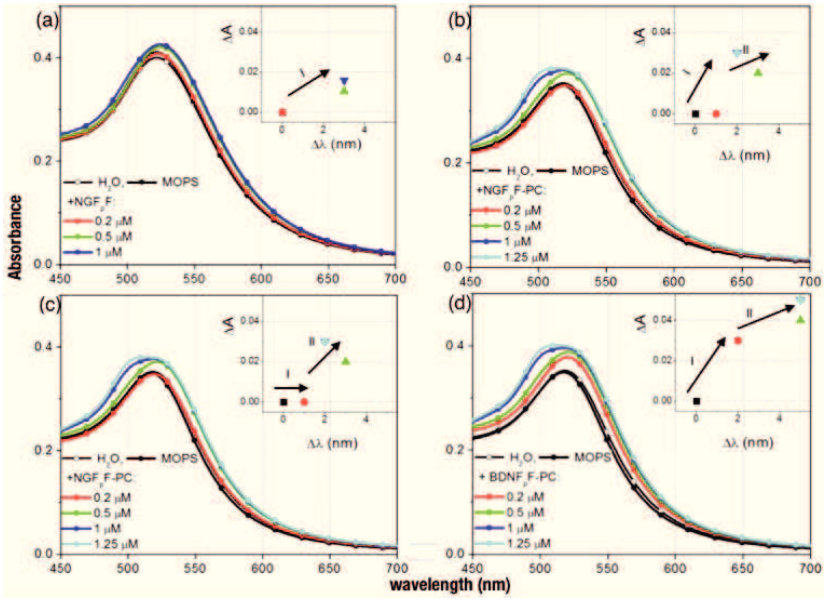

Fig. 14 - UV-visible spectra of AuNPs (2.2 nM) before (in water and in MOPS buffer) and after the addition at increasing concentrations ($2x10^{-7}$ M–$1.2x10^{-6}$ M range) of: (a) NGF_pF; (b) $BDNF_pF$; (c) NGF_pF-PC; (d) $BDNF_pF$-PC. In the insets: ΔA-Δλ scatter plots, with arrows drawn to guide the eye to subsequent adsorption steps (I, II). Submitted to Chem.Com. Ref. 163.

The parallel occurrence of these two spectral features is generally attributed to the size increase of the colloidal metal owing to, *e.g.*, the 'decoration' of the nanoparticle surface by adsorption of molecules. Therefore, a hybrid assembly comprising a metal core (AuNP) surrounded by a soft shell (peptide molecules) can be figured out.

The saturation in the shifts of wavelength (Δλ) and absorbance (ΔA) is reached at the peptide concentration of 0.5 μM for NGF_pF and 1 μM for $BDNF_pF$, NGF_pF-PC and $BDNF_pF$-PC,

respectively. The corresponding coverage, in terms of peptide molecules for each gold nanoparticle, is calculated of about $1.2x10^7$ for NGF_pF and about $2.4x10^7$ for $BDNF_pF$, NGF_pF-PC and $BDNF_pF$-PC, respectively.

As to the direct peptide-AuNP interaction (Fig. 14a-b), the plots of ΔA versus $\Delta\lambda$ exhibit a direct one-step change for NGF_pF but a two-step change for $BDNF_pF$ (see insets). Therefore, for NGF_pF/AuNP and $BDNF_pF$/AuNP, the measured curve shifts likely depend on different stages in the peptide adsorption process, in turn related to diverse orientation/conformation of the molecules at the interface with the gold nanoparticle surface. Such a finding is in agreement with dissimilar affinities of the two peptides towards the Au surface, as demonstrated for NGF and BDNF peptides at the interface with flat gold, resulting into viscoelastic and rigid adlayers, respectively. [170,171]

By taking into account the ideal monolayer coverage, 'disordered' multilayers of NGF_pF molecules in side-on/end-on configuration (Scheme 3a) and more packed adlayers of $BDNF_pF$ molecules most likely in side-on configuration can be figured out at the interface with AuNP (Scheme 3b).

As to the lipid-mediated peptide/AuNP interaction (Fig.14c-d), a significant synergic effects from each component, i.e., peptide/lipid/AuNP, is monitored at the hybrid nano-biointerface. Firstly, for NGF_pF-PC, the peptide concentration at equilibrium, i.e., the value corresponding to the saturation in the

plasmonic peak shifts, rises up to 1 μM. This fact suggests an active role by the fluid lipid membrane in the confinement of NGF peptide at the interface with the gold surface. Such an effect would prompt a more 'ordered' interaction with AuNPs, and therefore a higher number of molecules detected by the plasmonic sensing. Secondly, the insets in Fig. 14c-d show also a peptide-driven effect, because both $\Delta\lambda$ and ΔA are narrower for NGF_pF-PC than for $BDNF_pF$-PC, similarly to what observed for NGF_pF and $BDNF_pF$, respectively. Thirdly, the UV-visible spectra of pellets and supernatants recovered after centrifugation demonstrate a lower nanoparticle aggregation for peptide-loaded SUVs/AuNP in comparison with POPC SUVs (without peptide)/AuNP systems.

The comparison between pellet and supernatant spectra of peptide-functionalised AuNP shows similar band shapes; therefore, at the used experimental conditions, an almost totally irreversible adsorption can be deduced for NGF_pF and $BDNF_pF$ in the direct interaction with the AuNPs. On the other hand, for the lipid-mediated interaction, the spectra of supernatants clearly display the spectral features of free peptides and/or peptide-PC systems, indicating that a partially reversible adsorption occurred. This finding points to the possibility, through the lipid-mediated interaction, to modulate the actual peptide coating onto AuNPs.

Zeta potential (ZP) analyses confirm the full nanoparticle coverage after the peptide adsorption process. Indeed, the bare gold nanoparticles, negatively charged in water (ZP ~ - 60 mV), and still anionic but less negative in MOPS (ZP ~ - 40 mV), become even less negative after the interaction with the lipid vesicles (ZP of POPC SUV/AuNP ~ - 13 mV). The ZP increase for AuNPs in MOPS is explained in terms of the partial charge neutralisation of citrate anions surrounding the metal core by the Na^+ and K^+ ions used to fix the ionic strength of the buffer. In the case of POPC SUV/AuNP, the ZP increase is a likely marker of only a partial coverage, if any, of the gold nanoparticles by the lipid molecules. On the other hand, all the other samples, i.e., those containing the peptides, exhibit an almost null surface charge, thus confirming the complete nanoparticle coating. Accordingly, atomic force microscopy (AFM) analyses of NGF_pF/AuNP and $BDNF_pF$/AuNP samples (Figure 15) clearly show a size increase for the peptide-functionalised AuNPs, with a broader diameters distribution in NGF_pF/AuNP than in $BDNF_pF$/AuNP samples, respectively.

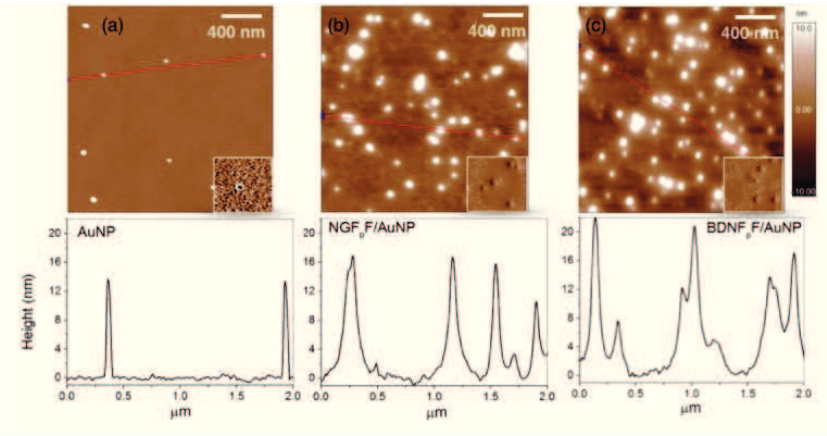

Figure 15. AFM topography images and height section of: (a) bare AuNP; (b), NGF$_p$F/AuNP and (c) BDNF$_p$F/AuNP. Z –scale = 20 nm. In the inset a representative detail of the corresponding phase image for each sample. Submitted to Chem.Com. Ref. 163.

Also dynamic light measurements (DLS) results point to diverse increases in the hydrodynamic diameter, D: from 26±2 nm (bare AuNP, both in water and in MOPS) to D=250±30 nm for NGF$_p$F/AuNP and D=75±3 nm for BDNF$_p$F/AuNP. Interestingly, NGF$_p$F-POPC exhibit a higher average diameter (D=122±2 nm) than BDNF$_p$F-POPC (D=104±3 nm), which instead are comparable in size than the control SUVs without peptide (D=108±5 nm). Such a finding confirms the NGF$_p$F tendency to 'end-on'-like arrangement, whereas BDNF$_p$F is more likely lying flat at the leaflet plane of the lipid membrane. As to the peptide-PC/AuNP samples, D values respectively of 173±34 nm for POPC SUV/AuNP, 172±28 nm for NGF$_p$F-PC/AuNP and 83±7 nm for BDNF$_p$F-PC/AuNP, reveal

comparable average size distributions of BDNF-functionalised AuNP, both for direct and for lipid-mediated interaction. This finding is in agreement with the similar saturation shifts in the plasmonic shifts showed in Fig. 14b and 14d. On the other hand, a significant particle aggregation can be deduced for NGF_pF as well as bare AuNPs at the interface with the lipid membranes.

The physicochemical characterisation of NGF_pF/AuNP and $BDNF_pF$/AuNP samples provided by X-ray photoelectron spectroscopy (XPS) further confirms the picture figured out for the hybrid interfaces formed for the two peptides (Figure 16).

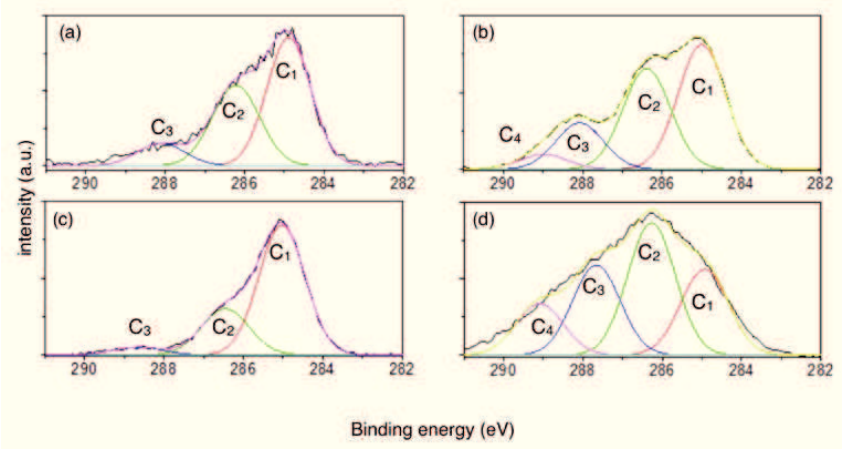

Figure. 16. XPS peaks of C 1s for: (a) NGF_pF/AuNP, (b) NGF_pF, (c) $BDNF_pF$/AuNP, (d) $BDNF_pF$. Submitted to Chem.Com. Ref. 163.

For the peak fitting analysis of C 1s, the following four components have been considered: C_1 (at binding energy, BE, of 285.0 eV), due to C-C and C-H hydrocarbon bonds; C_2 (at BE of 286.2±0.2), assigned to heterocarbon C-O and C-N bonds; C_3

and C_4, at BE of 288.2±0.2 eV and 289.0±0.2 eV, corresponding to C=O and C(=O)OH groups, respectively.

Intrinsic structural differences due to the primary peptide sequence are clearly displayed in the carbon peak components found for NGF_pF (Fig. 16b) and $BDNF_pF$ (Fig. 16d). In fact, the former exhibits a ratio of polar to apolar components (C2+C3+C4)/C1 of 1.3 for NGF_pF, whereas of 3.2 for $BDNF_pF$. These finding is explained according to the two extra amino acids in NGF_pF, and also two more phenylalanine residues in comparison with $BDNF_pF$, which instead encompasses both one carboxylic residue and one guanidine extra residue.

Interestingly, the comparison of C 1s spectra for NGF_pF/AuNP (Fig. 16a) and $BDNF_pF$/AuNP (Fig. 16c) samples suggest that the BDNF peptide molecules bind to the gold surface predominantly through the guanidine, carbonyl and carboxyl groups (i.e., strong decrease of C_2, C_3 and C_4 components, respectively), according to the picture of molecules lying at the interface in the extended side-on arrangement. In the case of NGF peptide, a minor change in the peak shapes can be an indicator of a more localised interaction among certain sites of the peptide sequence and the gold nanoparticle, which results in a less ordered hybrid interface.

In order to test the transport of neurotrophin peptide-functionalised AuNPs across the BBB, a cellular model of immortalized Human Brain Microvascular Endothelial Cells

(iHBMEC) was used. No toxicity was found up to 24 h of cell treatments. Figure 17 shows representative images of laser scanning confocal microscopy (LSM) for cells incubated for 2 h with NGF_pF and $BDNF_pF$ (emitting in the green, due to Fam moieties): free (Fig.17a), immobilised on AuNPs by direct adsorption (Fig. 17b), loaded in rhodamine-labelled POPC SUVs (emitting in the red) (Fig. 17c) and immobilised on AuNPs by lipid-mediated adsorption (Fig. 17d).

A visible enhancement of peptide internalisation by the cells in the functionalised AuNPs in comparison to both free peptides and peptide-loaded SUVs was observed. Interestingly, for NGF_pF/AuNP a higher peptide uptake (displayed by a diffuse green emission in the cytoplasm) and intracellular aggregation of the gold nanoparticles (dark spots in the optical micrograph, see open arrows in Fig. 17b), was found in comparison with $BDNF_pF$/AuNP. This latter exhibits a more localised distribution (dotted green emission) with a preferential localisation at the cell membrane (see solid arrow in Fig. 17b). As to NGF_pF-PC/AuNP and $BDNF_pF$-PC/AuNP systems, the cellular internalization is comparable for both peptides, with green spots co-localising with the gold nanoparticles, also in the nuclei.

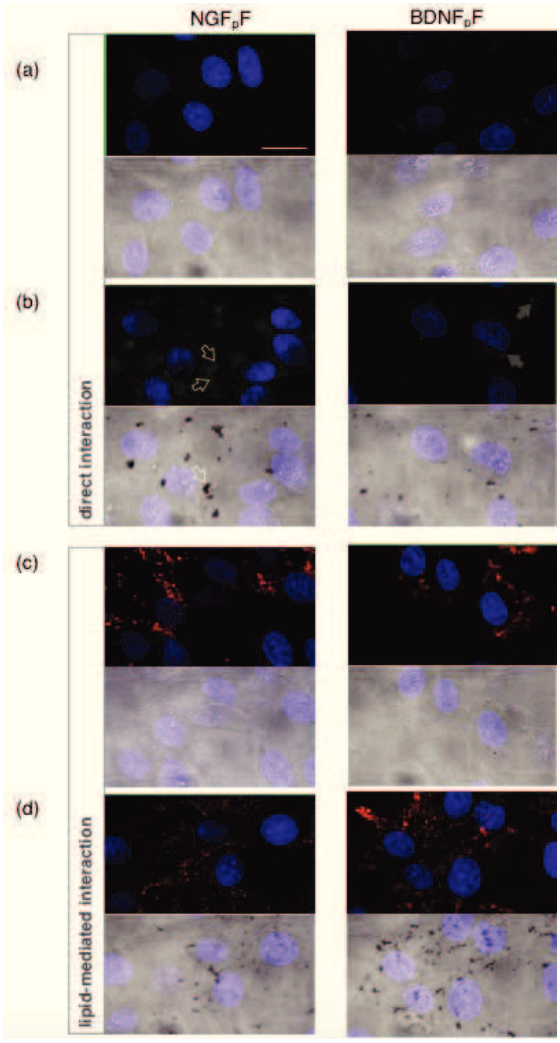

Fig. 17. LSM micrographs of iHBMECs incubated for 2 h (37°C, 5% CO_2) with: (a) NGF$_p$F(or BDNF$_p$F); (b) NGF$_p$F(or BDNF$_p$F)/AuNP; (c) NGF$_p$F-PC(or BDNF$_p$F-PC); (d) NGF$_p$F-PC(or BDNF$_p$F-PC)/AuNP. Scale bar = 20 μm. For each sample: the merged fluorescence images of nuclei (blue, DAPI, $\lambda_{ex/em}$=405/425-475 nm), peptides (green, Fam; $\lambda_{ex/em}$=488/500-530 nm) and lipids (red, Rhodamine; $\lambda_{ex/em}$=543/550-650 nm) (top); the merged DAPI emission and optical bright field images (bottom). Submitted to Chem.Com. Ref. 163.

3.5.4 Conclusions.

In this work, we set up a new promising approach to develop a 'tunable' theranostic platform based on a neurotrophin-like potential drug (NGF and BDNF peptides) and a plasmonic/fluorescence image contrast working principle. A modulation in the peptide immobilisation was demonstrated by the comparative study (by UV-visible, AFM, DLS, ZP analyses) of direct vs. lipid-mediated peptide-AuNP interaction.

3.5.5 Future Perspectives.

Further physicochemical and biological (including *in vivo test)* works will be necessary on these hybrid nanobiointerfaces to finely control the sub-cellular localisation of the drug and the resulting efficiency in crossing the BBB.

3.6 An tunable anti-angiogenic nanoplatform based on VEGF peptide and gold nanoparticles: a physicochemical study of covalent vs. physical adsorption immobilisation approaches.

3.6.1 The balance of pro-/anti-angiogenic properties of gold nanoparticles functionalised with a VEGF peptide.

The proliferation mediated by growth factors and, more in general, angiogenesis has a central role in many pathological conditions including neoplasia, rheumatoid arthritis, wound healing, and chronic inflammation. Parental vascular endothelial growth factors (VEGF-A) was discovered more than a decade ago.[172] They are known as key regulators of physiological angiogenesis.[173,174] Among all conditions, hypoxia-inducible factor (HIF) regulates the expression of VEGF-A (Figure 18).[175]

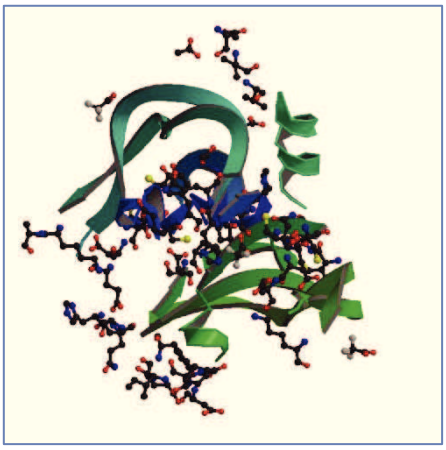

Figure 18. Cristal structure of the mirror image form of VEGF-A. Adapted from ref. 176

The VEGF family of growth factors, including also VEGF-B, VEGF-C, VEGF-D, placenta growth factor (PLGF) and platelet-derived growth factor (PDGF), are polypeptides belonging to the cysteine-knot superfamily of signalling proteins. All VEGFs bind to and activate the VEGF receptors, i.e. VEGFR-1, VEGFR-2 and VEGFR-3, mainly expressed by endothelial cells, but displaying different and overlapping binding patterns.[177]

Four isoforms of VEGF-A, containing 121, 165, 189, and 206 amino acids, are produced from a single gene as a result of alternate splicing.[178,179] The most abundantly expressed splice variant is $VEGF_{165}$: a heparin binding glycoprotein with a single glycosylation site (at Asn75), secreted as a homodimer of approximately 45 KDa and cleaved by plasmin to yield $VEGF_{110}$, which is equipotent to $VEGF_{121}$ with respect to mitogenic activity on endothelial cells.[180] The 121 amino acid form of VEGF induces the proliferation of endothelial cells but, in contrast to $VEGF_{165}$, lacks the heparin binding ability. Only a small number of VEGF residues are important for the binding to VEGF receptors. Particularly, the positively charged domain of VEGF encompassing Arg82, Lys84 and His86, located in a hairpin loop, and a negatively charged residues Asp63, Glu64 and Glu67 resulted responsible for the respectively binding of VEGFR-1 and VEGFR-2 receptors, [181] and also for the angiogenic response.[182]

Many antiangiogenic approaches have been developed to block the interaction of VEGFs with their receptors in order to inhibit angiogenesis and tumor growth. Many VEGF mimetic peptides with antiangiogenic activity have been described,[183] while very few molecules with pro-angiogenic activity have been reported.[184]

Furthermore, angiogenesis may be influenced by the presence of copper(II) ions and many pro-angiogenic proteins have been reported to be copper dependent.[185] Copper regulates the production of VEGF, not only *via* the activation of transcription factor regulating its expression,[186] but also *via* the exploiting of copper chelators in anti-angiogenesis therapy.[187] Recently, Grasso et al.[188] reported how Cu^{2+} influence the biological features of VEGF mimicking peptides, scrutinizing the interaction between copper(II) and VEGF peptide fragments as VEGF73-101 and VEGF84-101.

Inorganic nanoparticles discovered to have anti-angiogenic properties even if the mechanism is unknown. Different sizes and surface charges influenced the intracellular signalling events. Particularly, AuNPs and AgNPs seemed to inhibit the function of pro-angiogenic heparin-binding growth factors (HB-GFs), such as VEGF165 and basic fibroblast growth factor (bFGF), etc.[189,190] VEGF121 does not have a heparin binding domain and hence was not inactivated by gold nanoparticles.

Therefore, AuNPs selectively inhibited VEGF165-induced proliferation of HUVEC cells.[191]

In the present work, we studied the immobilization of $VEGF_{73-101}$ peptides labelled with 5,6-carboxyfluorescein (VEGF-FAM) on AuNPs through *i)* indirect physisorption of the VEGF73-101 peptide (VEGF-FAM/Au) and *ii)* a direct chemisorption mediated by the mutated residue 88 with a cysteine (Cys) instead of the Glycine (Gly) in the $VEGF_{73-101}$ peptide ($VEGF_{Cys}$FAM/Au). To best of our knowledge, this is the first work dealing with the functionalization of gold nanoparticles with a VEGF peptide as enhanced anti-angiogenic nanomedicine to trigger uncontrolled neovascularization.

3.6.2 Results and discussion

The synthesis of gold nanoparticles, carried out by chemical reduction method with citrate acting both as reducing and stabiliser agent[35], results, at the used experimental conditions, in a monodisperse colloidal solution of spherical nanoparticles having diameter of 12 nm and a plasmonic band centered at 518 nm.[163]

As described in Section 3.5.3, a red shift and broadening of the gold plasmonic peak upon the addition of the peptides can be

used to quantify the surface coverage and/or aggregation of the metal nanoparticles.

Figure 18a-b displays the red shifts dominated in the 25 nM - 125 nM concentration range of added peptide, with total shifts measured of 10 nm for $VEGF_{Gly}FAM$ and 6 nm for $VEGF_{Cys}FAM$, respectively.

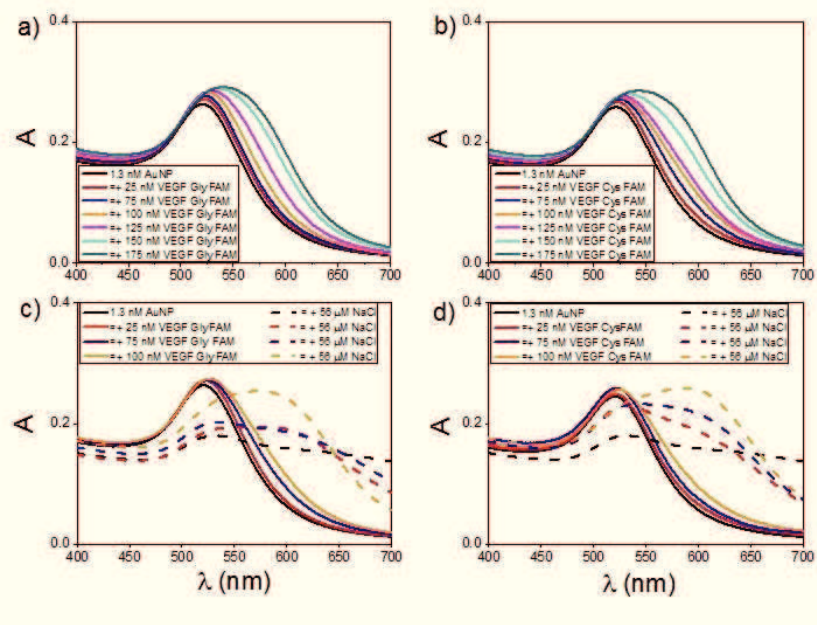

Figure 18. UV-visible spectra of 1.3 nM AuNPs by addition of $VEGF_{Gly}FAM$ (a) and $VEGF_{Cys}FAM$ (b) at increasing concentrations (from $2.5x10^{-8}$M to $17.5x10^{-8}$M). In (c) and (d) are shown the spectra of bare and peptide-coated AuNPs upon the addition of 56 µM NaCl.

In the concentration range between 125 nM and 175 nM, the width of the plasmonic bands increase up to FWHM of 130 nm compared to 81 nm for the bare AuNPs. Such findings were

explained both in terms of a predominant particle coverage by the peptide molecules in the lower concentration range, and a predominant colloidal aggregation in the higher concentration range, respectively. To confirm this hypothesis, the flocculation assay by addition of an electrolyte solution (56 μM NaCl) has been performed for the gold nanoparticle-peptide assemblies formed in the 25-100 nM range of peptide concentration. Figure 18c-d show that the addition of 75 nM $VEGF_{Gly}FAM$ and 25 nM $VEGF_{Cys}FAM$ were enough to stabilise the gold colloids, which exhibit a decrease in the intensity of the plasmonic intensity respectively of 30%, 26%, and 9% for bare, $VEGF_{Gly}FAM$- and $VEGF_{Cys}FAM$-coated nanoparticles. It was therefore inferred that the cysteine residue was more effective as anchoring site to the metal nanoparticle surface than the glycine residue, thus owing the chemisorption forces that complement the energy balance of the peptide adsorption at the nanoparticle surface.

In order to remove the loosely bound and/or free peptide molecules from the peptide-coated NPs, a centrifugation step was performed and the supernatant and the pellet obtained were characterized. The pellets were widely characterized by using spectroscopic (UV-Vis, FT-IR, XPS), spectrometric (TOF-SIMS) and microscopic (AFM, SEM) analyses. Moreover, the hydrodynamic size and the surface charge of the hybrid peptide-gold nanoparticles were monitored by DLS and Z-potential measurements, respectively.

Figure 19 shows the TEM images of the re-suspended samples. The nanoparticles were well-dispersed with an average dimension of 30 nm, as dynamic light scattering analysis confirmed. Instead, the average size of hydrodynamic diameter for functionalized AuNPs/VEGF$_{Cys}$FAM reached ~159.3±11.9 nm in comparison to AuNPs/VEGF$_{Glu}$FAM (~67.4±0.8 nm). Also, it was possible to note a shell around the grouped nanoparticles suggesting the effectively coating of the peptide at the nanoparticles surface. On the other case, AuNPs/VEGF$_{Gly}$FAM image did not clearly evidence the same coating, but only a slight increasing of the average dimensions.

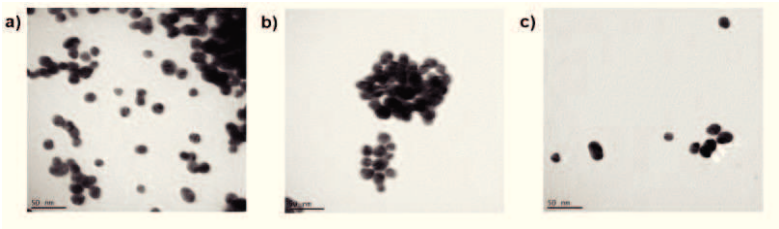

Figure 19. TEM images (scale bar = 50 nm) of bare AuNPs (a), AuNPs/VEGF$_{Cys}$FAM (b) and AuNPs/VEGF$_{Gly}$FAM (c).

Other evidences of the effectively functionalization of AuNPs is the changing of ζ-potential as the histogram below displayed. Bare NPs indicated an average ζ-potential of ~ -46.6 mV that were almost neutralised by peptides immobilization (ζ-potential ~-7.7 mV and 4.4 mV for AuNPs/VEGF$_{Gly}$FAM and AuNPs/VEGF$_{Cys}$FAM, respectively).

FT-IR spectra were employed to detect the characteristic bands of AuNPs before and after the peptide conjugations (Figure 20). Both $VEGF_{Cys}FAM$ and $VEGF_{Gly}FAM$ peptides exhibited very similar spectral features, with the characteristic vibrational modes of amide I and II (1666-1450 cm^{-1}), N−H (a sharp band around 3276 cm^{-1}), C=O (1737 cm^{-1}), C-O (1245 cm^{-1}), aliphatic CH_2 (1313 cm^{-1}) and C-H (1278 cm^{-1}), respectively. However, in the case of $VEGF_{Cys}FAM$ did not evidence the characteristic peak of thiol group related to cysteine residue as the inset shown. FT-IR spectra were strongly affected after AuNP conjugation. Particularly, the characteristic features were still visible but less evidence; also, a shift in the position of COO^- (asymmetric ~1629 cm^{-1} and symmetric ~1405 cm^{-1}) and NH_3^+ stretching was likely due to a change in their dipole moment when peptides physisorption or chemisorption on metal surface with high electron density.

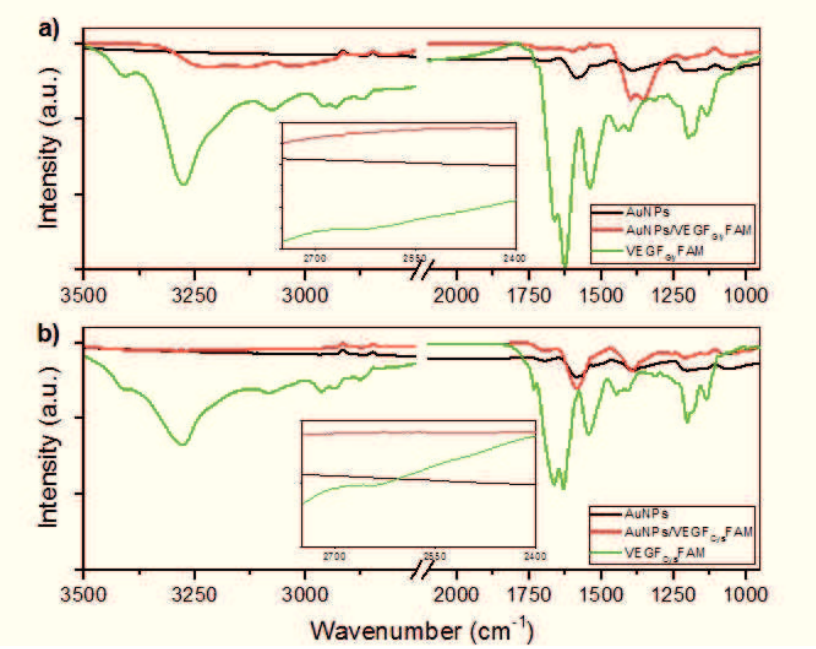

Figure 20. FT-IR spectra of the bare gold nanoparticles (line black), the unbound peptide (line green) and the AuNP/peptide systems (line red) for VEGFGlyFAM (a) and VEGFCysFAM (b), respectively. In the inset: the magnified 2750-2400 cm^{-1} region.

In order to obtain information about the functionalization and the chemistry of modified nanoparticles, XPS and ToF-SIMS measurements were performed.

The atomic percentage composition of AuNPs before and after the coating with peptides showed in Table 1, demonstrate that the bare AuNPs a relatively high amount of C1s and O1s that hide the Au4f signal. This finding was attributed to a thick adlayer of citrate ions coating the metal core of the nanoparticles.

Table 1. Surface atomic composition of AuNPs before and after the functionalization with peptides.

	C1s (at.%)	O1s (at.%)	S2p (at.%)	N1s (at.%)	Au4f (at.%)
Bare AuNPs	54.6	34.3	-	-	11.1
AuNPs/$VEGF_{Cys}$FAM	8.0	3.6	1.0	0.0	87.4
$VEGF_{Cys}$FAM	66.7	18.5	2.0	12.9	-
AuNPs/$VEGF_{Gly}$FAM	9.5	4.5	0.9	1.5	83.7
$VEGF_{Gly}$FAM	67.3	15.7	1.6	15.3	-

Accordingly, due to the replacement of the citrate shell by the peptide molecules adsorbing at the interface, the atomic concentration for Au4f increases. It must be noted that no traces of N1s and S2p were detected at the surface of bare AuNPs, whereas, after the coating by the peptides, comparable amounts of sulphur were found for both AuNPs/$VEGF_{Gly}$FAM and AuNPs/$VEGF_{Cys}$FAM.

The S2p high-resolution spectra of the two peptides, both free and bound to the gold nanoparticles are shown in Figure 21. The peak deconvolution has been performed according to the presence of a doublet corresponding to the $S2p_{3/2}$ and $S2p_{1/2}$ components, at a relative distance each from the other of 1.2 eV and with an intensity peak ratio, $S2p_{3/2}/S2p_{1/2}$, of about 2:1. The higher binding energy (BE) component $S2p_{3/2}$ has been assigned to the following chemical states of sulphur: S-Au bonds, at BE=161.3 ±0.2 eV[192,193] (S0 component); S-C bonds, e.g. in cysteine and methionine residues, at BE=163.5 ±0.2 eV[194] (S1 component); S-O bonds, at increasing oxidation levels,

respectively at BE= 166.3 ±0.2 eV[192] (S2 component); 168.4 ±0.2 eV (S3 component) and 170.7 ±0.2 eV (S4 component).[195]

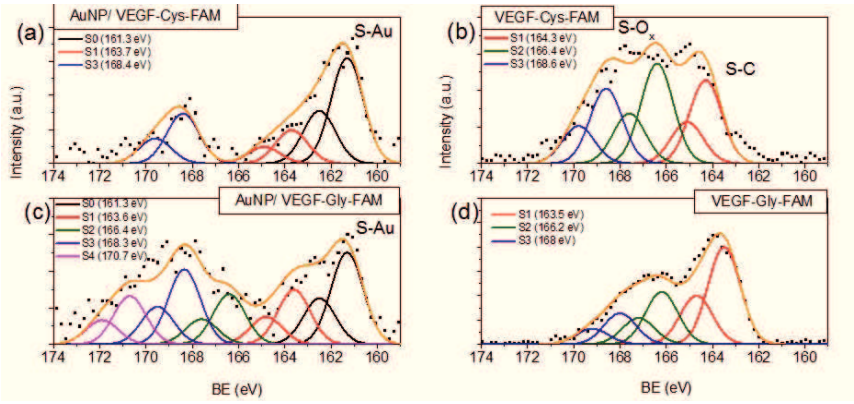

Figure 21. Representative high resolution spectra of S2p of bare AuNPs (a), AuNPs/VEGFcysFAM (b), AuNPs/VEGFglyFAM (c) and VEGFcysFAM (d), VEGFglyFAM(e) peptides, respectively.

Interestingly, although the free peptides exhibit different peak shapes, the peak fitting analysis resulted in the same components of the S2p peak, i.e., S1, S2 and S3, at different relative intensity ratio. Specifically, the S1/(S2+S3) ratio is 1.2 for VEGF-Gly-FAM and 0.3 for VEGF-Cys-FAM. This finding can be explained by the tendency of cysteine groups to oxidise in a non-reducing environment[196] As to the peptides bound to the AuNPs, for both AuNP/VEGF-Gly-FAM and AuNP/VEGF-Cys-FAM the component S0 of chemisorbed sulphur is found. In the case of the peptide containing the cysteine such a component is expected owing to the high binding affinity of thiol groups towards metal surfaces.[195] On the other hand, in the methionine

residue, the presence of electron pairs of the sulphur 2p orbitals is likely to prompt, e.g., by coordinative binding, the formation of S-Au bonds corresponding to S0 component. It must be noted that the relative intensity ratio between the components assigned respectively to chemisorbed sulphur (S-Au) and S-C bonds, correspond to the S0/S1 values of 3.1 for AuNP/VEGF-Cys-FAM and 1.7 for AuNP/VEGF-Gly-FAM, thus confirming the higher chemisorption process occurred in the presence of the cysteine residue. As to the overall oxidation state of sulphur in the AuNP/peptide assemblies, the values of the intensity ratio S1/(S2+S3+S4) of 0.7 for AuNP/VEGF-Cys-FAM and 0.3 for AuNP/VEGF-Gly-FAM point to a less extent of oxidation of the sulphur moieties for the nanoparticle-bound peptide in comparison to the free peptide in the case of VEGF-Cys-FAM.

The ToF-SIMS technique has been extensively used to study the interaction of biomolecules with surfaces including nanofilms and nanoparticles, often as complementary tool of XPS studies.[197]

The Principal Component Analysis (PCA) method[198] used to wisely analyse the ToF-SIMS spectra, and the corresponding results are shown in Fig. 22. In this plot, each individual point represents the ToF-SIMS spectrum acquired at a specific location of the sample. PC1, represented on the vertical axis, from the PCA study of positive ToF-SIMS spectra for AuNP, AuNP/VEGF peptide and VEGF peptide samples reveals that

the bare AuNP and the peptide-coated AuNP samples are clearly discriminated, i.e. located in distinct regions (i.e., PC1<0) with respect to the free peptide one (PC1>0). This results is found for both for $VEGF_{Gly}FAM$ (left hand side panel) and $VEGF_{Cys}FAM$ (right hand side panel), respectively.

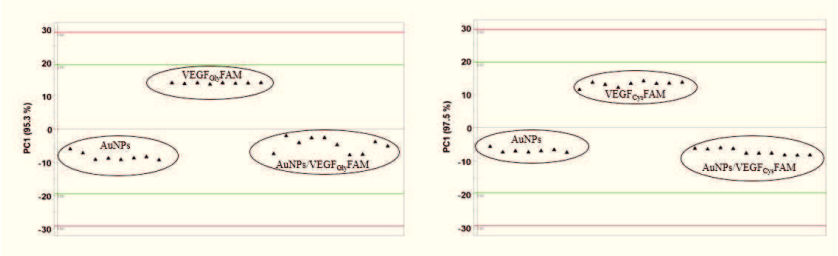

Figure 22. Score Plot obtained from PCA analysis of positive ToF-SIMS spectra (at least five spectra for each sample) of functionalized AuNPs with $VEGF_{Gly}FAM$ peptide (on the right) and $VEGF_{Cys}FAM$ (on the left).

In Fig. 23 is displayed a second PCA model, which takes into account only the spectra recorded from bare and peptide-functionalised AuNP samples.

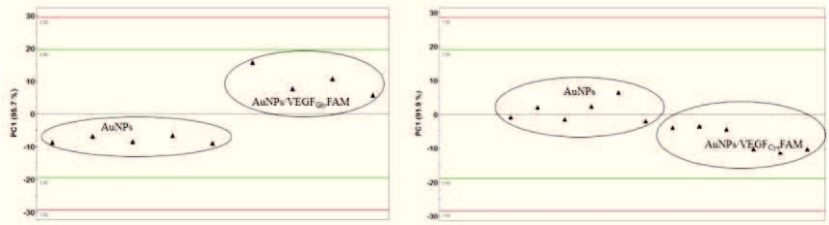

Figure 23. Score Plot obtained from PCA analysis of positive ToF-SIMS spectra (at least five spectra for each sample) of bare and functionalized AuNPs with $VEGF_{Gly}FAM$ peptide (left hand side panel) and $VEGF_{Cys}FAM$ (right hand side panel).

The score plots showed in Fig 23 well discriminate between two samples, and a higher separation is obtained for the ensembles of PC1 values of AuNP vs. AuNP/VEGF$_{Gly}$FAM than those of AuNP vs. AuNP/VEGF$_{Cys}$FAM. According to the picture figured out from UV-visible and XPS analyses, this finding is explained in terms of the higher peptide coverage of the gold nanoparticles by VEGF$_{Gly}$FAM with respect to VEGF$_{Cys}$FAM.
Preliminary experiments of cellular uptake of AuNPs, both bare and peptide-functionalised, were performed in HUVECs by confocal microscopy (LSM) in order to investigate the potential application of these smart nanosystems as potential theranostic nanoplatform. Figure 24 shows the highest cellular internalisation of peptide for AuNP/VEGF$_{Cys}$FAM, as visible by the green emission of the FAM moiety covalently bound to the peptide sequence; it must be noted that this fluorescence mostly co-localises with the dark spots in the optical image (due to metal nanoparticles aggregates), thus confirming the strong chemisorption of the peptide containing the cysteine residue onto the AuNPs. On the other hand, a lower green fluorescence but still co-localised with AuNPs, is detected for AuNP/VEGF$_{Gly}$FAM, according to the weaker binding of this peptide to the nanoparticle surface. No significant peptide uptake could be detected for the free VEGF$_{Gly}$FAM (75 nM) nor VEGF$_{Cys}$FAM (25 nM and 75 nM).

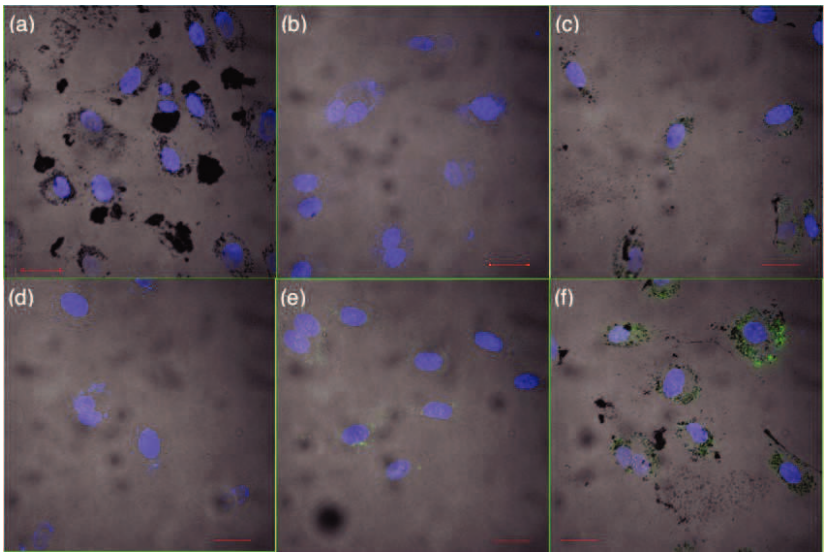

Figure 24. LSM merged micrographs of fluorescence (blue: DAPI; green: FAM) and optical bright field of HUVECs 24-hours treated with 2.5 nM bare AuNP (a); (b) 75 nM $VEGF_{Gly}FAM$; (c) AuNP/$VEGF_{Gly}FAM$; (d) 25 nM $VEGF_{Cys}FAM$; (e) 75 nM $VEGF_{Cys}FAM$; (f) AuNP/ $VEGF_{Cys}FAM$.

Moreover, the cells incubated for 24 h (37°C, 5% CO_2) with 2.5 nM AuNP, 25 nM $VEGF_{Cys}FAM$, 75 nM $VEGF_{Gly}FAM$ and the corresponding hybrid composites did not exhibit any toxicity.

3.6.3 Conclusions.

We were able to functionalize gold nanoparticles by the peptide fragment VEGF73-101 by exploiting two different approaches of adsorption, namely physisorption or chemisorption. The peptide-functionalized AuNPs were scrutinised by different spectroscopies (UV-visible, FTIR, XPS), spectrometric (ToF-

SIMS) and microscopic (TEM, LSM) techniques. The promising potentialities in the nanoparticle-driven cellular uptake of the peptide were demonstrated.

3.6.4 Future work

We explained at the begging the importance of copper(II) ions in the angiogenesis development and as the copper can regulate the production of VEGF. Further studies will carry out to scrutinize the possible interaction of VEGF73-101 peptide/AuNP hybrid systems with the copper(II) ions either in solution or in vitro cellular environments.

3.7 Silver nanoparticles functionalized with a fluorescent cyclic RGD peptide: a versatile integrin targeting platform for cells and bacteria

In this paper, we addressed fabrication of a smart nanodevice to specifically target cancer cells which are generally characterized by an over-expression of specific receptors (Figure 26).

-

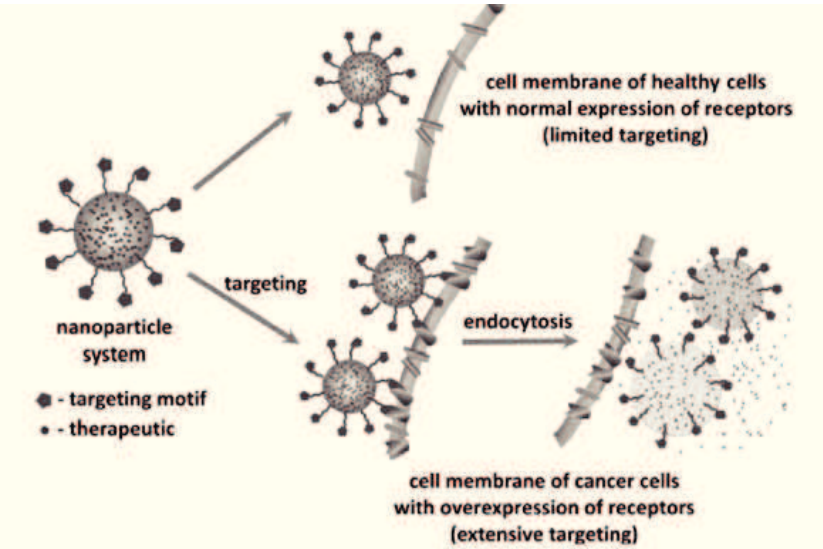

Figure 26. Drug delivery strategy to target cancer cells. Adapted from ref. 199

Among them, *integrins* are well-known cell adhesion receptors involved in several important functions for the survival of cells, *e.g.*, receptor for extracellular matrix (ECM) proteins, immunoglobulin, growth factors, cytokines, and matrix-

degrading proteases. Integrins mediate adhesive events during various cancer stages such as malignant transformation, tumor growth and progression, invasion, and metastasis.[200]

3.7.1 Integrin receptors and targeting strategies

Integrins can be classified based on their properties or based on their subunit composition. The integrin family comprises 24 transmembrane receptors: a divalent cation-dependent heterodimeric membrane glycoproteins composed of non-covalently associated α- and β-subunits (18 α- subunits and 8 β-subunits).[201] Each subunit is composed of *(i)* an extracellular domain, *(ii)* a single transmembrane region, and *(iii)* a cytoplasmic region.[202] The combination of α- and β-subunits determines the ligand binding specificity and signalling properties of a given integrin.

Small protein-like chains designed to mimic a peptide and to target receptors with a higher affinity than the natural ligand are so called "peptidomimetics". These compounds offer advantages when compared to natural peptide such as increased physiological half-lives and oral bioavailability.[203] Most integrins recognize their respective ECM proteins through short peptide sequences such as Arg- Gly-Asp (RGD), Glu-Ile-Leu-Asp-Val (EILDV), or Arg-Glu- Asp-Val (REDV). The discovery of the structural basis of the recognition between integrins and their natural ligand have permitted the rational

design of a selective integrin inhibitors without interfering with normal tissues. This strategy called "tumour targeted drug delivery approach" represents a promising strategy because tumor vasculature and tumour cells display a well-differentiated pattern of (over) expression of specific receptors (i.e., receptors required for tumour angiogenesis).[204,205]

A wide variety of integrins are expressed on blood vessels of human tumor biopsy samples but not on vessels in normal tissues. For this reason, most of them are studied in various type of cancer.[206] Specifically, $\alpha_v\beta_3$ (vitronectin receptor) and $\alpha_1\beta_5$ (fibronectin receptor) integrins are studied to be selective toward RGD tripeptide (Arg-Gly-Asp)[207,208] and played a key role in angiogenesis.[209]

The RGD sequence was first discovered in the early 1970s by E. Ruoslahti as a cell attachment site in fibronectin.[210] Nowadays, the RGD sequence is currently the basic module for a variety of molecules designed for the preferential binding to $\alpha_v\beta_3$ integrin and other integrins.[211] The affinity of RGD peptides for their ligands may be modulated by, *e.g.*, steric conformation, the cyclization and linear conformation of the peptides, that could influence receptor affinity, receptor selectivity, and other biological properties.[212]

PEGylated RGD-containing peptides have been successfully functionalized in AuNPs to target specifically cancer cells.[213] The peptide encompass the sequence glycine-cysteine (GC) has

been reported to stabilize gold nanoparticles by cross-linking.[214] Therefore, the design and the synthesis of AuNPs capped by a chimeric peptide named RGD-$(GC)_2$, have recently described.[34] Similar to gold, AgNPs elicited a lot of interest as theranostic platform.[35, 215] Nevertheless AgNPs exhibit several more attractive features in comparison to AuNPs: *i)* a narrower plasmon bandwidth that permits more accurate measurements of the local surface plasmon shift,[216] *ii)* known anti-bacterial activity[217] and low propensity to induce bacterial resistance,[218] and *iii)* availability of green synthetic approaches assisted by biomolecules.[219] The few works reported on silver nanoparticles conjugated to RGD-containing peptides, include the demonstration of programmed cell death in carcinoma cells by nuclear-targeted RGD-conjugated AgNPs [220] and the active conjugation of silver nanoparticles with c-RGD, which rapidly induced endosome formation and minimized nonspecific interactions in comparison to passive PEGylation. [221] Promisingly, poly gamma glutamic acid-capsulated AgNPs conjugated to c-RGD, carried out a sustained controlled release specifically targeting the neovascularization cells and induced apoptosis unaffecting the normal retinal cells, thus demonstrating potential applications as a boon to ocular therapies.[222]

The goal of this work was the comprehensive physicochemical characterization of a hybrid peptide-metal nanoparticle biointerface fabricated by the immobilisation, through thiol chemistry, of a fluorescent cyclic RGD peptide (See Scheme 4) onto AgNPs of 13 nm of diameter.

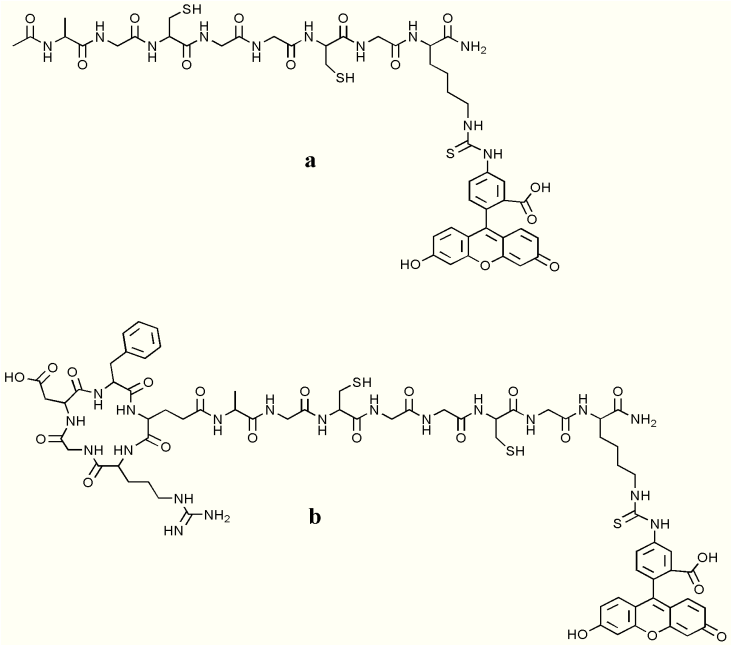

Scheme 4- Structures of the fluorescent peptides FITC-$(GC)_2$ (a) and FITC-RGD$(GC)_2$ (b) used for this paper. Reproduced from Ref. 223 with permission from The Royal Society of Chemistry.

RGD peptide-functionalised AgNPs were investigated by a multi-technique including spectroscopic (UV-visible, FTIR and XPS), spectrometric (ToF-SIMS) and microscopic

(SEM, TEM, AFM) techniques as well as dynamic light scattering and ζ-potential measurements. Results were indeed very promising, with proof-of-work confocal microscopy imaging experiments on neuroblastoma and K562 cell lines, which overexpress respectively the $\alpha_v\beta_3$ and $\alpha_5\beta_1$ integrins, validating the assembled systems as versatile and multifunctional theranostic nanoplatform.

To the best of our knowledge, this is the first work that deals with RGD peptide-silver nanoparticles, with a comprehensive physicochemical study of the hybrid biointerface, in view of its application at with cells and bacteria.[223]

3.7.2 Synthesis of Fluorescent RGD peptide-functionalised silver nanoparticles.

Spherical AgNPs were prepared by sodium borohydride reduction method.[224] The obtained bright yellow dispersion of AgNPs were characterised of 13 nm in diameter, as expected by the plasmon band centred at 389 nm of wavelength. The Figure 27 display the obtained colloidal dispersion.

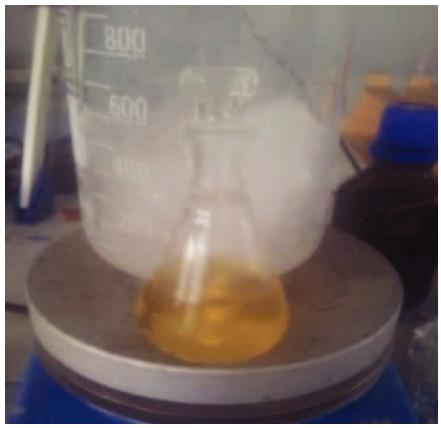

Figure 27. Image of AgNPs dispersion obtained from borohydride reduction method.

3.7.3 Results and discussion

3.7.3.1 Physicochemical characterisation of RGD-functionalised AgNPs.

A spectroscopic study by UV-vis spectroscopy of AgNPs dispersions was carried out to observe the plasmonic shifts, which are a straight marker of size and/or shape modifications of the nanoparticles, upon the addition of peptides (as we demonstrated in this thesis in the previous chapters). To scrutinize whether the introduction of the FITC group in the two peptide sequences $(GC)_2$ and $RGD(GC)_2$ altered the adsorption process onto the metal nanoparticle, both fluorescent and non-fluorescent sequences were investigated. Figure 28 (reported

also in the PAPER IV) show the spectra of the silver nanoparticles in the titration experiments carried out by addition of peptides at increasing concentrations.

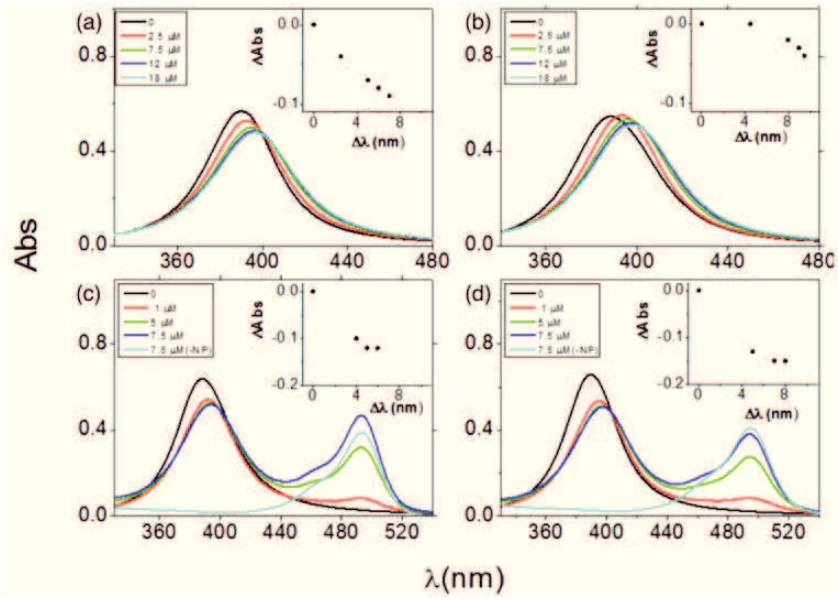

Figure 28. UV-visible spectra of silver colloids ($4.6x10^8$ NP/mL) upon the addition of increasing concentrations of: $(GC)_2$ (a), $RGD(GC)_2$ (b), FITC-$(GC)_2$ (c), FITC-RGD $(GC)_2$ (d). Reproduced from Ref. *223* with permission from The Royal Society of Chemistry.

All spectra showed an overall trend of absorbance decreasing and red-shifts in the plasmonic peak but with different trends for each peptide. An explanation of these different behaviours was inferred due to other type of binding not only the mere chemisorption interaction of the cysteine groups to the metal surface but also other specific contribution, e.g., electrostatic

attraction between the anionic silver nanoparticles and the cationic guanidine side chain of arginine in the RGD sequence.
It is to note that the spectral modification for all the peptide/AgNP assemblies studied was concomitant with the enhancing of brightness of the silver colloidal dispersion, explained in terms of stabilization towards aggregation, due to the nanoparticle coating by the biomolecules. Indeed, the freshly prepared dispersion of bare AgNPs was pale yellow and turned, at the used experimental conditions, to brown-grey after few hours. Conversely, the hybrid peptide/metal nanoparticle system was much more stable, with the yellow colour retained on a time scale of days.
To discriminate between the two possible processes responsible for the observed plasmonic shifts, i.e., particles aggregation and/or actual surface adsorption, the flocculation assay, where an electrolyte solution (NaCl) was added to the colloidal dispersion to disrupt the electrostatic mechanism of stabilisation, was used (see Figure S1 in PAPER IV). The obtained results indicated that the electrolyte neutralized the surface charge of the AgNPs, i.e., the borohydride ions used both to reduce the ionic silver and to stabilize the formed nanoparticles, carrying colloidal dispersion to the aggregation. On the contrary, an almost negligible stabilization in term of absorbance intensity of the plasmonic peak was measured in the peptide-added NPs. On the basis of these data the actual formation of a peptide coating

was inferred. Such an adlayer, adsorbed both chemically and physically, acted as a shell around the metal core thus drastically decreasing the colloidal aggregation. According to the spectra (reported in Figure 1 and S1 PAPER IV), the coverage of AgNPs was calculated to be of about $1.6x10^{10}$ peptide molecules/NP for both $(GC)_2$ and $RGD(GC)_2$ and of about $6.6x10^9$ peptide molecules/NP for both FITC-$(GC)_2$ and FITC-$RGD(GC)_2$, respectively.

In order to remove the loosely bound and/or unbound peptide molecules, centrifugation step occurred and the collected supernatant and pellets (as displayed in the Figure 29) were characterised by UV-Vis spectroscopy (Figure 2 – PAPER IV). The spectra of pellet recovered after the centrifugation of hybrid peptide/silver nanoparticle exhibited a red-shifts in comparison to as prepared dispersion of 14 nm for FITC-$(GC)_2$ and 11 nm for FITC-$RGD(GC)_2$. A contribution to these spectral features could be attributed to a partial aggregation.

Figure 29. Peptide/AgNP dispersion after the centrifugation step. In the red circle is highlighted the collected pellet.

DLS analyses confirmed the increase of the hydrodynamic diameter to ~ 60 nm for the re-suspended pellet of Ag/FITC-$(GC)_2$ and a minor size change to ~ 29 nm for that of Ag/FITC-RGD$(GC)_2$ (Fig 2 c-d, PAPER IV).

The characterization by ζ-potential of the bare and peptide-coated NPs indicated that the anionic bare AgNPs (ZP ~ -20 mV) were neutralised by FITC-$(GC)_2$ peptide immobilization (ZP ~ 0) and exhibited a further increase of the surface negative charge after the functionalisation with FITC-RGD$(GC)_2$ (ZP~ -30 mV). A likely explanation of such a finding, according to the titration experiments discussed above, was given in terms of the preferential orientation of anionic carboxylic groups (in the aspartic acid residue) and of the cationic guanidine group (in arginine) respectively outwards and towards the AgNP surface. It is to note that the charge neutralization of the nanoparticle upon the immobilisation of FITC-$(GC)_2$ was in agreement with the observed aggregation effect, owing to the predominance of dispersive Van der Waals attraction forces compared to the electrostatic repulsions among the AgNPs.

AFM results (Figure 3 - PAPER IV) further confirmed the aggregation effect for AgNPs functionalised with $(GC)_2$ peptide and clearly showed a different morphology of the nanoparticle surface, with the increase of average size after the peptides adsorption. Noteworthy, the phase images displayed a soft shell

(brightest areas) in the RGD peptide-coated compared to the bare nanoparticles.

The characterization by SEM of re-suspended pellets evidenced the presence of dimer aggregates, with average dimensions of about 20 nm with no significant different among all samples.

On the other hand, the TEM micrographs (See Figure 30) displayed the successful peptide coating of the nanoparticles, as evidenced by the appearance of a uniform shell around the core metal (also confirmed by AFM results).

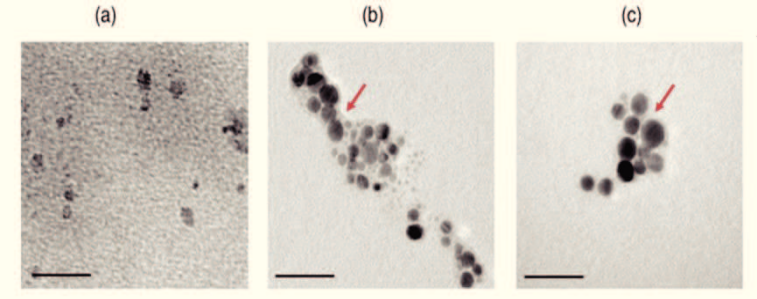

Figure 30. TEM (bottom; scale bar = 50 nm) micrographs of AgNPs from the re-suspended pellet after centrifugation: (a) bare AgNPs; (b) AgNP/FITC$(GC)_2$; (c) AgNP/ FITC-RGD$(GC)_2$. Reproduced from Ref. 223 with permission from The Royal Society of Chemistry.

FT-IR spectra of hybrid AgNP/peptide systems, compared to the reference peptides and bare AgNP samples, showed very similar spectral features (as Figure S2 reported in PAPER IV) but the whole spectra were strongly affected. For our purpose, the most characteristic features were two visible weak peaks at 2450 and 2650 cm^{-1}, due to the free cysteine (-SH), which were not any more visible in the case of AgNP/peptide systems, indicating

that an actual chemisorption process occurred via the thiol moieties.

The quantitative XPS analysis, show in Table 2, confirmed the presence of the peptide in the hybrid peptide/AgNP assemblies by the detection of nitrogen and sulphur signals, not found in the bare AgNPs (Table S1 in PAPER IV). Bare AgNPs showed an actual surface atomic composition consistent with a metal substrate covered with an organic overlayer, according to the carbon and oxygen contents respectively of about 74% and 23%. The peptide molecules are expected to replace the shell of stabilisers ions wrapping the metallic core. Accordingly, the C/O ratio changed from ~ 3.2 in uncoated Ag NPs to ~ 2.6 in FITC-$(GC)_2$/AgNP and ~ 2.3 for FITC-RGD$(GC)_2$/AgNP, respectively.

Table 2. Surface atomic composition of bare and peptide-functionalized AgNPs.

	C 1s (at. %)	N 1s (at. %)	O 1s (at. %)	S 2p (at. %)	Ag 3d (at. %)
Bare AgNP	74.2	-	23.2	-	2.6
FITC-$(GC)_2$/AgNP	65.4	2.2	28.4	0.8	3.2
FITC-RGD$(GC)_2$/AgNP	65.1	2.6	25.3	1	6.1

Representative high resolution XPS spectra (in Figure 5 - PAPER IV), displayed the Ag3d and S2p spectra for the peptides as well as the peptide-AgNP systems, confirmed the results obtained. In fact, the adsorption/chemisorption of peptide on AgNPs surface is inferred by either *(i)* the shift of Ag3d peak to higher binding energies in the peptide-coated AgNPs samples,

due to charge-transfer effects from the metal to the peptide molecules; and *(ii)* in the case of peptide-coated AgNPs samples, the presence of a weak but visible component around 162–163 eV in the S2p signals assigned to sulphur atoms chemisorbed to the silver surface.

ToF-SIMS together with PCA analysis helped to further chemically characterize peptide/silver nanoparticles. Positive ToF-SIMS spectra in Figure 31 (Figure S3 in PAPER IV) of AgNPs, AgNP/FITC-$(GC)_2$ and AgNP/FITC-RGD$(GC)_2$ samples exhibited many peaks, as typical in ToF-SIMS spectra of peptides and proteins, globally similar but with some differences in their relative intensities.

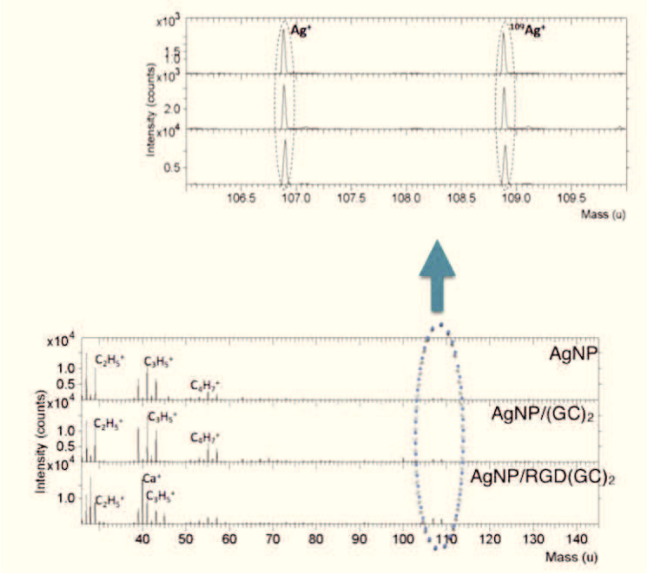

Figure 31. Positive ToF-SIMS spectra of AgNPs, AgNP/FITC-$(GC)_2$ and AgNP/FITC-RGD$(GC)_2$ (from the top to the bottom). Reproduced from Ref. 223 with permission from The Royal Society of Chemistry.

PCA method was used to wisely analyse the ToF-SIMS spectra obtained (see Figure 6 – PAPER IV). PCA analysis was able to discriminate the bare AgNP samples from the peptide/AgNP samples.

The loading plots collected the most significant peaks which explained the PCA model. In particular, we found characteristic ionized fragments associated with the peptides reference samples such as various carbonaceous fragments, including the fragment $C_2H_{10}SN^+$ which is characteristic of the cysteine, and CH_4N^+, which is encountered in most of the amino acids. Moreover, the negative ion ToF-SIMS spectra were relevant to the characterization of Ag-S interfacial bonds, because of sulphur atoms that give rise to intense S^- ions. The score plot obtained from PCA analysis discriminated from AgNP and peptide/AgNP as before (Figure 6b - PAPER IV).

The characteristic ionized fragments listed in the loading plot (Table S2 in PAPER IV) displayed two fragments of CN^- and CNO^-, characteristics respectively of amine and amide moieties were found, and S^- and HS^- ions, characteristic of the cysteine amino acid.

In conclusion, ToF-SIMS analysis could not detect a clear evidence of Ag-S bonds (at the near-surface region). This fact can be explained by differences in the ordered arrangement of the peptide molecules at the nanoparticle surface, with a

thickness of the adlayer higher than the ≈ 1 nm (top-surface region), which is the depth probed by the ToF-SIMS technique. It is noteworthy that the ToF-SIMS technique presents a sensitivity of 1-2 order of magnitude higher than the XPS technique. Indeed, XPS analyses discussed above clearly revealed signals from sulphur moieties in the hybrid AgNP/peptide samples but with a very low intensity of the S2p line related to thiolate bound to silver.

3.7.3.2 Cellular Experiments

Proof-of-work cellular experiments of confocal microscopy imaging were performed to assess the capability of the AgNP/peptide hybrid systems to be internalized by two different cell lines, $\alpha_v\beta_3$ and $\alpha_5\beta_1$ integrins, respectively.

$\alpha_v\beta_3$ integrin is expressed at low levels on mature endothelial cells and epithelial cells, conversely it is highly expressed on the activated endothelial cells of tumor neo-vasculature and other tumor cells, including osteosarcomas, neuroblastomas, glioblastomas, melanomas, lung carcinomas, and breast cancer. [225] Undifferentiated and differentiated neuroblastoma SH-SY5Y cells have been shown to express α_1, α_3, and β_1 integrin subunits, as well as concentrations of α_2, α_4, α_5, α_6, and α_v integrin subunits.[226]

While the $\alpha_v\beta_3$ integrin cooperates with certain growth factors, potentiating their effect on cells, the $\alpha_5\beta_1$ integrin appears to be

a growth-suppressing integrin, and it protects cells from apoptosis when growth factors are absent.[227] It is also to note that several pathogens utilize ECM protein fibronectin as a molecular bridge, indirectly linking the bacterial surface with the $\alpha_5\beta_1$ integrin.[228] An important feature that makes cell adhesion receptors prime targets for bacterial adhesion and invasion is their functional connection to the intracellular cytoskeleton whose rearrangements can lead to cellular invasion. A non-peptide antagonist of integrin $\alpha_5\beta_1$, able to inhibit internalization of streptococci by primary human tonsillar epithelial cells, increased the extent of bacterial killing by antibiotics.[229] A cellular model which overexpress the fibronectin receptor is the K562 cell line, which endogenously express $\alpha_5\beta_1$, with $\alpha_v\beta_3$.[230]

Neuroblastoma cells treated with free peptide and peptide/AgNP systems were reported in the Figure 32 (Figure 7 – PAPER IV).

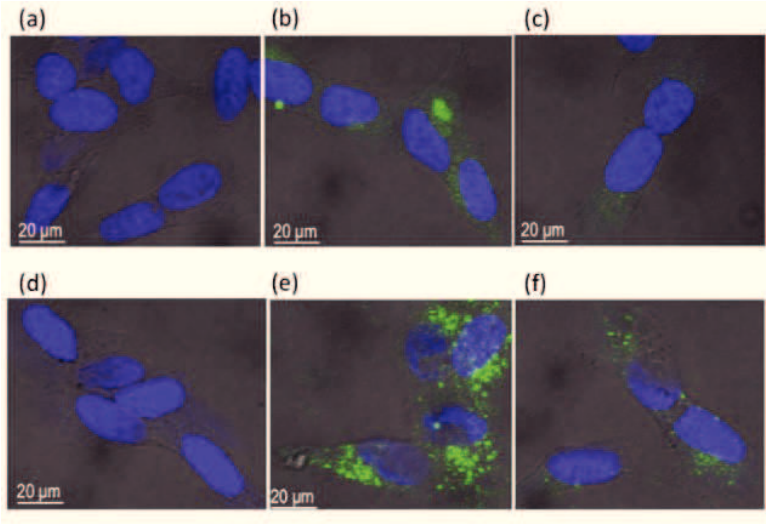

Figure 32. Bright field optical and fluorescence confocal (DAPI, blue; FITC, green) merged micrographs of neuroblastoma SH-SY5Y cells untreated (a) and 2-hours treated with: 5 µM peptides (b: FITC-$(GC)_2$, c: FITC-RGD$(GC)_2$); 3 nM AgNP (d); nanoparticle/peptide systems at 3 nM nanoparticle concentration (e: AgNP/FITC-$(GC)_2$, f: AgNP/FITC-RGD$(GC)_2$). Reproduced from Ref. 223 with permission from The Royal Society of Chemistry.

The comparison with cells treated with the free peptides (Figure 32d) evidences slight differences in the cellular uptake of the two peptides, in terms both of different sub-cellular localization and of intracellular accumulation, *e.g.*, a less spread and more intense green fluorescence for cells treated with FITC-$(GC)_2$ than those treated with FITC-RGD$(GC)_2$. For cells incubated with AgNP/FITC-$(GC)_2$ (Figure 32e) and AgNP/FITC-RGD$(GC)_2$ (Figure 32f), the trend displayed was similar to that found in cells incubated with the free peptides, but an amplified fluorescence was visible. Therefore, the peptides immobilized

onto the AgNPs exhibited a higher internalization, due to the sum of passive transport, related to the nanoparticle carrier, and the active transport, related to the specific peptide sequence. The observed differences, i.e., lower cellular uptake when RGD is in the peptide sequence, can also be related to steric hindrance effects.

As to leukaemia K562 cells, figure 33 (Fig. 8 – PAPER IV) shows that unbound FITC-$(GC)_2$ (Figure 33b) and FITC-RGD$(GC)_2$ (Figure 33c) peptides were not internalized by the cells at the used experimental conditions. However, there was a visible uptake of AgNPs (Figure 33d, dark spots) and also, for the cells treated with the hybrid AgNP/peptide systems, a slight intracellular green fluorescence, which revealed the actual peptide molecules internalization. Such a fluorescence was mostly confined at the cell membrane, visibly lower for cells incubated with AgNP/FITC-$(GC)_2$ (Figure 33e) than those treated with AgNP/FITC-RGD$(GC)_2$ (Figure 33f).

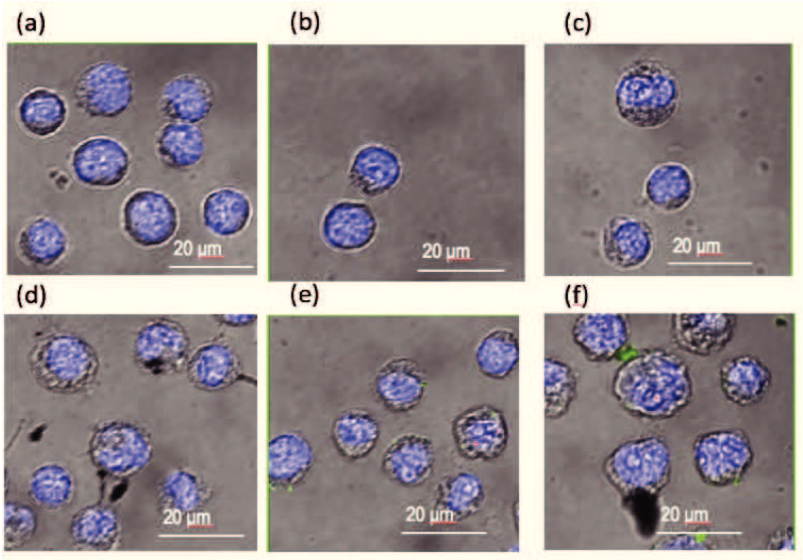

Figure 33. Bright field optical and fluorescence confocal (DAPI, blue; FITC, green) merged micrographs of leukaemia K562 cells untreated (a) and 2-hours treated with: 5 µM peptides (b: FITC-$(GC)_2$, c: FITC-RGD$(GC)_2$); 3 nM AgNP (d); nanoparticle/peptide systems at 3 nM nanoparticle concentration (e: AgNP/FITC-$(GC)_2$, f: AgNP/FITC-RGD$(GC)_2$). Reproduced from Ref. 223 with permission from The Royal Society of Chemistry.

Therefore, the AgNP/peptide platform was effective to achieve a cellular uptake of the peptides that could not be reached, at the same experimental conditions, with the free peptides. Moreover, also in this case, some peptide-specific differences in the cellular uptake occurred, therefore suggesting that the peptide immobilized at the surface of the silver nanoparticle still maintained its activity towards the specific integrin receptor.

3.7.4 Conclusions

The obtained results clearly demonstrated that the hybrid peptide/AgNPs assemblies keep some specific activities in the uptake by neuroblastoma SH-SY5Y and leukemia K562 cells, likely related to the specific peptide sequence. Moreover, the different cellular uptake showed by the two cell lines pointed to certain cell selectivity towards the uptake of the peptide-coated nanoparticles. It is to note that the effects of the binding to $\alpha_5\beta_1$ and $\alpha_v\beta_3$ depend on signaling specific pathways for these integrins. Moreover, integrins require activation from the inside of the cell to be able to bind their ligand outside the cell. High $\alpha_5\beta_1$ expression and abundant matrix formation also suppress tumorigenicity *in vivo*, whereas perturbing the function of $\alpha_5\beta_1$ with peptides that block its ligand binding suppresses experimental metastasis.[230] Effecting these changes in tumor cells by a theranostic platform such as the AgNP/RGD-peptide assembly may provide new potentially highly effective cancer therapies.

3.7.5 Future Perspectives

Further experiments, by staining cellular organelles such as lysosomes, mitochondria and Golgi with the respective dyes, are planned to map precisely by co-localization analysis the fate of the peptide-conjugated AgNP nanoplatform inside the cells.

4 Graphene oxide and its derivatives at the biointerface with curcumin-loaded lipid bilayers, albumin and doxorubicin.

4.1 Graphene and Graphene oxide nanomaterials in theranostics

Carbon nanomaterials, such as graphene (G) and graphene oxide (GO), have been at the focus of recent investigations for potential applications in various areas ranging from nanoelectronics, composite materials, energy technology, sensors, and catalysis, which have been summarized by several review articles.[231,232]

G is a material composed by sp^2-bonded carbon atoms. As a basic building block of other carbon allotropes, G can be wrapped to generate 0D fullerenes, rolled up to form 1D carbon nanotubes, and stacked to produce 3D graphite.[233] Particularly, the intensive research on the bio-applications of G and its derivatives is due to many fascinating properties, such as high specific surface area (2630 m^2/g), exceptional electronic conductivity (mobility of charge carriers, 200,000 $cm^2\ V^{-1}\ s^{-1}$), thermal conductivity (~5000 W/m/K) and mechanical strength (Young's modulus, ~1100 GPa).[231]

After the observed micromechanical exfoliation of G by Novoselov et al. in 2004,[234] various methods for the design of new synthetic routes have been developed, such as chemical

exfoliation of graphite,[235] chemical vapor deposition (CVD) growth[236] and chemical synthesis.[237]

Moreover, beyond the applications aforementioned, the biomedical application of G and its derivates is a relative new area with significant potential.[238] Even though G surfaces have successfully found many applications,[239] its poor solubility and difficult processability in water make it a less than ideal material to work in biomedical fields. Instead GO sheets, which exhibits hydroxyl and epoxy groups on its basal planes and carbonyl groups at the edges, not only readily swell and disperse in aqueous media, but also provide an optimal nanoplatform for the interaction with biomolecules.[240]

In the last years, carbon-based nanomaterials have found many applications as potential drug delivery systems. The delocalized π-electrons on graphene plane enable the binding of various drugs *via* non-covalent interactions; also, the conjugation through specific chemical bounds with selective drugs can be realized. Therefore, graphene and graphene oxide for drug and gene delivery have been extensively discussed in many reviews,[241,242] for *in vivo* promising application.

One of the possible therapeutic applications of graphene family nanomaterials (GNFs) include photo-therapies, mainly photothermal therapy (PTT) and photodynamic therapy (PDT).[243,244] These strategies are able to destruct cancer cells

upon specific light irradiation specifically targeting cancer without significant damage to normal organs in dark.

The GO-based nanomaterials have been extensively explored to develop sensitive biosensors.[245, 246] Exploiting the efficient fluorescent quenching ability of graphene, novel fluorescent resonance energy transfer (FRET) devices have been developed.[247] The unique electronic properties of G were also applied to directly detect bio-signals from living cells based on Field Effect Transistor (FET) devices.[248] Moreover, the hybrid nanocomposites composed by graphene and noble metals have been widely utilized as Raman signal enhancing substrate in various SERS-based biosensors.[249] These systems showed synergistically enhanced sensing performance compared to the typical systems with one kind of metal.

Finally, a matrix for detection of molecules graphene-based nanoplatform for matrix-assisted laser desorption/ionization time-of-flight mass spectrometry (MALDI-TOF MS) has been reported.[250]

4.2 Synthetic strategies for the synthesis of GO and its derivatives.

GO sheets have a history that extends back many decades to some of the earliest studies involving the chemistry of graphite. The first well-known example came in 1859 when British chemist B. C. Brodie performed a reaction adding potassium

chlorate ($KClO_3$) to a slurry of graphite in fuming nitric acid (HNO_3).[251] Brodie determined that the resulting material was composed of carbon, hydrogen, and oxygen, dispersible in pure or basic water, but not in acidic media, which prompted him to term the material ‘‘graphic acid’’.

L. Staudenmaier improved Brodie’s preparation by adding the chlorate in multiple aliquots over the course of the reaction and concentrated sulfuric acid to increase the acidity of the mixture. This slight change in the procedure resulted in an overall extent of oxidation.[252]

After Staudenmaier, Hummers and Offeman developed an alternate oxidation method by reacting graphite with a mixture of potassium permanganate ($KMnO_4$) and concentrated sulfuric acid (H_2SO_4), again, achieving similar levels of oxidation (Figure 34).[253] After Hummers and Offeman synthesis, many other versions have been proposed, but in reality, little changing have been applied.[254] Some differences can be obtained changing the type of oxidants used, the graphite source and reaction conditions. Also, other discriminating characteristics of GO are the number of layers, surface chemistry, purity, lateral dimensions, defect density and composition.

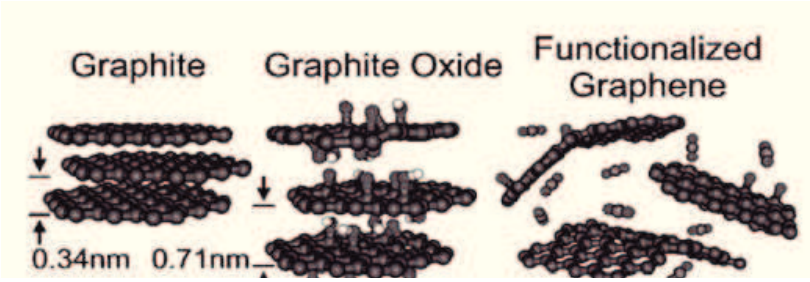

Figure 34. Scheme of graphite oxidation using Staudenmaier method with subsequent thermal exfoliation. Adapted from ref. 255.

GO produced by rough oxidation of crystalline graphite and followed by dispersion in aqueous medium through sonication or other processes is obtained as multilayers. In fact, the basal plane of GO contains free surface π-electrons from unmodified areas of G, which are hydrophobic and capable of π–π interactions for drug loading and non-covalent functionalization. [256] However, repeated treatment, centrifugation and harsh environment lead to production of monolayer oxidized graphene. The presence of functional groups creates high defect density due to their disrupted sp^2-bonding networks in GO thereby reducing its mechanical, electrical and thermal properties.[257]

Reduced graphene oxide (rGO) belongs to the GFNs. rGO is mainly produced to recover the electrical, thermal, and mechanical properties of G, restoring the π-network and reducing the oxygen content, surface charge, and hydrophilicity. [258] rGO can be obtained following different reaction processes ranging from chemical to physical methods.

Scalability is a fundamental requirement of a useful synthetic protocol if graphene wants to be broadly utilized.

Among chemical reduction reactions, the most common is certainly the reaction with hydrazine monohydrate.[259] One of the disadvantages of using hydrazine, or in general chemical methods of reduction, is the introduction of heteroatom impurities. While effective at removing oxygen functionality, nitrogen tends to remain covalently bound to the surface of GO, likely in the form of hydrazones, amines, aziridines or other similar structures.[260] Residual C–N groups have a profound effect on the electronic structure of the resulting graphene, functioning as n-type dopants.[261]

Other reducing agents are lithium aluminium hydride (LAH), but the major challenge is the dispersion of the reagent in water;[262] sodium borohydride ($NaBH_4$), more effective than hydrazine as a reductant of GO;[260] hydroquinone,[263] gaseous hydrogen (after thermal expansion),[264] and strongly alkaline media.[265] Sulfuric acid or other strong acids can also be used to facilitate dehydration of the graphene surface.[266] "Green" reducing agents can be utilized as vitamin C or ascorbic acid,[267] bovine serum albumin (BSA)[268] and bacterial respiration.[269]

Electrochemical reduction is considered an alternative method to produce rGO.[270] In principle, this could avoid the use of dangerous reductants (*e.g.* hydrazine) and disposing of the by-products. After depositing thin films of GO on a variety of

substrates (glass, plastic, ITO, etc.), electrodes were placed at opposite ends of the film and linear sweep voltammetry was run in a sodium phosphate buffer.

Even if chemical reduction is the most common methods to produce rGO, physical approaches can also generate exfoliated and reduced GO. Thermal exfoliation and reduction of GO happens by directly heating.[271] The by-products caused by heating leaves behind vacancies and topological defects throughout the plane of the reduced GO platelets, which inevitably affect the electronic (and probably the mechanical) properties of the products by decreasing the ballistic transport path length and introducing scattering sites.[272]

Other physical reduction methods can be mentioned are photothermal reduction[273] and sonolysis.[274]

Recently, "green" approaches to produce rGO sheets have been developed as microwave-assisted reduction [275] and UV-irradiation.[276] Also, a laser-assisted synthesis of rGO at the water-air interface was demonstrated by Compagnini et al.[277]

4.3 Covalent or non-covalent functionalization strategies of graphene.

Functionalization of GFNs with small molecules, polymers, nanoparticles is a strategy widely used to enhance or alter the properties required for specific application. It is well known that the surface chemistry of nanomaterials is the key to improve the

biocompatibility of nanomaterials and control their behaviour in biological systems. Depending on different application purposes, various surface coating strategies of GO and rGO, including covalent and non-covalent approaches, have been designed to engineer functionalized graphene-based materials for use in biological application.

Theoretically, owing to the rich chemistry of hydroxyl, carboxyl, and epoxy groups, GO has been used very often as the starting materials for the formation of graphene derivatives through the covalent attachment of organic groups on its surface.[278]

GO can react with polymeric chains that have reactive groups such as hydroxyls and amines. The conjugation with polymers confers to GO new reinforcement characteristics as dispersibility, mechanical strengthening, and several morphological characteristics. For example, poly(ethylene glycol) (PEG) can be grafted onto GO nanoplatelets for different reasons: *i)* to enhance their dispersible in water (also, in several biological solutions such as serum or cell medium) and their biocompatibility; *ii)* to reduce their non-specific binding to biological molecules and cells and *iii)* to improve their *in vivo* pharmacokinetics for better tumor targeting. This important characteristic makes PEGylated GO an important candidate for the delivery of hydrophobic drugs in biological systems.[279] Besides, other polymers have anchored to GO. Polyacrylic acid

(PAA) and poly(N-isopropylacrylamide) (PNIPAM) have used to modify graphene based nanocomposites to be environmental pH-responsive and thermal-responsive, respectively.[280]

The residual oxygen-containing groups give to the rGO a weaker chemical reactivity as regards organic groups that can be grafted onto the graphene surface through oxygen linkers. The first strategy to chemical functionalize RGO using residual oxygen groups has been presented by Hsiao et al.[281] Moreover, the solubility of rGO in aqueous solutions usually becomes worse because of the loss of oxygen-containing hydrophilic groups. Some examples of the possible covalent polymer functionalizations on rGO can be the bounding with poly(L-lysine) (PLL) to make dispersible devices in biological solution and useful for theranostic applications,[282] as well as, polystyrene (PS) chains to improve the mechanical properties of rGO.[283]

Apart from conjugated polymers, simple organic chromophores such as porphyrins, phthalocyanines, and azobenzene with very interesting optoelectronic properties have been covalently attached on graphene nanoplatelets.[284]

Besides covalent chemical reactions, graphene can also be non-covalently functionalized by polymers or biomolecules *via* hydrophobic interactions, π–π stacking, or electrostatic binding. *Via* non-covalent interactions, G and GO can be stabilized by a surfactant or amphiphilic polymers to improve their stability in aqueous solutions. However, for biomedical use, biocompatible

polymer coatings are usually preferred. In fact, non-covalent coating of PEG grafting was developed using rGO with excellent physiological stability and ultra-long blood circulation half-life useful for photothermal cancer treatment.[285]

The non-covalent functionalization method is essentially based on hydrophobic interactions between the graphene surface and amphiphilic polymers. Since GO sheets are highly negatively charged, a positively charged polyelectrolyte can bind GO *via* electrostatic interactions. For instance, this approach can be exploited for gene transfections [286] and drug delivery. For example, in this last case, doxorubicin (DOX) was loaded on GO using positively charged folate conjugated chitosan.[287]

Furthermore, natural reducing agents as curcumin was also used to both reduce and functionalize GO through π-π attachments onto its surface.[288]

4.3.1 The hybrid nanobiointerface between nitrogen-doped graphene oxide and lipid membranes: a theoretical and experimental study.

The functionalization of graphene using organic moieties constitutes an affordable way to modulate its physical and chemical properties, especially at the interface with biomolecules. The large surface area and the combination of hydrophobic character and π−π stacking interaction with drug molecules are some reasons for the interest of graphene application in theranostics.[289, 290]

On the other hand, GO with a number of hydroxyl, epoxy and carboxyl groups is hydrophilic, with an excellent solubility in water. *In particular, the introduction of amino groups at graphene surface is one of the most attractive approaches to control the charge-potential landscape at solid-liquid interfaces, for engineered novel devices for applications in catalysis and energy conversion as well as sensing and biodevices*.[291, 292] For example, a theoretical study about the thermal stability and thermodynamics of amino- and ethylamino-graphene found that more amino groups stabilize the functionalized graphene thus favouring further amination, whereas a small concentration of amino groups is unstable in many cases.[293]

Because of the gained importance in the application of GO at the biointerfaces, the study of the engineered nanomaterial interactions with the biological membranes[294,295] have increased

to scrutinize the possible mechanisms of the cytotoxicity of GO.[296] In fact, lipid vesicles as small unilamellar phospholipid vesicles (SUVs), spontaneously adsorb and subsequently rupture under appropriate conditions and on a hydrophilic surface. [297] This spontaneous phenomenon to form planar membrane is exploited to the formation of so called supported lipid bilayers (SLBs) on solid substrates.[298] SLBs (Figure 35) are bilayer membranes existing at the solid liquid interfaces which are used to mimic the fundamental physicochemical properties of lipid bilayers and also as cell membrane model systems *in vitro*.[299]

Figure 35. Representative supported lipid bilayer at the solid liquid interfaces.

Different parameters are involved during the formation and control of the properties of SLBs. Among them, the fabrication techniques, the physical/chemical properties of the substrate surfaces can influence the formation, the stability and the behaviour of SLBs.[300] A hydrophilic surfaces is a prerequisite for the spontaneous SLB formation from

adsorption/rupture/fusion processes of lipid vesicles. Thus, mica, glass, silica, quartz and TiO_2 are generally used.[301] For example, Satriano et al. demonstrates a SiO_2 coating made from poly(hydroxymethylsiloxane) (PHMS) that reproducibly allowed for SLB formation from vesicles. The surface of PHMS films was converted, via plasma oxidation, into a SiO_2- like, stable, very hydrophilic and smooth overlayer.[302]

Other parameters for the interaction between lipid bilayer membranes and solid substrates include the lipid composition,[303] the size of vesicles and temperature.[304]

The most common *in situ* label-free methods for the characterization of SLB interfaces are: quartz crystal microbalance with dissipation monitoring (QCM-D),[305] due to its unique ability to distinguish between intact vesicle adsorption and SLB formation on the surface; surface plasmon resonance (SPR),[306] ellipsometry,[307] and AFM.[308]

The fluidity of cell membranes is another important factor for biological reactions, many of which include the lateral molecular diffusion as a fundamental process for the lateral molecular transportation and formation and/or dissolution of two-dimensional domains.[309] The fluidity of SLBs is evaluated by fluorescence recovery after photobleaching (FRAP), [310] fluorescence correlation spectroscopy (FCS) [311] and single molecule tracking (SMT). [312] Generally, diffusion in a macroscopic area on the order of several micrometers to 100 μm

is evaluated with FRAP, while it is possible to detect the diffusion at a narrower region with FCS and SMT in principle. Specifically, in the FRAP technique, a small spot on the fluorescent surface is photobleached by a brief exposure to an intense focused laser beam, and the subsequent recovery of the fluorescence is monitored by the same, but attenuated, laser beam. Recovery occurs by replenishment of intact fluorophore in the bleached spot by lateral transport from the surrounding surface. The lateral molecular diffusion in SLBs is always under the effect from substrates. It is reported that the diffusion coefficient (*D*) of lipids in SLB is calculated by using the Axelrod's algorithm[313] $D_{coeff} = 0.88w^2/4\tau_{1/2}$, where *w* is the radius of the bleached area and $\tau_{1/2}$ describes time for 50% recovery.

Finally, various kinds and sizes of domains and clusters exist in cell membranes and play key roles in signal transportation and molecular recognition through and on cell membranes. A representative example is the concept of “raft domains”, but the relation between the properties of such domains and biological functions are still to be elucidated. SLBs will be also valuable as artificial reaction fields to study how two-dimensional assemblies of lipids and proteins affect biological functions. For instance, the adhesion of lipid vesicles having controlled chemical and physical structure to polymer supported human serum albumin (HSA) thin layers was investigated, at varying

parameters such as the chemical composition of lipid bilayer, suspending solution and protein film.[314]

Also GO induces the rupture of pre-adsorbed liposomes and the formation of a nanocomposite, bio-nonbio multilayer structure, consisting of alternating graphene oxide monolayers and lipid membranes, with an important role played by electrostatic interactions between graphene oxide and lipid headgroups.[315] Recently, Wu et al., provided evidence that overcoming the electrostatic repulsion of phosphate group, its hydrogen bonding attraction as well as the electrostatic and hydrophobic interaction of choline group are the driving forces for the effective adsorption of GO on lipid membrane.[316]

However, a comprehensive understanding about the nature of the interaction between GO and lipid membrane still remains challenging. **As this regard, we address a comparative investigation of GO and nitrogen-doped GO (N-GO) at the hybrid nano-biointerface with lipid bilayers at the two pH of 7.4 and ~6. This study provides the first investigation, both theoretical and experimental, of the interaction between N-GO and lipid membranes. The effect of the graphene-lipid biointerface for drug delivery applications was scrutinized by using the case study of curcumin (Curc).**

4.3.2 Curcumin

Curcumin (Curc), bis(4-hydroxy-3-methoxyphenyl)-1,6-diene-3,5-dione, is a low molecular weight polyphenol yellow compound derived from the rhizome of the plant Curcuma longa. It has been widely used in traditional Ayurvedic and Chinese medicine since the second millennium BC.[317] Curc has a wide range of pharmacological applications such as anti-inflammation, antihuman immunodeficiency virus, anti-microbial, anti-oxidant, anti-parasitic, anti-mutagenic and anti-cancer with low or no intrinsic toxicity (Figure 36). [318]

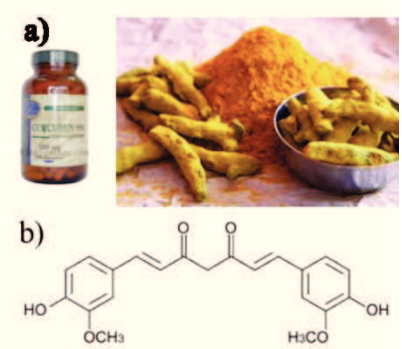

Figure 36. Representative images of Curc powders for pharmacological application (a); chemical structure of Curc (b).

Despite all these extraordinary anti-cancer properties, curcumin suffers from low solubility in aqueous solution (≈20 μg/mL) and undergoes rapid degradation at physiological pH, which results in low systemic bioavailability, poor pharmacokinetics, and greatly hampers its in vivo efficacy.[319]

To improve Curc application as an anti-cancer agent, it is necessary to improve its stability and bioavailability. At this regard, numerous formulations based on Curc encapsulation in polymer nanoparticles or nanogels, [320] liposomes, [321] and conjugates [322] have been generated. These systems not only improve drug solubility and stability but also provide drugs to the cancer cells in their active form.

Among the natural agents, Curc is known as one of the effective natural antioxidants. There are also some recent reports concerning application of curcumin in synthesis and functionalization of nanoparticles having antioxidant properties. [323] Moreover, it was found that some natural compound having aromatic structures can not only reduce GO (rGO) sheets, but also functionalize the rGO ones through π–π attachment of the reductant molecules onto the rGO surface. Newly, CURC was also utilized for simultaneous reduction of chemically exfoliated GO sheets and functionalization of the rGO ones through π–π attachment. Also, the potential concentration-dependent cytotoxicity of the curcumin-functionalized rGO sheets was investigated against two human breast cancer cell lines and a normal mouse cell line using viability assay.[324]

In this study, we demonstrate that a controlled modification of the GO surfaces by introducing amino-containing groups

at different oxidation level, can modulate the surface termination and, in turn, the release of Curc at the graphene surfaces from lipid vesicles loaded with the model drug.[325]

4.3.3 GO fabrication and N-GO preparation.

Graphene sheets were deposited on glass or silica by mechanical exfoliation of graphite and successively exposed to UV-ozone (UVO) irradiation for 1 h.[326] Alternatively, GO was synthesized from graphite powder using a modified Hummer's method.[327] Graphene oxide sheets were thus obtained.

According to Ren procedure,[328] the amino-derivatisation of GO samples was studied by using two different approaches of wet chemistry reduction (Figure 37).

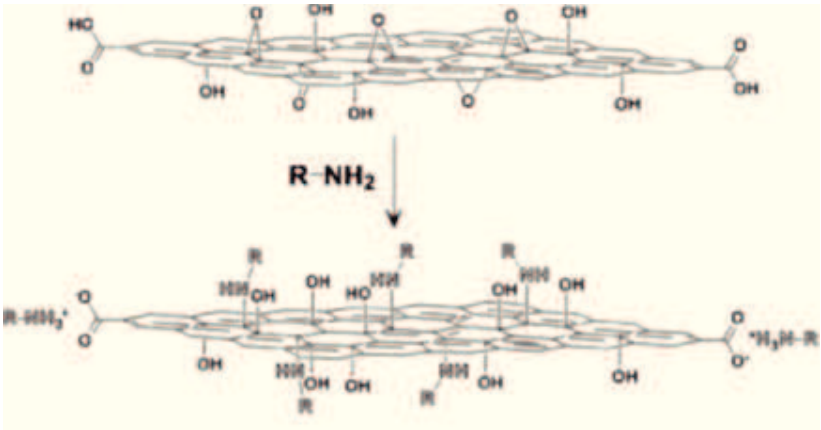

Figure 37. GO and amino-GO after the treatment with amino-compounds. Adapted from ref. 329.

4.3.4 Preparation of the Lipid Vesicles.

Zwitterionic small unilamellar vesicles (SUVs) were prepared from a chloroform solution of 1-palmitoyl-2-oleoyl-sn-glycero-3-phosphocholine (POPC) added with rhodamine-DHPE (1,2-dihexadecanoyl-sn-glycero-3-phosphoethanolamine) to obtain dye-labelled POPC-Rhod. To prepare the curcumin loaded vesicles (POPC-Rhod-Curc), Curc was dissolved into the lipid solution in chloroform. The solvent was evaporated under Ar flow, to obtain lipid films adsorbed on the wall of a round-bottomed

flask. The film afterward was emulsified in phosphate buffer saline solution (PBS) at room temperature, vortexed, and extruded 13 times through a 100 nm polycarbonate membrane, followed by another 13 times through a 30 nm membrane. In order to remove the unloaded curcumin, the vesicles were centrifuged 15 min at 8,000 r.p.m. and the supernatant recovered and stored under Ar at 4 °C. Figure 38 display the photographs of the obtained lipid vesicle samples.

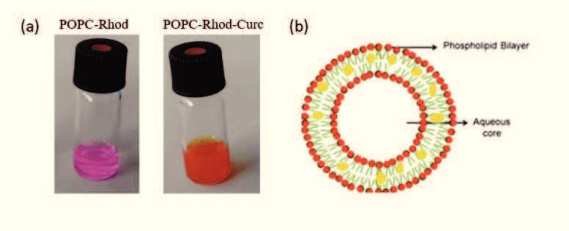

Figure 38. (a) Photographs of POPC-Rhod (on the left) and POPC-Rhod-Curc (on the right); (b) representative lipid vesicles loaded with curcumin molecules.

4.3.5 Results and discussion

In the first approach, N-GO in dispersion was produced by adding the reductant agents (N_2H_4, DDA or DDA/N_2H_4 mixtures) to the aqueous dispersion of the graphene oxide. In the second approach, N-GO solid was obtained by deposition, through exfoliation of graphite, of numerous sheets of graphene on a silica substrate, then oxidising graphene to graphene oxide by UVO treatment and eventually dropping the reducing solutions at the top surface of the GO solid samples. Representative images for the obtained graphene derivatives were shown in the Figure 39.

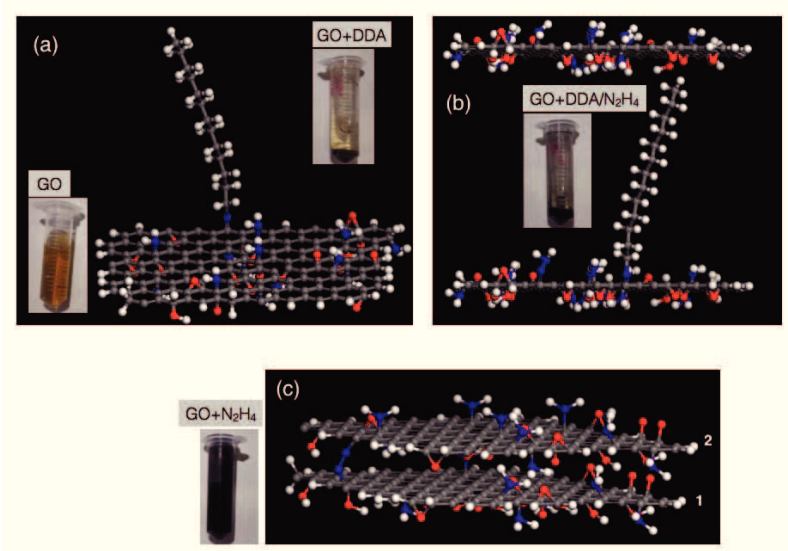

Figure 39. A schematic view (and photographs of the prepared samples) for the three different N-doped GO obtained by GO treatment with: (a) DDA, (b) N_2H_4, (c) DDA/N_2H_4. Reproduced from Ref. 325 with permission from AIMS Materials Science.

The reduction of GO by dodecylamine is expected to introduce amino functionalities at the near interface with the graphene sheet, thus resulting in N-GO samples with an outward orientation of alkyl groups, e.g., C(graphene sheet) = NH–$(CH_2)_{11}CH_3$. In the case of hydrazine, the bifunctional character of the molecule is likely to prompt the formation of N-GO aggregates, with diazo moieties (e.g., C(graphene sheet 1) = N–N = C(graphene sheet 2) bridging between two or more graphene sheets. When both DDA and N_2H_4 are used, the dodecylamine molecules may play a spacer role between the graphene sheets, and therefore the presence of amino-terminated graphene sheets can be figured out, e.g., C(graphene sheet) = N–NH_2 (Figure 39). It must be noted that while hydrazine is a known reductant of GO, the interaction between GO and DDA has three possibilities: hydrogen bonding, electrostatic attraction between carboxylic group and protonated amine and, most predominantly, the nucleophilic substitution between epoxy and amine, which result into the grafting of the long hydrocarbon chain of the octadecylamine onto GO sheets.[330,331]

The GO and GO-N samples were characterized by Raman, XPS and UV-vis spectroscopies. The Raman spectra of the solid-state samples used in the second approach are shown in Figures 40.

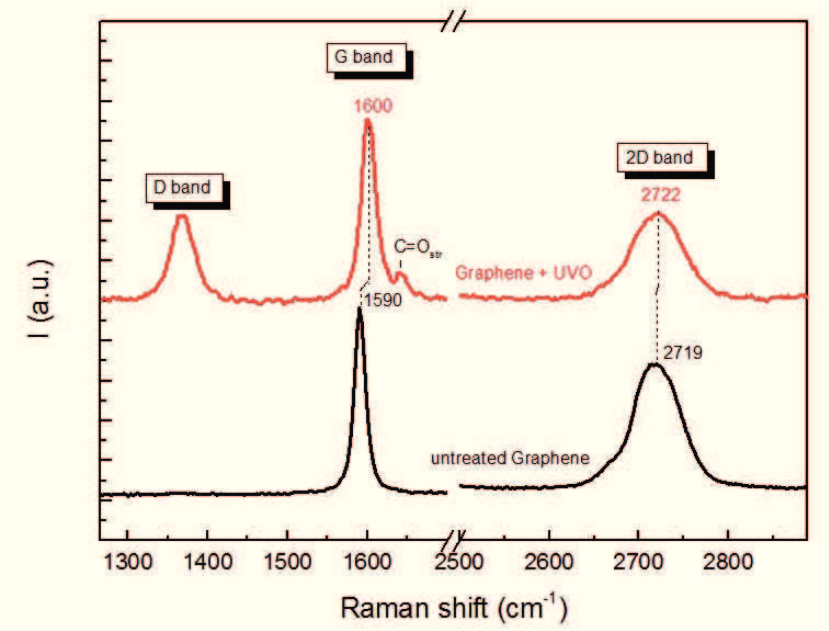

Figure 40. Raman spectra of a few layer-thick graphene sample before (black line) and after (red line) oxidation by UVO (treatment time = 1 h). Reproduced from Ref. 325 with permission from AIMS Materials Science.

The spectra of a few-layers thick (~5 layers) graphene (FLG) sample, before and after exposure to UVO, demonstrates the effectiveness of 1h treatment for the conversion of the original graphitic structure to an oxidised form (Figure 40). Indeed, the spectrum of untreated graphene shows a unique peak, at about 1590 cm^{-1}, characteristic of sp^2 carbon (G band), whereas for the UVO-treated graphene two new peaks are visible, at ~1350 cm^{-1}, typical of sp^3 carbon (D band), and at ~1620 cm^{-1}, due to carbonyl stretches.[332] The shape and the position of the 2D band that usually can be used to determine the stacking order in a

FLG, can also be related to the possible stress and defects induced by the UVO treatment. There is no significant change in spectral shape of the 2D band but only a negligible decrease in the peak intensity. Furthermore, the in-depth effect of the UVO-induced oxidation of the graphene sheets for samples at different thicknesses were analysed by Raman spectroscopy. The Raman spectra (See supplementary information of the paper VI) evidence the signals of sp^2-bonded carbon layers at about 1590 cm^{-1} and 2700 cm^{-1}, assigned respectively to the doubly degenerate zone centre E_{2g} mode (G band) and to the second order (2D band) of zone-boundary phonons. According to their relative intensities, the shape and the frequency position, such peaks are assigned to double layer graphene (DLG), few-layer graphene (FLG), and multi-layer graphene (MLG). The comparison with the spectra recorded for UVO-treated graphene samples indicates that the conversion to GO actually involves only the top surface of the graphene sheets. This finding validates the used approach as an efficient methodology to fabricate a thin overlayer of graphene oxide onto a graphene substrate.

The Raman spectra of N-GO samples, obtained with the different approaches were displayed in Figure 41.

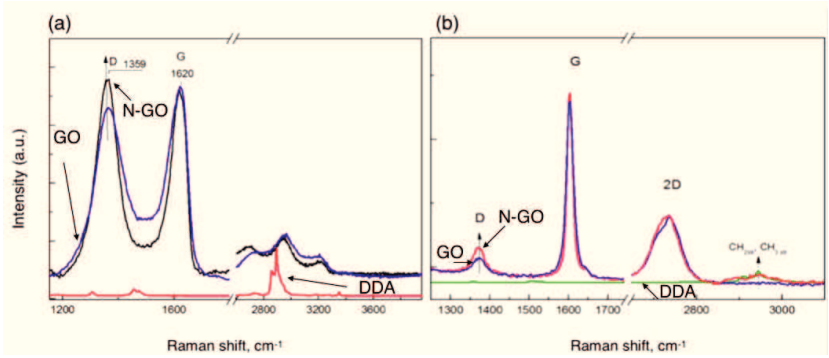

Figure 41. Raman spectra of GO (aqueous dispersion) (a) and G/UV-ozone treated (b) after functionalisation with DDA. Reproduced from Ref. 325 with permission from AIMS Materials Science.

A visible enhancement of the D peak is visible in the Figure 41a. These findings point to the increase of graphitic-defective sp^3 domains likely due to the grafting of the amine molecules at the graphene surface. The hydrocarbon CH_2 and CH_3 stretches in the 2800–3200 cm^{-1} region, clearly visible in the DDA spectrum, are instead absent in the N-GO spectrum, probably because they are hidden by the second order graphene signals. For N-GO solid samples (Figure 41b) both the increase of D band and the appearance of CH_2 and CH_3 stretching are observed. Raman spectra of the N-GO samples functionalised by N_2H_4 or DDA/N_2H_4 did not exhibit detectable Raman signals owing to fluorescence interference.

The optical characterisation of GO and of N-GO samples in dispersion prepared by reduction with DDA, N_2H_4 and DDA/N_2H_4 shows, for all the N-GO samples, a bathochromic

shift of the GO characteristic spectral features, which are the peak around 230 nm (π-π* plasmon peak)[333] and the shoulder around 300 nm. Similar trends are found both in water (pH: ~6, Figure 42a) and in PBS buffer (pH: ~7.4, Figure 42b). In particular, the peak at 230 nm exhibits a red shift of about 29 nm in GO+N_2H_4 sample, both in water and in buffer. In GO + DDA sample such a peak disappears in water and broadens in PBS. As to the sample GO+DDA/N2H4, a sum effect of contributions of the GO+DDA and GO+N_2H_4 spectra is observed.

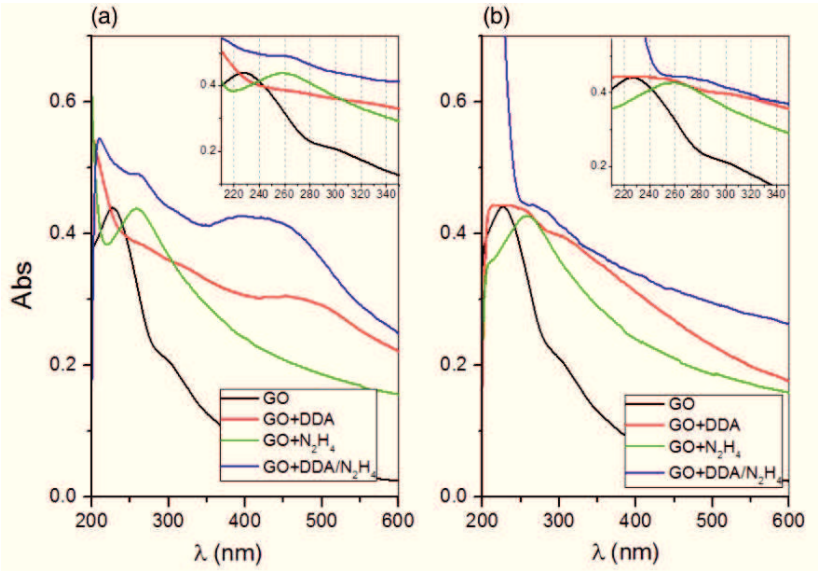

Figure 42. UV-Vis spectra in ultrapure water (a) or PBS buffer (b) of GO and N-GO samples obtained by treatment with dodecylamine (GO + DDA), hydrazine (GO + N_2H_4) or the mixture (GO + DDA/N_2H_4). Reproduced from Reproduced from Ref. 325 with permission from AIMS Materials Science.

In the π-π* plasmon peak two kinds of conjugative effect coexist, related to nanometer-scale sp^2 clusters and linking chromophore units such as C=C, C=O and C–O bonds.[364] The

UV-Vis spectral changes in N-GO samples in comparison to GO can be related to the introduction of defects in the sp^2 domains by the formation of new C=N bonds, as well as conjugative effect of chromophore aggregation, which influences the π-π* plasmon peak.

The deconvolution obtained from XPS analysis of C1s and N1s peaks (Figure 43) confirm the considerations inferred from the UV-Vis spectra. Indeed, the relative intensity ratio C1/C2/C3 of the different components of carbon peak in GO, respectively at 284.6 eV (C1, C–C and C–H bonds), 286.7 ± 0.2 eV (C2, C–O bonds) and 288.7 ± 0.2 eV (C3, C(=O)O bonds) of binding energy (BE), change differently in the different GO-N samples, which all exhibit a new C=N component (C4, at 285.7 ± 0.2 eV).[334] Compared to the spectrum of GO, the decrease of peak intensity of C2 component in GO+DDA (Figure 43) and GO+N_2H_4 (Figure 43c) indicates that the grafting mainly occurred through the reaction of the epoxide functional group in GO. In the case of GO+DDA, a component related to the carbonyl groups is found (C5, at 288.2 ± 0.2 eV) instead of the carboxylic C3 component.

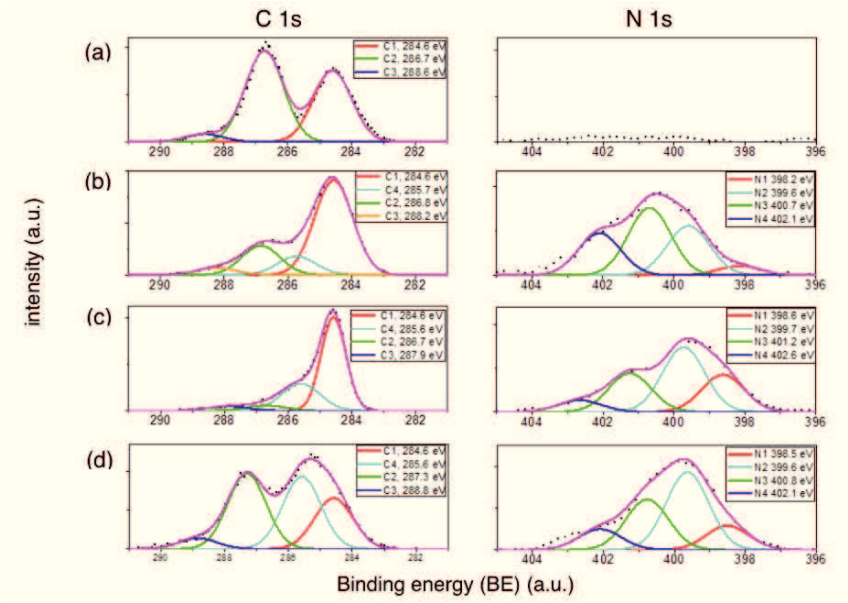

Figure 43. XPS spectra of C1s (left panels) and N1s (right panels) regions for: (a) GO; (b) GO + DDA, (c) GO + N_2H_4, (d) GO + DDA/N_2H_4. Reproduced from Ref. 325 with permission from AIMS Materials Science.

As to the nitrogen XPS spectra of the different nitrogen-doped GO surfaces, the broad N1s peak could be deconvoluted into four chemically shifted components: at 398.8 ± 0.2 eV (N1), 399.6 ± 0.2 eV (N2), 400.7 ± 0.2 eV (N3) and 402.1 ± 0.2 eV (N4) of binding energy, respectively.

These peaks are assigned respectively to: hydrogen-based interactions between the amino groups and the oxygen functionalities (N1), C–N linkages as a result of covalent interactions of amino groups with GO (N2), charge-induced interactions between the protonated amines and weakly acidic sites of GO (N3), and $C–N^+$ (from quaternary nitrogen) or NH_4^+

(N4).[335] The N2 component is therefore an indicator of the effective grafting of the *n*-alkylamines on the basal plane of GO through covalent interactions, whereas the structurally strained epoxy groups are unzipped by the nucleophilic substitution of *n*-alkylamines.[336] Some of the amines interact with the oxygen functionalities *via* hydrogen bonding as supported by the appearance of the N1 component. The weak acidic sites such as the carboxyl and phenolic groups interact with the amino groups through columbic interactions, induced by the transfer of H^+, as revealed by the N3 component.

The recovery of fluorescence after a laser photobleaching (FRAP) analysis was performed to assess whether the drug incorporation into the membrane could affect its fluidity. In fact, the lateral mobility of the lipid molecules within the membrane, quantified by the diffusion coefficient D at the solid interface, is an important indicator of the drug loading and release capabilities by the lipid bilayer platform. Supported lipid bilayers of rhodamine labelled POPC (PC-Rhod) and curcumin-loaded POPC (PC-Rhod-Curc) lipids were obtained by physical adsorption of the lipid vesicles on a hydrophilic glass followed by spontaneous rupture/fusion of the vesicles and the formation of the supported membranes.[337] FRAP results showed that both vesicles formed fluid supported membranes with a good mobility of lipids in both cases, since an almost complete

recovery of fluorescence after photobleaching was observed (Figure 44).

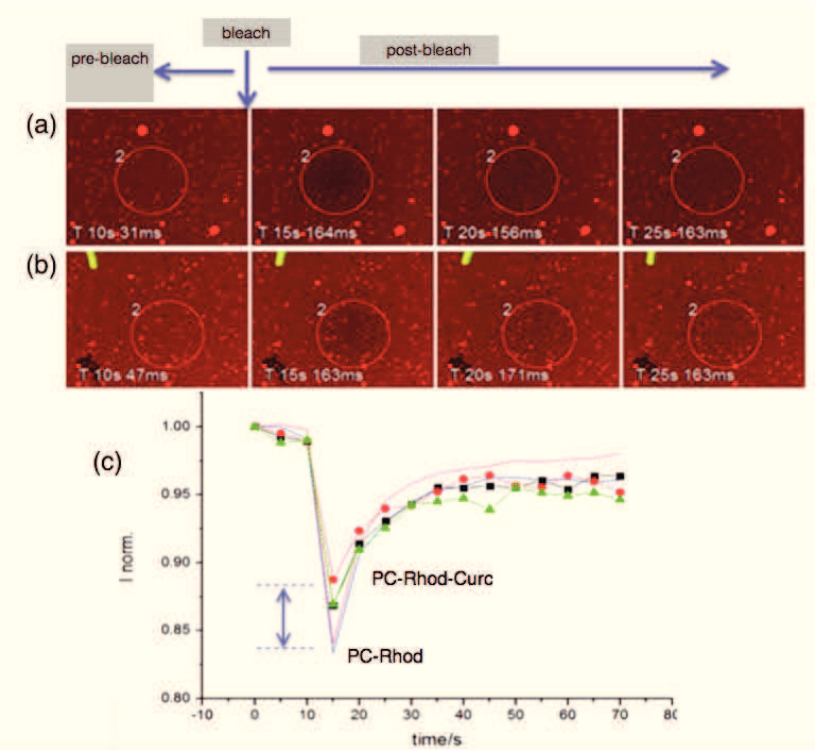

Figure 44. Confocal microscopy and FRAP analysis of rhodamine-labelled POPC without and with the loading of curcumin. Representative micrographs for FRAP experiments on: (a) POPC-Rhod; (b) POPC-Rhod-Curc. In (c): the curves of normalized emission intensity of rhodamine ($\lambda_{ex/em}$ = 543/550–650 nm) before and after photobleaching (POPC-Rhod = line; POPC-Rhod-Curc = line + symbol). Reproduced from Ref. 325 with permission from AIMS Materials Science.

Figure 44 show the representative micrographs of the FRAP experiment for PC-Rhod (Figure 44a) and PC-Rhod-Curc (Figure 44b), as well as the curves of normalized intensity before and after the photobleaching (Figure 44c). It must be noted that

the minimum, which corresponds to the first scan immediately after the bleach, is less pronounced for the Curc-loaded lipid membrane. This indicates a higher fluidity than the bare SLB. However, the diffusion coefficients, calculated by using the Axelrod's algorithm ($D = 0.88w^2/4\tau_{1/2}$, where w is the radius of the bleached area and $\tau_{1/2}$ describes time for 50% recovery)[338] is about 1.6–1.7 (±0.2) $\mu m^2/s$ for both PC-Rhod and PC-Rhod-Curc.

4.3.5.1 The Interaction of GO and N-GO Derivatives with Curc-loaded Lipid Membranes: Theoretical Calculations.

Molecular dynamics (MD) simulations were carried out to study the different interactions of amino-GO derivates at the interface with Curc-loaded biomembranes at pH values of 7.4 and 5.5, respectively. The distance between GO surface and the phenolic oxygen of curcumin was taken as a reference for this type of study. Figure 45 show the process below described.

Firstly, the loaded-Curc in lipid vesicles at the interface with amino-GO derivatives at the two pHs were investigated. In particular, at pH 7 the studies showed that the Curc remained inside the bilayer even if the molecule was subjected at wide fluctuations with the -OH groups facing the water layers and interacting, through electrostatic force and H-bond, with

phosphate, carbonyl groups of POPC and water molecules. Also, at this value of pH, a random orientation of the water molecules was found (Figure 45). Indeed, at pH 5 the fluctuations and the absolute distance curcumin-surface are smaller in comparison to pH=7. This means that mobility of Curc into the double layer is reduced and phenolic hydroxyl is kept away from the layer of water.

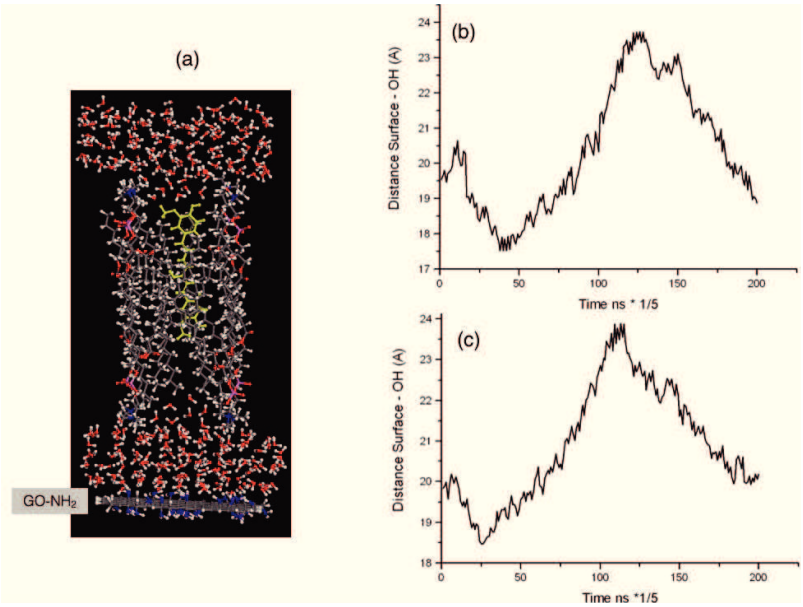

Figure 45. Curcumin intercalated in the POPC bilayer (a; carbon atoms are shown in grey, nitrogen atoms in blue and oxygen atoms in red spheres, curcumin molecule atoms are in yellow) and calculated distance between the amino-terminated N-GO surface and the phenolic oxygen of curcumin floating within the top and bottom leaflets of the lipid bilayer: (b) pH = 7; (c) pH = 5. Reproduced from Ref. 325 with permission from AIMS Materials Science.

Moreover, it is to note that the orientations of water molecules seem to be influenced by positive charges (GO-NH_3^+) located on the surface (Figure 46). Since long range electrostatic interactions, the negative side of the dipole associated to the water molecules mostly point toward the surface giving rise to a "V" prevailing orientation. As a consequence, the positive charge of the dipole, characterized by the hydrogen atoms, repels the partially positive charged hydrogen atom of the phenolic group (Ph-OH) pushing away the curcumin inside the double layer. Being due to the GO-NH_3^+ surface, such arrangement is not present in the water layer placed above the double layer. In fact, a random orientation of the dipoles is found in this layer therefore any repulsive effects, with respect to the Ph-OH group is observed.

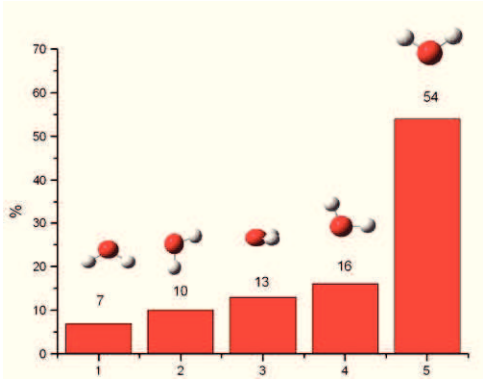

Figure 46. Statistically orientation of water influenced by electrostatic interaction at the GO interface. Reproduced from Ref. 325 with permission from AIMS Materials Science.

Finally, the mobility of curcumin within the POPC bilayer at the interface with N-GO samples obtained by GO+DDA treatment as well as with GO is represented in Figure 47a-b.

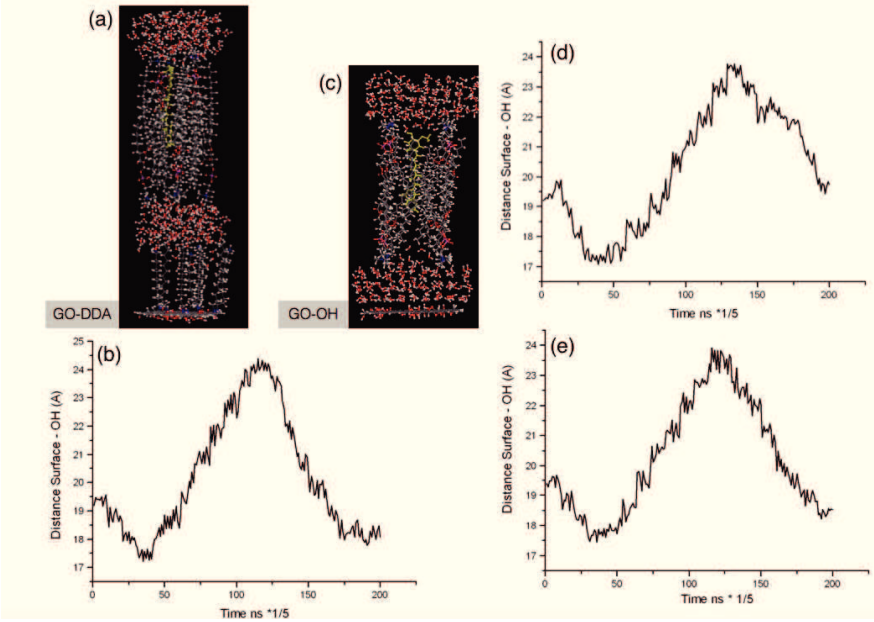

Figure 47. Calculated distance between the phenolic oxygen of curcumin floating within the top and bottom leaflets of the lipid bilayer and: (a, b) methyl-terminated N-GO surface; (c) hydroxyl-terminated GO surface at pH = 7 (d) and pH = 5 (e). Reproduced from Ref. 325 with permission from AIMS Materials Science.

In these cases, the effect of a pH variation is negligible. In fact, the layer of water and the nitrogen atoms in dodecylamine, which are directly bound to GO, are separated by a large distance. Simulation results show in both neutral and acid pH, a very low affinity between the functionalized surface and water

layer, which give rise to desorption of the entire system from the surface.

At neutral pH, the -OH groups in GO were considered deprotonated (GO-O^-) (Figure 47c). The overall effect is that the dipole associated to water molecules is oriented in a opposite way if compared to GO-NH_3^+. In the layer between surface and POPC water, molecules are mainly oriented with the positive side of the dipole toward GO-O^-. It follows that phenolic hydrogen atom of curcumin undergo an attractive interaction and, at the end of the side, its distance from the surface remains constant for a while (Figure 47d). Any relevant effect is observed in the proximity of the layer above POPC. At acid pH, the picture is essentially similar to GO-NH_2. Also in this case, a random orientation of dipole moment is detected and the mobility of curcumin is characterized by wide fluctuations (Figure 47e).

4.3.5.2 The Interaction of GO and N-GO Derivatives with Curc-loaded Lipid Membranes: Experimental Results

An experimental validation of theoretical calculations, discussed in the previous section, on the mobility of the curcumin within the POPC lipid bilayer at the interface with the different GO substrates was performed by confocal microscopy.

The confocal microscopy images for POPC-Rhod or POPC-Rhod-Curc adsorbed onto the different GO and N-GO substrates, prepared by the approach with GO solid, are shown in Figure 48.

The inhomogeneous distribution of red emission from the POPC-Rhod lipids highlights the graphene sheets (see the contrast in the merged fluorescence and optical images, ch02 + BF) in the hybrid glass-GO samples. The curcumin fluorescence is clearly visible on the different GO and N-GO sheets, with a particular enhancement of the green fluorescence on the top surface of the N-GO sheets prepared by dodecylamine reduction (Figure 48c, see the merged fluorescence and optical images, ch01 + ch02 + BF). This finding could be explained by the higher affinity of the hydrophobic curcumin towards the methyl-terminated N-GO sheets in comparison to the hydrophilic GO. According to that, the much larger regions with evident darker contrast in the red emission (Figure 48c, image ch02 + BF) fit well with a less favoured process of supported lipid bilayer formation from the spontaneous adsorption-rupture-fusion processes, as expected on a hydrophobic substrate.[339]

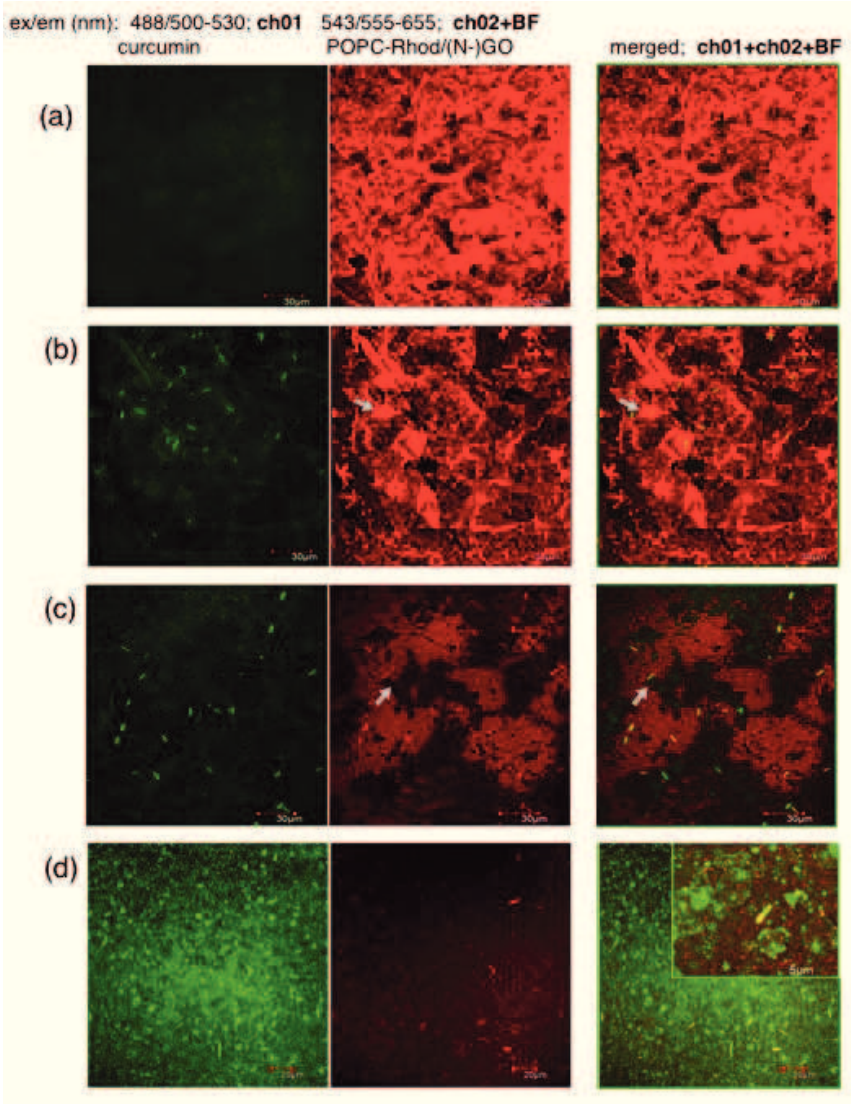

Figure 48. Confocal micrographs and bright field (BF) optical images of POPC-Rhod adsorbed on GO (a) and POPC-Rhod-Curc adsorbed on GO (b), methyl-terminated NGO (c), amino-terminated N-GO (d). The arrows point to some GO and N-GO sheets. Reproduced from Ref. 325 with permission from AIMS Materials Science.

Interestingly, for the amino-terminated N-GO surfaces the transfer of the drug to the substrate seems even more efficient, as demonstrated by the extensive green fluorescence (Figure 48d, see image ch01). Moreover, an effect similar to the reported formation of curcumin—induced lipid domains,[340] with the localization of the drug at the domain boundaries, is also visible (see inset in Figure 48d).

4.3.6 Conclusions

In summary, in the present work we investigated two functionalization strategies for graphene oxide in aqueous dispersion and for solid graphene, to prepare N-doped GO with different surface termination (e.g., outward exposure of methyl or NH_2 groups). The experimental characterisation by Raman, UV-visible and XPS spectroscopies demonstrated the actual modification of the GO, and allowed for the N-doping quantification. The interfaces established between such systems and curcumin-loaded lipid membranes was scrutinised by means on theoretical calculations, to elucidate both on the actual surface termination of the various GO samples at the interface with the lipid-curcumin system and on the pH-triggered release process of the curcumin. Experimental results validated the calculations as far as concerns the fluidity of the lipid bilayer (and the consequent freedom degrees of the curcumin intercalated within the membrane) and the promising

potentialities for the drug-release at the GO-lipid membrane interface, as demonstrated by the confocal microscopy studies. Further studies will elucidate on the impact of the used strategy for the modulation of the curcumin delivery at the graphene surfaces and the advantages of using the hybrid graphene oxide/lipid bilayer assembly for the release of the hydrophobic drug driven by specific chemical or physical stimuli.

4.3.7 Future Perspectives

Further GO functionalisation studies at the interfaces with biomolecules are actually in progress. In this context, the grafting of sulphur moieties at the GO surface (GO-XSH) has considered an interesting strategy for the fabrication of smart bio-sensing devices. [341 , 342] Until now, only plasma thiol-functionalization on carbon nanotubes and sulphur dioxide on GO were effectively investigated.[343,344] Our purpose is the study of GO-XSH obtained by radiofrequency plasma source in a H_2S/Ar gas mixtures. Preliminary results are not shown in this thesis, but they are collected in a manuscript for the submission.

4.4 Lateral-size controlled graphene oxide functionalised by polyacrylate grafting: an experimental and theoretical study for applications in theranostics.

An advanced application of GO nanosheets as theranostic platforms requires their surface engineered to get smart stimuli-responsive materials, *e.g.*, towards pH changes which are local environmental chemical markers of the tumour.

In the last few years a great number of reports focused on the fabrication of GO grafted with polyacrylic acid (PAA), for well-controlled mechanical characteristics and unique multiple pH response.[345]

Moreover, the lateral dimension of GO sheets is relevant for many biological phenomena on particle size, such as cell adhesion and spread on large sheets, cellular uptake of small GO sheets and cell deformation caused by interacting with GO. Furthermore, the antibacterial activity of GO has been related to the actual lateral dimension of GO sheets in various suspensions, which is strongly correlated with their dimension.[346] Therefore, the dimensions seem to regulate the differences in the toxicity of GO sheets functionalized with various molecules[347] due to the differential composition of the protein corona formed at their surfaces that determine their cell membrane interaction and cellular uptake.

The biomedical applications of GO derivatives as a drug delivery system need to investigate GO interactions with proteins in term of their structures and activities.

4.4.1 Plasma protein interactions: serum albumin.

Proteins are considered complex amphiphilic biopolymers, featuring hydrophobic and hydrophilic patches on their surfaces, which makes them well-known for the adhesiveness to solid surfaces.[348] Among biomacromolecules, serum albumin is the most soluble abundant protein in plasma. It has 585 amino acid residues that are arranged in three domains (I, II, III), each containing two subdomains (A, B).[349] It can bond to hydrophobic molecules and transport them to target tissues. Further, it commonly serves as a depository and a transport molecule for many exogenous compounds. Studies on the binding of drugs with plasma proteins will facilitate the interpretation of the metabolism and transport processes of such substances, and the binding of small molecules with bovine serum albumin (BSA) is a typical example of such interactions because of its hydrophilicity, biocompatibility, biodegradability and safety.[350] External stimuli (*e.g.*, pH) have also been reported to regulate the controlled release of drugs.[351] Thus, it is an appropriate protein to use for such investigations, partly because of its structural homology with human serum albumin (HSA).[352]

Generally, when an artificial biocompatible material is set in contact with circulating blood, the first step is the deposition of plasma proteins, mostly albumin, over its surface. Then, BSA can accumulate and stay in tumor tissues for a long time due to passive targeting by enhanced permeable reaction (EPR) effects and active targeting by gp60 receptors on the membrane of the cancer cells.[353] Moreover, BSA is also used as a good reductant due to its Tyr residues.[354] BSA proteins reduce and stabilize GO sheets to prepare BSA-GO/rGO conjugates with pH dependent solubility,[355] which can load drugs.

Doxorubicin hydrochloride (DOX) is an effective anticancer agent for leukemia chemotherapy but its clinical use has been limited because of side effects; thus, its delivery by various nanoparticles has been largely investigated. GO and reduced GO (rGO) have been already demonstrated to be promising nanocarriers for DOX.[356] Recently, Cheon et al. showed a NIR-mediated drug release of DOX from DOX-loaded bovine serum albumin-functionalized rGO nanosheets for chemo-photothermal therapy of brain tumor cells. [357]Also, DOXs were also linked to PAA-GO sheets which were internalised by cells, hence improving the loading efficacy of drugs in the delivery system.[358]

In this work, the fine lateral size control and the related surface charge of the GO sheets were found to be crucial for

the application of the GO at the (bio)interface. Specifically, pH-responsive GO-PAA, both at low (GO-PAA$_{thin}$) and high (GO-PAA$_{thick}$) acrylate grafting ratio, were synthesized and scrutinised by a combined theoretical and experimental approaches.

Moreover, implementing the concept of a DOX-albumin-GO assembly, recently demonstrated to exhibit an increased biocompatibility as well as promising features for NIR-mediated DOX release in photothermal therapy of tumours,[359,360] we further functionalised GO and GO-PAA nanosheets with both fluorescein-labelled albumin (emitting in the green range of wavelengths) and DOX (intrinsically fluorescent in the red). The graphene-mediated interaction between the two fluorophores was monitored in terms of fluorescence resonance energy transfer (FRET) processes at the GO(-PAA)/albumin/DOX interface, both in solution and *in vitro* intracellularly. Confocal microscopy confirmed the differential cellular uptake in neuroblastoma SH-SY5Y cells of these hybrid nano-bio-platforms.

Results showed the relevance of the GO lateral size for a reliable and reproducible derivatisation and to trigger the response at the liquid interface. A great potential of GO-PAA derivatives as tunable FRET and drug release platform for application in theranostics is demonstrated.[361]

4.4.2 Results and discussion

4.4.2.1 Nanosheets of GO and their characterization.

The GO sheets with different lateral sizes were prepared by sonication for 30, 80 and 120 min using a titanium cup-horn sonicator and centrifugation step to separate nanosheets (sub-micron lateral size) from bulky large sheets (up to several μm of lateral size), most likely assembled in the pellet (Figure 49).

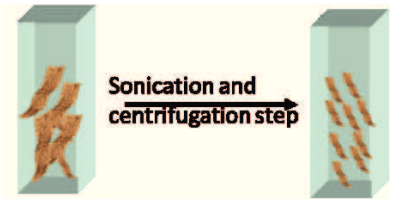

Figure 49. Nanosheets of GO obtained after sonication and centrifugation step.

The zeta potential of a colloidal dispersion is a marker of its stability, providing a quantitative measure of the effective surface charge associated with the double layer around the particles or the sheets, as in the case of GO. It is well known that GO forms a stable dispersion at pH >4, related to the presence of polar oxygen-containing groups at the sheets surface, especially concentrated along the edges.[362]

Figure 50 show the zeta potential (ZP) and the atomic force microscopy (AFM) results for graphene oxide pristine and sonicated in a time range from 30 minutes to 2 hours.

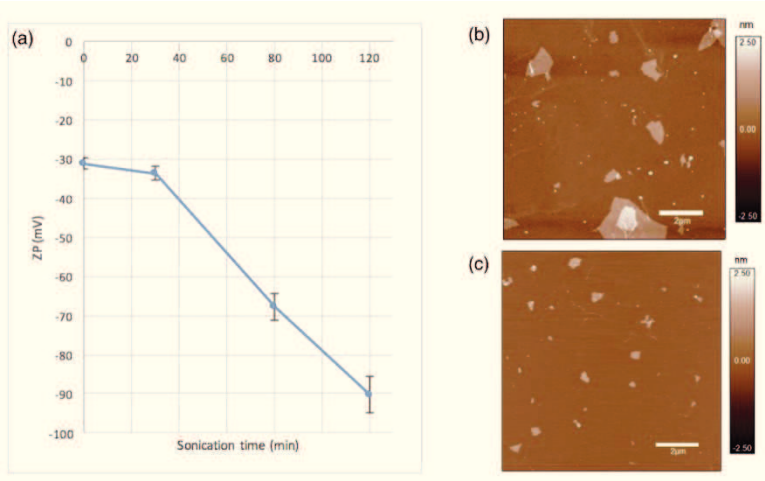

Figure 50 - (a) Zeta potential values measured for GO, pristine and sonicated for 30 min, 80 min and 120 min. AFM height images in AC mode in air of GO pristine (b) and GO sonicated for 120 min (c); bar = 2 μm; z-scale = 5 nm. Submitted to RSC Advances, ref. 361

The measured ZP value of pristine GO (~ -30 mV) was consistent with water soluble and dispersible GO sheets (Figure 50a).[363] The corresponding AFM topography image (Figure 50b) displays a distribution of micro- and nanosheets largely heterogeneous in the lateral size, with an average diameter of 458 ±484 nm (Figure 50b). A progressive decrease in the ZP values is measured for the GO sheets sonicated at increasing times until a ZP of ~ -90 mV was reached after a sonication time of 120 min. This effect was explained by the higher concentration of negatively charged groups at sheet edges as the lateral size of the sheet decreases. Indeed, a smaller and more homogeneous lateral size distribution (253 ±128 nm) of the GO

sheets sonicated for 120 min was found (Figure 50). These results were also confirmed by thermogravimetric analysis (TGA).

Another significant difference related to the lateral size of the GO sheets was found in the optical properties. Figure 51 show the UV visible spectra of GO, both pristine and sonicated samples, which exhibit the characteristic GO features: a band at 230 nm, corresponding to π-π* plasmon peak, and a shoulder at ~310 nm, corresponding to a n-π* plasmon peak.[364] The π-π* plasmon peak depends on two kinds of conjugative effect: one is related to nanometer-scale sp^2 clusters, and the other arises from linking chromophore units such as C=C, C=O and C–O bonds.[365] If all sp^2 clusters are treated as a single phenyl ring, spectral changes in GO should depend only on the effect of chromophore aggregation. Based on these considerations, that spectral shift of about 5 nm and the change of the UV-vis absorption intensity observed for sonicated GO (see insets in Figure 51) with respect to pristine GO can be explained in terms of the different number of linking chromophore units such as C–O and O=C, as indicated by ZP measurements before. Noteworthy, the curves recorded at two different pH values, 4 and 7.4, did not show any significant difference thus indicating that both pristine and sonicated GO are not sensitive to pH stimulus at the experimental conditions employed.

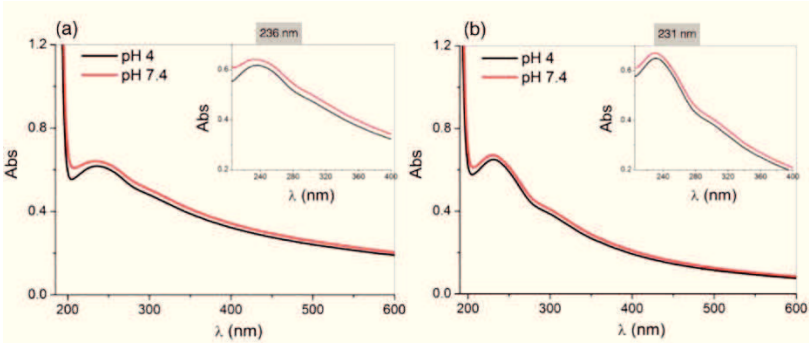

Figure 51. UV-visible spectra of aqueous dispersions of GO samples: pristine (a) and 120 min sonicated (b) at pH 4 and 7.4. Submitted to RSC Advances, ref. 361

In order to visualize GO-cell interaction, both pristine GO and 120 min sonicated GO were dye-labelled by adsorption of fluorescein-albumin and administered to human neuroblastoma cells by 1 and 2 hours of incubation in the culture medium supplemented with GO, either pristine or nanosheets.

Confocal microscopy results (Figure 52) show that, at short incubation times, pristine GO sheets as large as the size of the cells remained confined at the cell membrane whereas the nanosheets of the sonicated GO sample accumulated at the cell membranes (Fig. 52a).

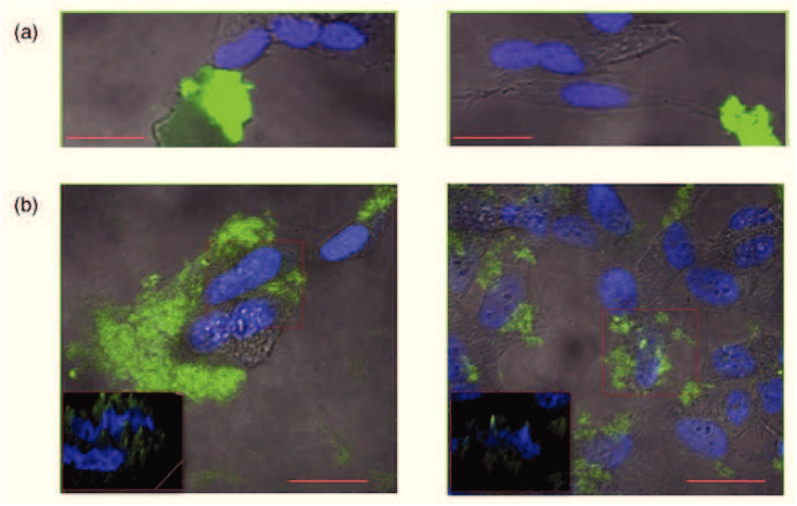

Figure 52. Merged optical bright field micrographs and fluorescence confocal images of nuclei (in blue, $\lambda_{ex/em}$ = 405/425 475 nm) and fluorescein-albumin labelled graphene (in green, $\lambda_{ex/em}$ = 488/500-530 nm) in SY-SH5H neuroblastoma cells incubated with 10 μg/mL of GO pristine (left panels) or GO nanosheets obtained by 120 min sonication (right panels) for 1 hour (a) and 2 hours (b). A detail corresponding to the dotted squatted area of reconstructed 3D images from xyz confocal scans is shown in the insets. Scale bar = 10 μm. Submitted to RSC Advances, ref. 361

After 2 hours of incubation (Fig. 52b) the larger GO sheets were still predominantly localised at the outer cell membrane, whereas GO nanosheets could reach a sub-cellular localisation including the nuclei (see the 3D image in the insets). Therefore, a fine tuning of the GO lateral size would be significant for specific cell targeting in the extracellular or intracellular environment, respectively.

4.4.2.2 PAA-GO derivative synthesis and characterization.

The dispersions of GO nanosheets which was homogenous in lateral size distribution (as obtained by 120 min of sonication) were used as substrate for the polyacrylate grafted-GO samples prepared at two different polymer chain lengths, namely an oligomeric PAA (henceforth named GO-PAA_{thin}) and a longer PAA chain (henceforth named GO-PAA_{thick}), depending on the AA monomer/GO ratio.

The effective functionalization and the different coverage of the GO sheets obtained for two different grafting ratios were determined by microscopy (AFM), mass spectrometry (ToF-SIMS and ESI-MS), thermogravimetry (TGA) and surface charge (ZP) measurements, and different spectroscopies (ATR-FTIR, Raman and XPS).

The results of AFM analysis of GO and PAA-grafted GO figured out a typical thickness of about 1.3 nm for GO (Fig. 53a). GO-PAA_{thin} sample exhibited a non-uniform height, generally ~2–6 nm in thickness (Fig. 53b), whereas a more homogeneous polymer coating is obtained for GO-PAA_{thick}, with thickness rising up to ~20 nm, together with a distinct propensity towards aggregation of the colloidal graphene sheets (Fig. 53c). Moreover, significant changes in roughness were measured, from R_q = 0.09±0.02 nm in GO to R_q=1.2±0.3 nm and R_q=4.9±2.3 nm for GO-PAA_{thin} and GO-PAA_{thick}, respectively.

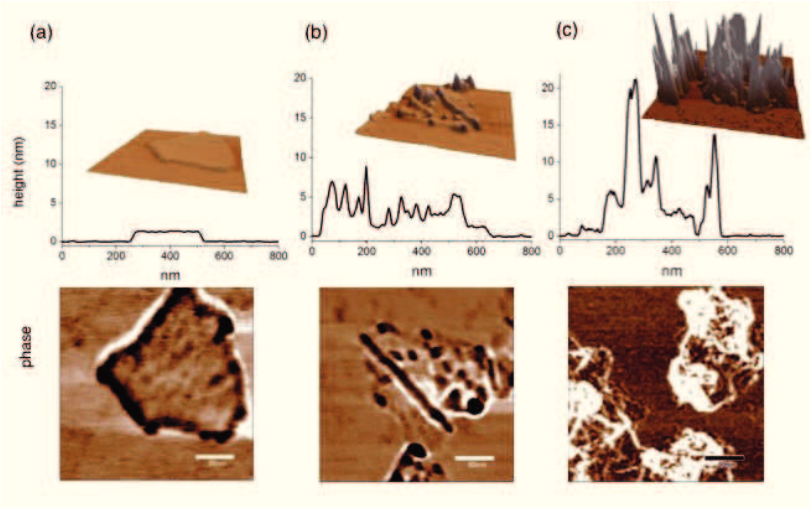

Figure 53. AFM section analysis and 3D height (xy scale = 1x1µm^2; z scale = 20 nm) (top) and phase (bottom) images of: (a) GO; (b) GO-PAA$_{thin}$; (c) GO-PAA$_{thick}$. Submitted to RSC Advances, ref. 361.

It is to note that the phase images showed darker regions at the sheet edges of GO but distributed in rounded-shaped flange features onto the sheet surface of GO-PAA$_{thin}$, respectively.

Such regions could be assigned to the polar oxygen-containing moieties and the resulting specific tip-surface interaction. This was expected to differ for the case of the longer polymer chain of GO-PAA$_{thick}$, where a major contribution from dispersive van der Waals forces could be invoked, and explained the aggregation effect discussed above. Accordingly, GO-PAA$_{thick}$ exhibited brighter area in the phase image corresponding to the rounded shapes protruding from the sheet surface.

These results revealed that in the hybrid graphene-polymer system, the polyacrylate grafting onto GO sheets did not change

the average size of the sheets, still ranging from few hundreds to about 1 micron, but increased the thickness of GO at different levels of heterogeneities. In particular, in GO-PAA_{thin}, the polymer left surface areas of the substrate uncovered, with preferential growth at the GO edges. Therefore, the grafting of PAA thin films was not expected to considerably inhibit the access of foreign molecules/particles close to the graphene surface and this could be a significant advantage for optical sensing and drug loading/release based applications.

XPS analysis of GO and GO-PAA samples allowed for the characterisation of the surface oxidation as well as of the efficiency of PAA grafting. The average atomic composition shows that both GO-PAA_{thin} and GO-PAA_{thick} exhibit surface amounts of carbon and oxygen comparable to those of GO, with respectively 68.3 at.% of C and 31.0 at.% of O, and additional traces of sulphur (0.4 at.%), owing to the synthesis procedure of colloidal graphene oxide. [366]

For the PAA-functionalized GO samples, a small amount of Ce (~1 at. %), which is the catalyst used for the acrylate monomer polymerization reaction, was found. The curve fitting analysis of C 1s and O 1s peaks (Figure 54) and the overall ratio calculated between the deconvoluted components provided quantitative indications on the possibility to tune the number of polar groups outwards exposed by the lateral size of the nanosheets (i.e., sonicated surface vs pristine) and by the

acrylate grafting ratio (i.e., GO-PAA$_{thin}$ and GO-PAA $_{thick}$ vs. GO).

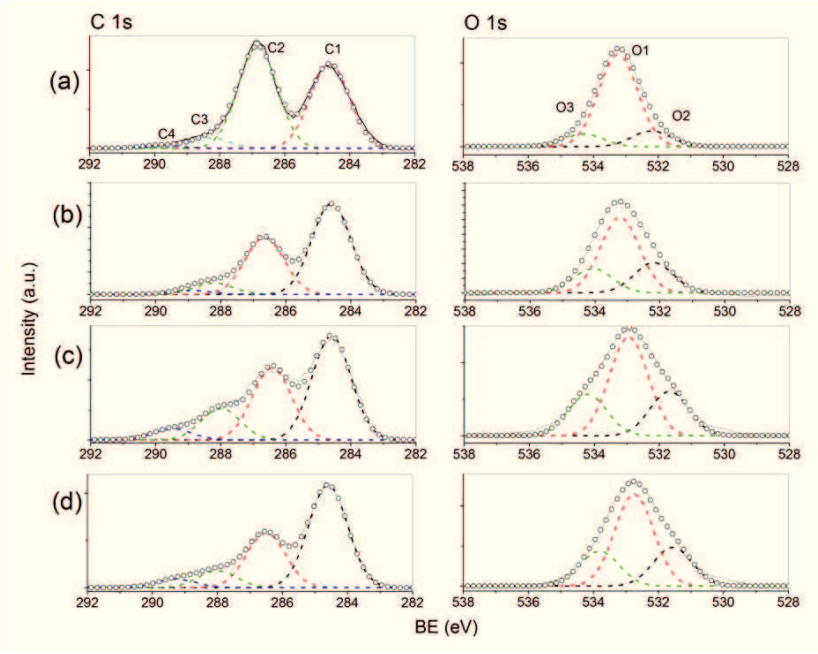

Figure 54. High resolution XPS spectra of C 1s and O 1s regions (solid line, experimental curves) with curve fitting (scatter points=convolution curve; dashed lines=peak components) of: (a) GO pristine; (b) GO sonicated; (c) GO-PAA$_{thin}$; (d) PAA$_{thick}$. Submitted to RSC Advances, ref. 361.

Peak fitting analysis was performed according to the peak components assignation described as follows. The C 1s peak component at binding energy (BE) around 284.5 eV was assigned to CC/CH bonds (C1); those at 286.4 eV (C2), 288.0 eV (C3) and 290.0 eV (C4) are typically attributed to C-O, C=O, and O=C-O groups, respectively. [367] Most structural models of GO also include an epoxide group (C-O-C), which should be centred at BE similar to that of C-OH. The O1s peak component

at 532.8 eV (O1) was assigned to C-O single bonds, the 532.0 eV (O2) component to C=O and O=C–OH groups[368] and that at 533.4 eV (O3) to O=C–OH and C–OH groups. [369]

The sonication process of GO samples produce a significant change in C1s peak shape, with the relative decrease of C2/C1, that was the area ratio between the C components attributed to ether groups and the hydrocarbon CC and CH bonds of the sp^2 domains, respectively. Similarly, in the O1s peak the (O2+O3)/O1 ratio increase. These two findings, taken together, indicate that the sonication-induced decrease of lateral size in GO was also associated to a partial oxidation of the CO bonds.

As to GO-PAA samples, it is known that C 1s peak of sp^2 carbon becomes asymmetric and broadened towards the high binding energy side as the amount of polar functional groups increases. [370] Accordingly, a significant modification of C1s peak shape for GO-PAA samples (Fig. 54c-d) in comparison to uncoated GO (Fig. 54) pointed toward the increase of relative contributions from carbon-oxygen double bonds (C3 and C4 components) and the decrease of carbon-oxygen single bonds (C2 component) with respect to graphitic (sp^2) and hydrogen-bonded carbon (C1 component). This decrease was especially evident for GO-PAA_{thick} than in GO-PAA_{thin}, in agreement with what expected by the different grafting ratios used. In the same way, the O1s peaks of GO-PAA samples exhibited the relative increase of contribution assigned to carbonyl (O2) and hydroxyl

(O3 component) groups with respect to the CO single bonds (O1 component). Both GO-PAA_{thin} and GO-PAA_{thick} exhibited similar spectra, and a comparable C1:C2:C4 area ratio of ~10:6:1. This value differed from the ratio of ~4:1:1 from standardized XPS studies of polyacrylic acid.[371] Such a finding, together with the presence of carbonyl-related components C3 and O1, which were not present in the standard PAA spectra, suggested that the samples showed polymer-uncovered GO areas. It has to be noted that the XPS samples were prepared by depositing concentrated films of GO-PAA_{thin} and GO-PAA_{thick} dispersion to obtain a thickness equal at least to the XPS sampling depth (i.e., about 6 nm at the applied experimental conditions, as confirmed by the absence of signals from the silicon substrate).

Mass spectrometry analysis by both ToF-SIMS and ESI-MS were used to take advantage of their specific features, namely the sampling depth confined to the outermost surface (~ 1 nm) of ToF-SIMS, and the large molecules detection capability of ESI-MS, respectively.

ToF-SIMS positive ion spectra do not visibly show significant differences between GO, GO-PAA_{thin} and GO-PAA_{thick} regarding expected fragments originating from the PAA monomer (Figure 55). However, the PC1-PC2 score plots obtained from PCA interpretation of the three samples showed that these ones were well discriminated (Fig. 55d).

In fact, PC1 explained 55.2% of the variance, and this one enables assessment of spectral differences between all three samples, because GO-PAA_{thick} were located at PC1>0, GO samples were located at PC1<0, while GO-PAA_{thin} samples displayed intermediate PC1 scores (≈ 0). In this way, we might intuitively understand that the PC1 scores increasing was associated with the coverage degree of GO samples by the PAA layer.

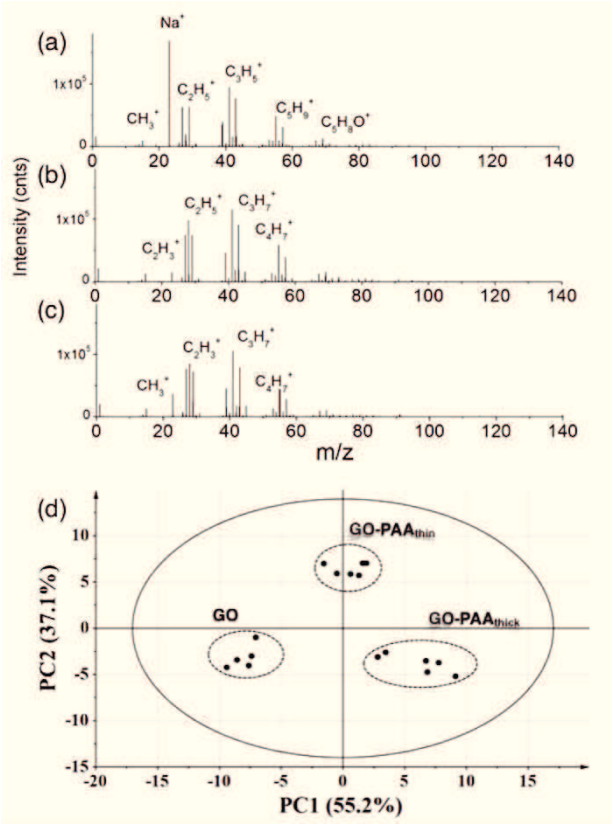

Figure 55. Positive ToF-SIMS spectra of GO (a), GO-PAA_{thin} (b), GO-PAA_{thick} (c) and corresponding score plot (d) obtained from PCA analysis (at least five spectra for each sample). Submitted to RSC Advances, ref. 361.

The analysis of most significant peaks extracted by PCA points to the predominance of hydrocarbon fragments ($C_xH_y^+$) in comparison to oxygenated hydrocarbon ($C_xH_yO_z^+$) species in the ToF-SIMS spectra GO-PAA_{thick} (PC1>0). This observation was in line with the expected increase in hydrocarbon composition of PAA in comparison with the highly oxygen-functionalized GO substrate. Moreover, XPS results display a significant increase in the CC/CH bonds component in the C1s spectra, in comparison to the C1s spectrum of GO. In this way, the interpretation of PC1 was further validated with support of XPS data.

In addition to PC1, the second principal component was mandatory to consider, as it captured 37.1 % of the variance. This one helped to further discriminate the three samples, particularly GO-PAA_{thin} and GO. By examination of the most significant peaks related to PC2 > 0, we noticed a number of hydrocarbon peaks ($C_xH_y^+$) which was still significant comparatively to the oxygenated hydrocarbon peaks ($C_xH_yO_z^+$), but lower than what was observed for the interpretation of PC1. We might tentatively interpret these data by the ToF-SIMS detection of uncovered area in the case of GO- PAA_{thin} samples. Regarding on the ESI-MS analysis, although this was the first time that a mass spectrometric characterization for the functionalized GO was carried out, in the mass spectra it is

possible to recognize some features that are specific for the PAA polymer.

The spectroscopic characterisation by UV-visible confirmed the responsiveness to the pH and ionic strength stimuli in water of GO-PAA samples (Figure 56).

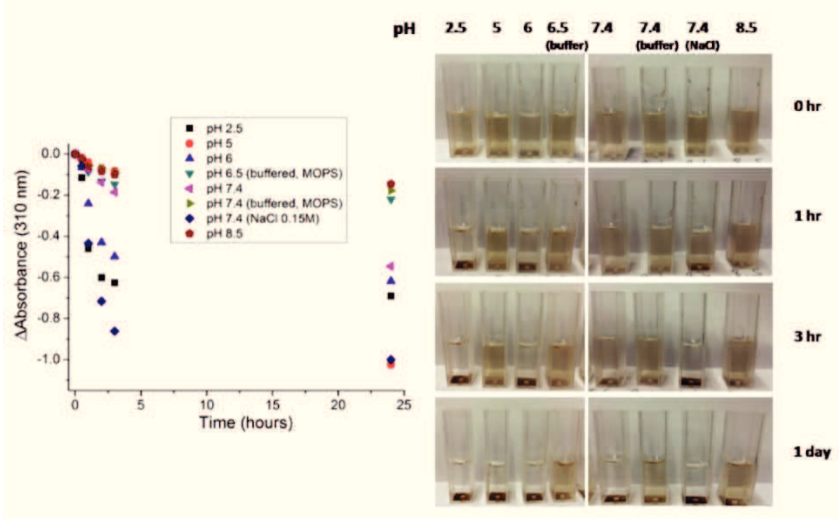

Figure 56. Plot of the normalized absorbance ($\Delta Abs = Abs_{(t)} - Abs_{(t=0)}$ at 310 nm) vs. time of GO-PAA_{thin} aqueous dispersions prepared at different pH (left). Images of GO-PAA_{thin} samples, prepared at different pH, collected at different time intervals (right). Submitted to RSC Advances, ref. 361.

Moreover, the ATR/FT-IR and Raman studies demonstrated the actual PAA grafting (Figure 57). In particular, the GO characteristic stretching modes of OH (at 3300 cm^{-1}), C=O (at 1725 cm^{-1}), C-O (at 1050 cm^{-1}) and C-OH (at 1220 cm^{-1}) moieties, reduced in intensity for GO-PAA_{thin} and GO-PAA_{thick}. The analysis of Raman spectra indicated that both the lateral size decreasing effect due to ultrasonication and the polymer grafting

induced an increase of the defects, in turn related to the I_D/I_G ratio increase in the in-plane crystallite, which can be attributed to a decrease of the sp^2 regions.

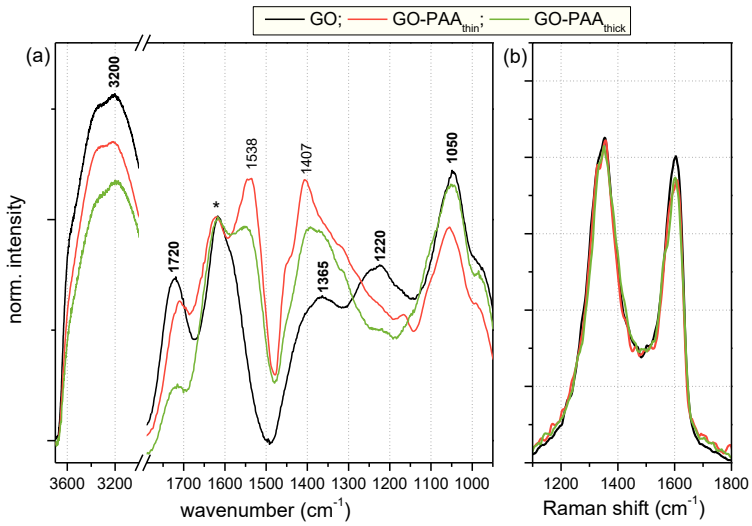

Figure 57. ATR/FTIR (a) and Raman (b) spectra of GO, GO-PAA$_{thin}$ and GO-PAA$_{thick}$ samples. The asterisk in (a) points to the peak at 1622 cm^{-1}, typical of skeletal vibration in unoxidized graphitic domains, used for spectra normalisation. Submitted to RSC Advances, ref. 361.

GO nanosheets surface successfully tailored by the PAA grafting with the related ratio of oxygenated to non-oxygenated groups, was, in turn, expected to significantly affect the optical response at the interface with water. These findings were confirmed both with theoretical calculations and spectroscopic analysis.

Particularly, UV-visible and fluorescence spectra of GO-PAA samples dissolved in ultrapure water (pH ~5) or in PBS buffer

(pH 7.4) (Figure 58) confirmed the strong interaction with the water molecules of the carboxylate groups at the surfaces of GO-PAA, not only for the pH-dependent aggregation but also for the optical properties at the aqueous interface.

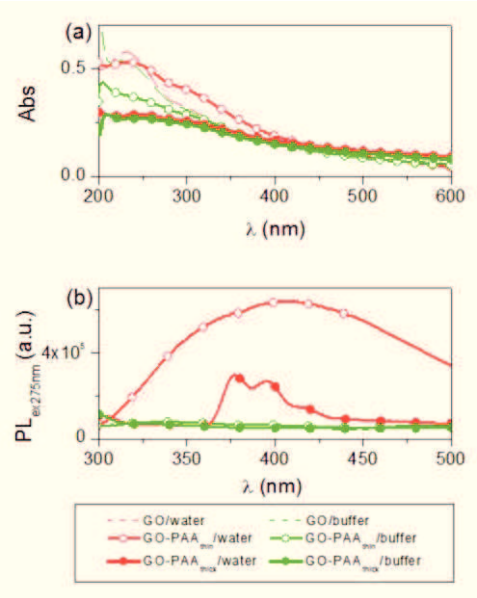

Figure 58. Comparison of UV visible (a) and fluorescence (b; excitation wavelength = 275 nm) spectra in water (pH <6) and in PBS buffer (pH = 7.4) of GO, GO-PAA$_{thin}$ and GO-PAA$_{thick}$. Submitted to RSC Advances, ref. 361.

The absorption spectrum of GO-PAA$_{thin}$ with carboxyl groups protonated (i.e., in water) exhibited a significant increase of the peak at ~310 nm in comparison to GO, likely due to the increased role of n-π* transition of the C=O bonds of the PAA chains grafted at the GO surface. For GO-PAA$_{thin}$ in PBS, both the π-π* plasmon peak at 230 nm and the shoulder at 310 nm decrease. This effect was related to the ionized carboxyl acid

groups, which influenced the electronic conjugation between the GO sheets. In the case of GO-PAA_{thick}, the π-π* plasmon peak at 230 nm decreases and no differences are observed for the different pHs. This might be attributed to the lowering of sp^2 domain size with the increased PAA grafting ratio, defect level transition, and structural changes,[372] which influenced the electronic structure of the GO nanosheets.

As to fluorescence spectra, it is to note the absence of emission at 443 nm[373] in uncoated GO, according to the presence of many oxygen-containing polar moieties such as epoxy, carboxyl, and hydroxyl groups causing a greater proportion of nonradiative decay of excitons. Similarly, a weak emission of GO-PAA was found at pH >6, where ionization of carboxylic acid groups likely causes an increase of the accessibility of electrons responsible for nonradiative recombination of holes of GO. A broad emission band was instead observed for GO-PAA at pH <6, with protonation of carboxyl groups and therefore a reduced role of nonbonding electrons responsible for nonradiative exciton recombination. It is to note that GO-PAA_{thick} yields a lower fluorescence intensity than GO-PAA_{thin}. This was attributed to the increased disorder of the graphitic structure due to grafting of higher amount of PAA on the GO surface.

4.4.2.3 Studies of GO and GO-PAA at the biointerface with albumin, doxorubicin and cells (theranostic target).

The potential theranostic platform assembled by GO (or GO-PAA_{thin}) with BSA-FITC (imaging factor) and DOX (drug factor) was scrutinised both in solution, by fluorescence spectroscopy, and in cells, by confocal microscopy. Figure 59 shows the two relevant steps in the assembling of the GO(-PAA)/albumin/DOX system. Specifically, Fig.59a-b displayed the graphene-induced quenching of fluorescein emission,[374] when the protein was put in contact either with GO or GO-PAA.

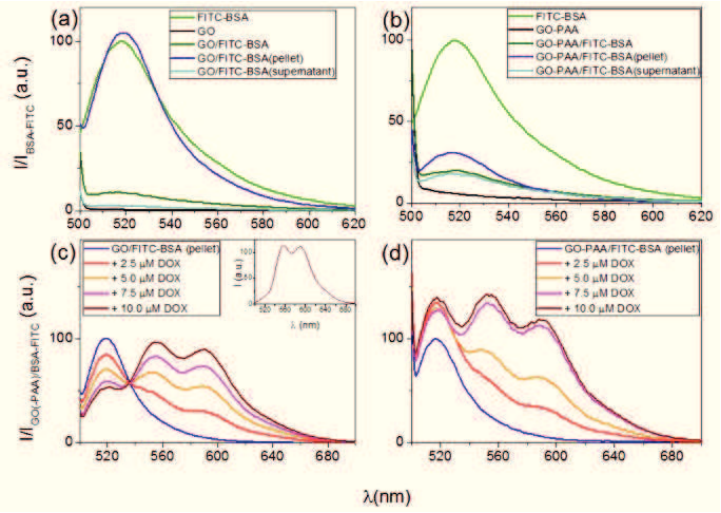

Figure 59. (a-b): Emission spectra (λex=488 nm) in PBS of GO (18 μg/mL, a) and GO-PAA_{thin} (13.4 μg/mL, b) at the interface with FITC-BSA (23 μg/mL), before and after centrifugation. (c-d) Fluorescence titration experiments in PBS for GO/FITC-BSA (c) and GO-PAA/FITC-BSA (d) by the addition of DOX at increasing concentrations (2.5-10 μM). In the inset of (c) the reference emission spectrum of 10 μM DOX in PBS is showed. Submitted to RSC Advances, ref. 361.

It must be noted that the fluorescence quenching was more effective for GO than for GO-PAA, likely due to hindering effects by the polymer coating.

After the centrifugation step, performed to remove unbound and/or loosely bound protein, the collected pellet, resuspended in PBS to a dilution factor of 1 to 2000, exhibited an almost complete recovery of fluorescence for GO/FITC-BSA (Fig. 59a). This finding cannot be attributed to the detachment of the protein from the GO surface, since a protein coating of ~46% was estimated by XPS analysis, according to a detected N1s concentration of ~6.1 % in comparison to ~13.2 % of bulk albumin (Table 3). On the other hand, the fluorescence recovery of GO-PAA/FITC-BSA, where the estimated protein coverage is ~15%, was less evident (Fig.59b). These results could be explained by the different average orientation and/or distance of the fluorescein-albumin with respect to the GO substrates. The emission spectra in solution of the GO/BSA-FITC system by addition of DOX at increasing concentration (Fig. 59c) show the typical trend of the energy transfer processes, with the decrease in intensity of the fluorescein peak at 530 nm (donor) and the corresponding increase of DOX emission (acceptor). Excitation spectra confirmed that an actual FRET process occurs, since the emission intensity were corrected for inner filter effects and

concentration changes.[52] Marked differences in the photophysical processes of energy transfer in the case of GO-PAA are instead found (Fig. 59b).

The drug delivery capability of the GO/albumin/DOX assemblies were assessed by a proof-of-work confocal microscopy study of the uptake in neuroblastoma cells after 2 h of incubation (Figure 60).

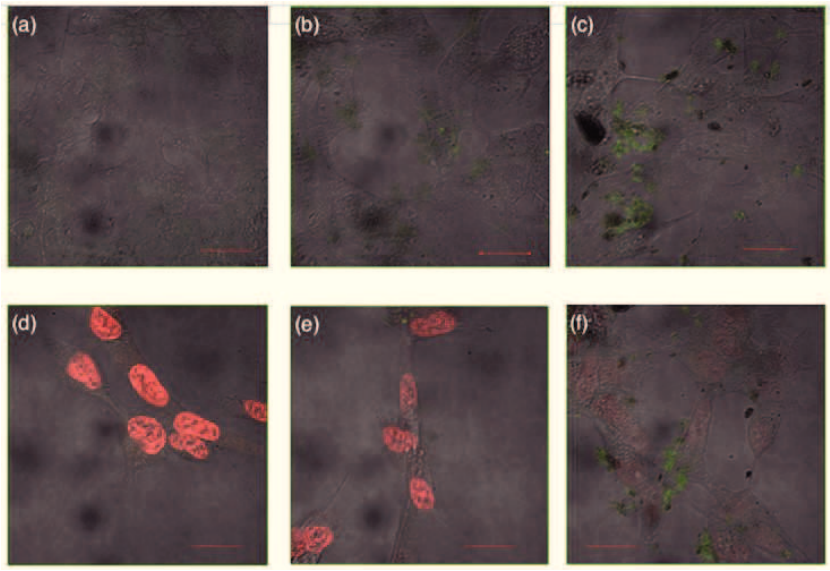

Figure 60. Merged optical and fluorescence confocal microscopy micrographs (FITC-BSA in green: ex/em = 488/500-530 nm; DOX in red: ex/em = 543/550-650) of neuroblastoma cells incubated 2 h with: (a) GO; (b) GO-albumin; (c) GO-PAA-albumin; (d) DOX; (e) GO-albumin-DOX; (f) GO-PAA-albumin-DOX. Bar = 20 μm. Submitted to RSC Advances, ref. 361

Both GO/FITC-BSA (Fig. 60b) and GO-PAA/FITC-BSA (Fig. 60c) were clearly internalised by the cells.

The polyacrylate-grafted GO exhibited a more inhomogeneous sub-cellular distribution than GO, as marked by the spotted green emission of the fluorescein-labelled albumin coating the nanosheets. The DOX uptake is shown in Fig. 60d-e for the free drug (10 μM) and DOX loaded in GO-albumin (2 μM) or GO-PAA-albumin (5 μM), respectively. The graphene oxide platforms, both uncoated (Fig.60e) and polyacrylate-coated (Fig. 60f), were effective in the delivery of DOX into the nucleus, as deduced from the comparison to control cells after the drug administration at a concentration five times higher than in the case of GO-PAA (Fig. 60d). The brighter green emission of GO-PAA/FITC-BSA within cells (Fig. 60f) in comparison to GO /FITC-BSA (Fig. 60e) demonstrated also the fluorescence imaging capability of this platform that, coupled to the drug release properties, demonstrated its promising potentialities for theranostics.

4.4.3 Conclusion

In this work, we studied PAA-grafted graphene oxide nanosheets of suitable and homogeneous lateral size with a specific focus on the optical response at the aqueous interface. Indeed, the sub-micrometer-large GO exhibited a more negative surface charge, a blue-shift of the π-π* plasmon peak and a more diffuse cellular uptake, which extends also to the nuclei. The grafting ratio of acrylate monomer was found crucial not only to

provide the pH-responsiveness character but also for the actual surface termination of the PAA-coated GO substrates, which in turn affected their optical response at the water interface.
Fluorescence resonance energy transfer experiments in solution demonstrated the different fluorescence imaging capability of GO and GO-PAA in the graphene oxide/fluorescein-labelled albumin/doxorubicin hybrid assembly. The drug delivery and imaging capabilities were validated by confocal microscopy experiments that therefore confirmed the promising potentialities of the developed nanoplatform for theranostics.

4.4.4 Future perspectives.

Further GO functionalization with copolymers sensitive to both temperature and pHs will be synthesized and characterized to scrutinize potential theranostic applications.

List of abbreviations

(AAV) Adeno-associated viral vector
(AD) Alzheimer's Disease
(AFM) Atomic Force Microscopy
(AgNPs) Silver nanoparticles
(Ajs) Dherent junctions
(ALS) Amyotrophic lateral sclerosis
(AMF) Alternating magnetic field
(BBB) Blood-brain barrier
(BDNF) Brain Derived Neurotrophic Factor
(BE) Binding energy
(bFGF) Basic fibroblast growth factor
(BM) Basement membrane
(BSA) Bovine serum albumin
(CD) Circular dichroism
(CNS) Central nervous system
(CNT) Carbon nanotube
(CUR) Curcumin
(CVD) chemical vapor deposition
(Cys) cysteine
(DHPE) 1,2-dihexadecanoyl-*sn-glycero*-3-phosfoethanolamine
(DOX) Doxorubicin
(DOX-BSA-rGO) DOX-loaded BSA-functionalized rGO
(EC) Endothelial cells
(ECM) Extracellular matrix
(EILDV) Glu-Ile-Leu-Asp-Val
(EPR) Enhanced permeability and retention
(EPR) Enhanced permeable reaction
(FAM) Carboxyfluorescein
(FCS) Fluorescence correlation spectroscopy

(FET) Field Effect Transistor
(FRAP) Fluorescence recovery after photobleaching
(FRET) Fluorescent resonance energy transfer
(G) Graphene
(GC) Glycine-cysteine
(Gly) Glycine
(GNFs) Graphene family nanomaterials
(GO) Graphene oxide
(GO-DDA) GO-dodecylamine
(GO-N_2H_4) GO-hydrazine
(HSA) Human serum albumin
($HAuCl_4$) Hydrogen tetrachloroaurate
(HB-GFs) Heparin-binding growth factors
(HD) Huntington's disease
(HIF) Hypoxia-inducible factor
(HSA) Human serum albumin
(iHBMEC) Immortalized Human Brain Microvascular Endothelial Cells
(LSPR) Localized surface plasmon resonance
(MALDI-TOF/MS) matrix-assisted laser desorption/ionization time-of-flight mass spectrometry
(MD) Molecular dynamics
(MEF) Metal Enhanced Fluorescence
(MMPs) Matrix metalloproteinases
(MNPs) Magnetic nanoparticles
(NGF) Nerve Growth Factor
(NMs) Nanomaterials
(NOS) Nitrogen oxygen species
(NPs) Nanoparticles

(NVU) Neurovascular unit
(PAA) Polyacrylic acid
(PC) Pericytes
(PD) Parkinson's Disease
(PDGF) Platelet-derived growth factor
(PDT) Photodynamic therapy
(PEG) Poly(ethylene glycol)
(PHMS) Poly(hydroxymethylsiloxane)
(PL) Photoluminescence
(PLGF) Placenta growth factor
(PLL) Poly(L-lysine)
(PMAA) Poly(methacrylic acid)
(PMMA) Polymethylmethacrylate
(PNIPAM) Poly(N-isopropylacrylamide)
(POPC) 1-palmitoyl-2-oleoyl-*sn-glycero*-3-phosphocholine
(PS) Polystyrene
(PTT) Photothermal therapy
(PVA) Poly (vinyl alcohol)
(PVP) Poly(vinylpyrrolidone)
(QCM-D) Quartz crystal microbalance with dissipation monitoring
(REDV) Arg-Glu- Asp-Val
(RGD) Arg-Gly-Asp
(rGO) Reduced graphene oxide
(ROS) Reactive oxygen species
(SERS) Surface Enhanced Raman Spectroscopy
(SLBs) Supported lipid bilayers
(SMT) Single molecule tracking

(SPR) Surface plasmon resonance
(SUVs) small unilamellar phospholipid vesicles
(SVLs) Supported vesicular layers
(TEER) Trans-endothelial electrical resistance
(TGA) Thermogravimetric analysis
(TJs) Tight junctions
(ToF-SIMS) Time of Flight-second Ion mass spectrometry
(UV) Ultra-violet
(VEGF) Vascular Endothelial Growth Factor
(XPS) X-Ray Photoelectron Spectroscopy
(ZP) Z-Potential
(ΔD) Delta dissipation
(Δf) Delta frequency

References

[1] Moghimi, S. M., Hunter, A. C., & Murray, J. C. (2005). Nanomedicine: current status and future prospects. *The FASEB journal*, *19*(3), 311-330.

[2] (a) Kelkar, S. S., & Reineke, T. M. (2011). Theranostics: combining imaging and therapy. *Bioconjugate chemistry*, *22*(10), 1879-1903; (b) Lammers, T., Aime, S., Hennink, W. E., Storm, G., & Kiessling, F. (2011). Theranostic nanomedicine. *Accounts of chemical research*, *44*(10), 1029-1038.

[3] Funkhouser, J. (2002). Reinventing pharma: The theranostic revolution. *Curr. Drug Discovery*, *2*, 17-19.

[4] Siegel, R. W. (1993). Nanostructured materials-mind over matter. *Nanostructured Materials*, *3*(1-6), 1-18.

[5] Liu, R., Duay, J., & Lee, S. B. (2011). Heterogeneous nanostructured electrode materials for electrochemical energy storage. *Chemical Communications*, *47*(5), 1384-1404.

[6] Albanese, A., Tang, P. S., & Chan, W. C. (2012). The effect of nanoparticle size, shape, and surface chemistry on biological systems. *Annual review of biomedical engineering*, *14*, 1-16.

[7] Canton, I., & Battaglia, G. (2012). Endocytosis at the nanoscale. *Chemical Society Reviews*, *41*(7), 2718-2739.

[8] Albanese, A., Sykes, E. A., & Chan, W. C. (2010). Rough around the edges: the inflammatory response of microglial cells to spiky nanoparticles. *ACS nano*, *4*(5), 2490-2493.

[9] Jain, R. K., & Stylianopoulos, T. (2010). Delivering nanomedicine to solid tumors. *Nature reviews Clinical oncology*, *7*(11), 653-664.

[10] Choi, H. S., Liu, W., Misra, P., Tanaka, E., Zimmer, J. P., Ipe, B. I., ... & Frangioni, J. V. (2007). Renal clearance of quantum dots. *Nature biotechnology*, *25*(10), 1165-1170.

[11] Rao, C. N. R., Kulkarni, G. U., Thomas, P. J., & Edwards, P. P. (2002). Size-dependent chemistry: properties of nanocrystals. *Chemistry–A European Journal*, *8*(1), 28-35.

[12] Discher, D. E., Janmey, P., & Wang, Y. L. (2005). Tissue cells feel and respond to the stiffness of their substrate. *Science*, *310*(5751), 1139-1143.

[13] Geim, A. K. (2009). Graphene: status and prospects. *science*, *324*(5934), 1530-1534.

[14] (a) Kim, K. S., Zhao, Y., Jang, H., Lee, S. Y., Kim, J. M., Kim, K. S., ... & Hong, B. H. (2009). Large-scale pattern growth of graphene films for stretchable transparent electrodes. *nature*, *457*(7230), 706-710; (b) Park, J. U., Nam, S., Lee, M. S., & Lieber, C. M. (2012). Synthesis of monolithic graphene–graphite integrated electronics. *Nature materials*, *11*(2), 120-125.

[15] Bae, S., Kim, H., Lee, Y., Xu, X., Park, J. S., Zheng, Y., ... & Kim, Y. J. (2010). Roll-to-roll production of 30-inch graphene films for transparent electrodes. *Nature nanotechnology*, *5*(8), 574-578.

[16] Nam, S., Lee, M. S., & Park, J. U. (2012, August). Monolithic graphene transistor biointerface. In *Engineering in Medicine and Biology Society (EMBC), 2012 Annual International Conference of the IEEE* (pp. 5678-5678). IEEE.

[17] Cuenot, S., Frétigny, C., Demoustier-Champagne, S., & Nysten, B. (2004). Surface tension effect on the mechanical properties of nanomaterials measured by atomic force microscopy. *Physical Review B*, *69*(16), 165410.

[18] Fan, H., Wang, L., Zhao, K., Li, N., Shi, Z., Ge, Z., & Jin, Z. (2010). Fabrication, mechanical properties, and biocompatibility of graphene-reinforced chitosan composites. *Biomacromolecules*, *11*(9), 2345-2351.

[19] Fan, H., Wang, L., Zhao, K., Li, N., Shi, Z., Ge, Z., & Jin, Z. (2010). Fabrication, mechanical properties, and biocompatibility of graphene-reinforced chitosan composites. *Biomacromolecules*, *11*(9), 2345-2351.

[20] Weissleder, R. (2001). A clearer vision for in vivo imaging. *Nature biotechnology*, *19*(4), 316-316.

[21] Vogel, A., & Venugopalan, V. (2003). Mechanisms of pulsed laser ablation of biological tissues. *Chemical reviews*, *103*(2), 577-644.

[22] Chuang, C. H., Lo, S. S., Scholes, G. D., & Burda, C. (2010). Charge separation and recombination in CdTe/CdSe core/shell nanocrystals as a function of shell coverage: probing the onset of the quasi type-II regime. *The Journal of Physical Chemistry Letters*, *1*(17), 2530-2535.

[23] Jain, P. K., Lee, K. S., El-Sayed, I. H., & El-Sayed, M. A. (2006). Calculated absorption and scattering properties of gold nanoparticles of different size, shape, and composition: applications in biological imaging and biomedicine. *J. Phys. Chem. B*, *110*(14), 7238-7248.

[24] Murphy, C. J., Sau, T. K., Gole, A. M., Orendorff, C. J., Gao, J., Gou, L., ... & Li, T. (2005). Anisotropic metal nanoparticles: synthesis, assembly, and optical applications.

[25] Nealon, G. L., Donnio, B., Greget, R., Kappler, J. P., Terazzi, E., & Gallani, J. L. (2012). Magnetism in gold nanoparticles. *Nanoscale*, *4*(17), 5244-5258.

[26] Viswanathan, B., & Scibioh, M. A. (2007). *Fuel cells: principles and applications*. CRC PressI Llc.

[27] Kumar, C. S., & Mohammad, F. (2011). Magnetic nanomaterials for hyperthermia-based therapy and controlled drug delivery. *Advanced drug delivery reviews*, *63*(9), 789-808.

[28] Yu, H. D., Regulacio, M. D., Ye, E., & Han, M. Y. (2013). Chemical routes to top-down nanofabrication. *Chemical Society Reviews*, *42*(14), 6006-6018.

[29] Teo, B. K., & Sun, X. H. (2006). From top-down to bottom-up to hybrid nanotechnologies: road to nanodevices. *Journal of cluster science*, *17*(4), 529-540.

[30] Maeda, H. (2010). Tumor-selective delivery of macromolecular drugs via the EPR effect: background and future prospects. *Bioconjugate chemistry*, *21*(5), 797-802.

[31] Perrault, S. D., Walkey, C., Jennings, T., Fischer, H. C., & Chan, W. C. (2009). Mediating tumor targeting efficiency of nanoparticles through design. *Nano letters*, *9*(5), 1909-1915.

[32] Hu, Z., Huo, F., Zhang, Y., Chen, C., Tu, K., Jiang, H., & Wang, L. Q. (2011). "Smart" nanocarriers: a new paradigm for tumor targeting drug delivery systems. *Drug Delivery Letters*, *1*(1), 67-84.

[33] Sinha, R., Kim, G. J., Nie, S., & Shin, D. M. (2006). Nanotechnology in cancer therapeutics: bioconjugated nanoparticles for drug delivery. *Molecular cancer therapeutics*, *5*(8), 1909-1917.

[34] Scarì, G., Porta, F., Fascio, U., Avvakumova, S., Dal Santo, V., De Simone, M., ... & Zaccaro, L. (2012). Gold nanoparticles capped by a GC-containing peptide functionalized with an RGD motif for integrin targeting. *Bioconjugate chemistry*, *23*(3), 340-349.

[35] Di Pietro, P., Strano, G., Zuccarello, L., & Satriano, C. (2016). Gold and silver nanoparticles for applications in theranostics. *Current Topics in Medicinal Chemistry*, *16*(27), 3069-3102.

[36] Dixit, V., Van den Bossche, J., Sherman, D. M., Thompson, D. H., & Andres, R. P. (2006). Synthesis and grafting of thioctic acid− PEG− folate conjugates onto Au nanoparticles for selective targeting of folate receptor-positive tumor cells. *Bioconjugate chemistry*, *17*(3), 603-609.

[37] Kasemo, B. (1998). Biological surface science. *Current Opinion in Solid State and Materials Science*, *3*(5), 451-459.

[38] Zhao, F., Zhao, Y., Liu, Y., Chang, X., Chen, C., & Zhao, Y. (2011). Cellular uptake, intracellular trafficking, and cytotoxicity of nanomaterials. *Small*, *7*(10), 1322-1337.

[39] Tenzer, S., Docter, D., Rosfa, S., Wlodarski, A., Kuharev, J., Rekik, A., ... & Sirirattanapan, J. (2011). Nanoparticle size is a critical physicochemical determinant of the human blood plasma corona: a comprehensive quantitative proteomic analysis. *ACS nano*, *5*(9), 7155-7167.

[40] Arvizo, R. R., Rana, S., Miranda, O. R., Bhattacharya, R., Rotello, V. M., & Mukherjee, P. (2011). Mechanism of anti-angiogenic property of gold nanoparticles: role of nanoparticle size and surface charge. *Nanomedicine: Nanotechnology, Biology and Medicine*, *7*(5), 580-587.

[41] Yang, S. T., Liu, Y., Wang, Y. W., & Cao, A. (2013). Biosafety and bioapplication of nanomaterials by designing protein–nanoparticle interactions. *Small*, *9*(9-10), 1635-1653.

[42] Albanese, A., Tang, P. S., & Chan, W. C. (2012). The effect of nanoparticle size, shape, and surface chemistry on biological systems. *Annual review of biomedical engineering*, *14*, 1-16.

[43] Duan, X., & Li, Y. (2013). Physicochemical characteristics of nanoparticles affect circulation, biodistribution, cellular internalization, and trafficking. *Small*, *9*(9-10), 1521-1532.

[44] De Souza, J. A., Hunt, B., Asirwa, F. C., Adebamowo, C., & Lopes, G. (2015). Global health equity: Cancer care outcome disparities in high-, middle-, and low-income countries. *Journal of Clinical Oncology*, *34*(1), 6-13.

[45] Lammers, T., Aime, S., Hennink, W. E., Storm, G., & Kiessling, F. (2011). Theranostic nanomedicine. *Accounts of chemical research*, *44*(10), 1029-1038.

[46] Kim, Y., Stolarska, M. A., & Othmer, H. G. (2011). The role of the microenvironment in tumor growth and invasion. *Progress in biophysics and molecular biology*, *106*(2), 353-379.

[47] Nussenbaum, F., & Herman, I. M. (2010). Tumor angiogenesis: insights and innovations. *Journal of oncology*, *2010*.

[48] Chung, A. S., & Ferrara, N. (2011). Developmental and pathological angiogenesis. *Annual review of cell and developmental biology*, *27*, 563-584.

[49] Naumov, G. N., Akslen, L. A., & Folkman, J. (2006). Role of angiogenesis in human tumor dormancy: animal models of the angiogenic switch. *Cell cycle*, *5*(16), 1779-1787.

[50] Shaked, Y., McAllister, S., Fainaru, O., & Almog, N. (2014). Tumor dormancy and the angiogenic switch: possible implications of bone marrow-derived cells. *Current pharmaceutical design*, *20*(30), 4920-4933.

[51] Naumov, G. N., Akslen, L. A., & Folkman, J. (2006). Role of angiogenesis in human tumor dormancy: animal models of the angiogenic switch. *Cell cycle*, *5*(16), 1779-1787.

[52] Francavilla, C., Maddaluno, L., & Cavallaro, U. (2009, October). The functional role of cell adhesion molecules in tumor angiogenesis. In *Seminars in cancer biology* (Vol. 19, No. 5, pp. 298-309). Academic Press.

[53] Desgrosellier, J. S., & Cheresh, D. A. (2010). Integrins in cancer: biological implications and therapeutic opportunities. *Nature Reviews Cancer*, *10*(1), 9-22.

[54] Francavilla, C., Maddaluno, L., & Cavallaro, U. (2009, October). The functional role of cell adhesion molecules in tumor angiogenesis. In *Seminars in cancer biology* (Vol. 19, No. 5, pp. 298-309). Academic Press.

[55] Saptarshi, S. R., Duschl, A., & Lopata, A. L. (2013). Interaction of nanoparticles with proteins: relation to bio-reactivity of the nanoparticle. *Journal of nanobiotechnology*, *11*(1), 26.

[56] Lacerda, S. H. D. P., Park, J. J., Meuse, C., Pristinski, D., Becker, M. L., Karim, A., & Douglas, J. F. (2009). Interaction of gold nanoparticles with common human blood proteins. *ACS nano*, *4*(1), 365-379.

[57] Shukla, R., Bansal, V., Chaudhary, M., Basu, A., Bhonde, R. R., & Sastry, M. (2005). Biocompatibility of gold nanoparticles and their endocytotic fate inside the cellular compartment: a microscopic overview. *Langmuir*, *21*(23), 10644-10654.

[58] Guarnieri, D., Sabella, S., Muscetti, O., Belli, V., Malvindi, M. A., Fusco, S., ... & Netti, P. A. (2014). Transport across the cell-membrane dictates nanoparticle fate and toxicity: a new paradigm in nanotoxicology. *Nanoscale*, *6*(17), 10264-10273.

[59] Sanchez, V. C., Jachak, A., Hurt, R. H., & Kane, A. B. (2011). Biological interactions of graphene-family nanomaterials: an interdisciplinary review. *Chemical research in toxicology*, *25*(1), 15-34.

[60] Mu, Q., Su, G., Li, L., Gilbertson, B. O., Yu, L. H., Zhang, Q., ... & Yan, B. (2012). Size-dependent cell uptake of protein-coated graphene oxide nanosheets. *ACS applied materials & interfaces*, *4*(4), 2259-2266.

[61] Kostarelos, K., & Novoselov, K. S. (2014). Exploring the interface of graphene and biology. *Science*, *344*(6181), 261-263.

[62] Li, J. J., Hartono, D., Ong, C. N., Bay, B. H., & Yung, L. Y. L. (2010). Autophagy and oxidative stress associated with gold nanoparticles. *Biomaterials*, *31*(23), 5996-6003.

[63] Pan, Y., Neuss, S., Leifert, A., Fischler, M., Wen, F., Simon, U., ... & Jahnen-Dechent, W. (2007). Size-dependent cytotoxicity of gold nanoparticles. *Small*, *3*(11), 1941-1949.

[64] Yen, H. J., Hsu, S. H., & Tsai, C. L. (2009). Cytotoxicity and immunological response of gold and silver nanoparticles of different sizes. *Small*, *5*(13), 1553-1561.

[65] Gurunathan, S., Han, J. W., Dayem, A. A., Eppakayala, V., & Kim, J. H. (2012). Oxidative stress-mediated antibacterial activity of graphene oxide and reduced graphene oxide in Pseudomonas aeruginosa. *Int J Nanomedicine*, *7*(5901), e14.

[66] Chowdhury, S. M., Lalwani, G., Zhang, K., Yang, J. Y., Neville, K., & Sitharaman, B. (2013). Cell specific cytotoxicity and uptake of graphene nanoribbons. *Biomaterials*, *34*(1), 283-293.

[67] Seabra, A. B., Paula, A. J., de Lima, R., Alves, O. L., & Duran, N. (2014). Nanotoxicity of graphene and graphene oxide. *Chemical research in toxicology*, *27*(2), 159-168.

[68] Sanchez, V. C., Jachak, A., Hurt, R. H., & Kane, A. B. (2011). Biological interactions of graphene-family nanomaterials: an interdisciplinary review. *Chemical research in toxicology*, *25*(1), 15-34.

[69] Akhavan, O., & Ghaderi, E. (2010). Toxicity of graphene and graphene oxide nanowalls against bacteria. *ACS nano*, *4*(10), 5731-5736.

[70] Li, N., Cheng, Y., Song, Q., Jiang, Z., Tang, M., & Cheng, G. (2014). Graphene meets biology. *Chinese science bulletin*, *59*(13), 1341-1354.

[71] Zhang, X., Yin, J., Peng, C., Hu, W., Zhu, Z., Li, W., ... & Huang, Q. (2011). Distribution and biocompatibility studies of graphene oxide in mice after intravenous administration. *carbon*, *49*(3), 986-995.

[72] Zhang, S., Yang, K., Feng, L., & Liu, Z. (2011). In vitro and in vivo behaviors of dextran functionalized graphene. *Carbon*, *49*(12), 4040-4049..

[73] Arvizo, R. R., Bhattacharyya, S., Kudgus, R. A., Giri, K., Bhattacharya, R., & Mukherjee, P. (2012). Intrinsic therapeutic applications of noble metal nanoparticles: past, present and future. *Chemical Society Reviews*, *41*(7), 2943-2970.

[74] Dreaden, E. C., Mackey, M. A., Huang, X., Kang, B., & El-Sayed, M. A. (2011). Beating cancer in multiple ways using nanogold. *Chemical Society Reviews*, *40*(7), 3391-3404.

[75] Franci, G., Falanga, A., Galdiero, S., Palomba, L., Rai, M., Morelli, G., & Galdiero, M. (2015). Silver nanoparticles as potential antibacterial agents. *Molecules*, *20*(5), 8856-8874.

[76] Pakiari, A. H., & Jamshidi, Z. (2007). Interaction of amino acids with gold and silver clusters. *The Journal of Physical Chemistry A*, *111*(20), 4391-4396.

[77] Deng, W., & Goldys, E. M. (2014). Chemical sensing with nanoparticles as optical reporters: from noble metal nanoparticles to quantum dots and upconverting nanoparticles. *Analyst*, *139*(21), 5321-5334.

[78] Tao, F. *RSC London Ed*, 2014.

[79] Zhang, Y., Huang, R., Zhu, X., Wang, L., & Wu, C. (2012). Synthesis, properties, and optical applications of noble metal nanoparticle-biomolecule conjugates. *Chinese Science Bulletin*, *57*(2), 238-246.

[80] Zhang, Z., Zhang, X., Xin, Z., Deng, M., Wen, Y., & Song, Y. (2011). Synthesis of monodisperse silver nanoparticles for ink-jet printed flexible electronics. *Nanotechnology*, *22*(42), 425601.

[81] Di Pietro, P., Strano, G., Zuccarello, L., & Satriano, C. (2016). Gold and silver nanoparticles for applications in theranostics. *Current Topics in Medicinal Chemistry*, *16*(27), 3069-3102.

[82] Adeyemi, O. S., & Sulaiman, F. A. (2015). Evaluation of metal nanoparticles for drug delivery systems. *Journal of biomedical research*, *29*(2), 145.

[83] (a) Larguinho, M., Canto, R., Cordeiro, M., Pedrosa, P., Fortuna, A., Vinhas, R., & Baptista, P. V. (2015). Gold nanoprobe-based non-crosslinking hybridization for molecular diagnostics. *Expert review of molecular diagnostics*, *15*(10), 1355-1368; (b) Majdalawieh, A., Kanan, M. C., El-Kadri, O., & Kanan, S. M. (2014). Recent advances in gold and silver nanoparticles: synthesis and applications. *Journal of nanoscience and nanotechnology*, *14*(7), 4757-4780.

[84] Benyettou, F., Rezgui, R., Ravaux, F., Jaber, T., Blumer, K., Jouiad, M., ... & Trabolsi, A. (2015). Synthesis of silver nanoparticles for the dual delivery of doxorubicin and alendronate to cancer cells. *Journal of Materials Chemistry B*, *3*(36), 7237-7245.

[85] Braun, G. B., Pallaoro, A., Wu, G., Missirlis, D., Zasadzinski, J. A., Tirrell, M., & Reich, N. O. (2009). Laser-activated gene silencing via gold nanoshell− siRNA conjugates. *Acs Nano*, *3*(7), 2007-2015.

[86] Chu, K. F., & Dupuy, D. E. (2014). Thermal ablation of tumours: biological mechanisms and advances in therapy. *Nature Reviews Cancer*, *14*(3), 199-208.

[87] Rai, P., Mallidi, S., Zheng, X., Rahmanzadeh, R., Mir, Y., Elrington, S., ... & Hasan, T. (2010). Development and applications of photo-triggered theranostic agents. *Advanced drug delivery reviews*, *62*(11), 1094-1124.

[88] He, F., Shen, Q., Jiang, H., Zhou, J., Cheng, J., Guo, D., ... & Chen, B. (2009). Rapid identification and high sensitive detection of cancer cells on the gold nanoparticle interface by combined contact angle and electrochemical measurements. *Talanta*, *77*(3), 1009-1014.

[89] Shang, L., & Dong, S. (2009). Sensitive detection of cysteine based on fluorescent silver clusters. *Biosensors and Bioelectronics*, *24*(6), 1569-1573.

[90] Ravindran, A., Mani, V., Chandrasekaran, N., & Mukherjee, A. (2011). Selective colorimetric sensing of cysteine in aqueous solutions using silver nanoparticles in the presence of Cr 3+. *Talanta*, *85*(1), 533-540.

[91] Huang, T., Nallathamby, P. D., Gillet, D., & Xu, X. H. N. (2007). Design and synthesis of single-nanoparticle optical biosensors for imaging and characterization of single receptor molecules on single living cells. *Analytical chemistry*, *79*(20), 7708-7718.

[92] Le Ru, E. C., Meyer, M., & Etchegoin, P. G. (2006). Proof of single-molecule sensitivity in surface enhanced Raman scattering (SERS) by means of a two-analyte technique. *The journal of physical chemistry B*, *110*(4), 1944-1948.

[93] Aslan, K., Gryczynski, I., Malicka, J., Matveeva, E., Lakowicz, J. R., & Geddes, C. D. (2005). Metal-enhanced fluorescence: an emerging tool in biotechnology. *Current Opinion in Biotechnology*, *16*(1), 55-62.

[94] Das, A., Zhao, J., Schatz, G. C., Sligar, S. G., & Van Duyne, R. P. (2009). Screening of type I and II drug binding to human cytochrome P450-3A4 in nanodiscs by localized surface plasmon resonance spectroscopy. *Analytical chemistry*, *81*(10), 3754-3759.

[95] Faraday, M. (1857). The Bakerian lecture: experimental relations of gold (and other metals) to light. *Philosophical Transactions of the Royal Society of London*, *147*, 145-181.

[96] Turkevich, J., Stevenson, P. C., & Hillier, J. (1951). A study of the nucleation and growth processes in the synthesis of colloidal gold. *Discussions of the Faraday Society*, *11*, 55-75.

[97] Kimling, J., Maier, M., Okenve, B., Kotaidis, V., Ballot, H., & Plech, A. (2006). Turkevich method for gold nanoparticle synthesis revisited. *The Journal of Physical Chemistry B*, *110*(32), 15700-15707.

[98] Wiley, B., Sun, Y., Mayers, B., & Xia, Y. (2005). Shape-controlled synthesis of metal nanostructures: the case of silver. *Chemistry–A European Journal*, *11*(2), 454-463.

[99] La Mer, V.K., Dinegar, R.H. (1950). Theory, Production and Mechanism of Formation of Monodispersed Hydrosols**.** *J. Am. Chem. Soc.,*72, 4847-4854.

[100] Pillai, Z. S., & Kamat, P. V. (2004). What factors control the size and shape of silver nanoparticles in the citrate ion reduction method?. *The Journal of Physical Chemistry B*, *108*(3), 945-951.

[101] Polte, J., Tuaev, X., Wuithschick, M., Fischer, A., Thuenemann, A. F., Rademann, K., ... & Emmerling, F. (2012). Formation mechanism of colloidal silver nanoparticles: analogies and differences to the growth of gold nanoparticles. *ACS nano*, *6*(7), 5791-5802.

[102] Pong, B. K., Elim, H. I., Chong, J. X., Ji, W., Trout, B. L., & Lee, J. Y. (2007). New insights on the nanoparticle growth mechanism in the citrate reduction of gold (III) salt: formation of the Au nanowire intermediate and its nonlinear optical properties. *The Journal of Physical Chemistry C*, *111*(17), 6281-6287.

[103] Oliveira, M. M., Ugarte, D., Zanchet, D., & Zarbin, A. J. (2005). Influence of synthetic parameters on the size, structure, and stability of dodecanethiol-stabilized silver nanoparticles. *Journal of colloid and interface science*, *292*(2), 429-435.

[104] Dong, X., Ji, X., Jing, J., Li, M., Li, J., & Yang, W. (2010). Synthesis of triangular silver nanoprisms by stepwise reduction of sodium borohydride and trisodium citrate. *The Journal of Physical Chemistry C*, *114*(5), 2070-2074.

[105] Perepichka, I. I., Mezour, M. A., Perepichka, D. F., & Lennox, R. B. (2014). High thermal stability of block copolymer-capped Au and Cu nanoparticles. *Chemical Communications*, *50*(80), 11919-11921.

[106] Pal, N. K., & Kryschi, C. (2015). A facile one-pot synthesis of blue and red luminescent thiol stabilized gold nanoclusters: a thorough optical and microscopy study. *Physical Chemistry Chemical Physics*, *17*(33), 21423-21431.

[107] Bönnemann, H., Braun, G., Brijoux, W., Brinkmann, R., Tilling, A. S., Seevogel, K., & Siepen, K. (1996). Nanoscale colloidal metals and alloys stabilized by solvents and surfactants Preparation and use as catalyst precursors. *Journal of Organometallic Chemistry*, *520*(1-2), 143-162.

[108] Yang, J., Lee, J. Y., & Ying, J. Y. (2011). Phase transfer and its applications in nanotechnology. *Chemical Society Reviews*, *40*(3), 1672-1696.

[109] (a) Ma, H., Yin, B., Wang, S., Jiao, Y., Pan, W., Huang, S., ... & Meng, F. (2004). Synthesis of silver and gold nanoparticles by a novel electrochemical method. *ChemPhysChem*, *5*(1), 68-75; (b) Salkar, R. A., Jeevanandam, P., Aruna, S. T., Koltypin, Y., & Gedanken, A. (1999). The sonochemical preparation of amorphous silver nanoparticles. *Journal of materials chemistry*, *9*(6), 1333-1335.

[110] Dong, H., Chen, Y. C., & Feldmann, C. (2015). Polyol synthesis of nanoparticles: status and options regarding metals, oxides, chalcogenides, and non-metal elements. *Green Chemistry*, *17*(8), 4107-4132.

[111] De Giglio, E., Cometa, S., Satriano, C., Sabbatini, L., & Zambonin, P. G. (2009). Electrosynthesis of hydrogel films on metal substrates for the development of coatings with tunable drug delivery performances. *Journal of Biomedical Materials Research Part A*, *88*(4), 1048-1057.

[112] Sato-Berrú, R., Redón, R., Vázquez-Olmos, A., & Saniger, J. M. (2009). Silver nanoparticles synthesized by direct photoreduction of metal salts. Application in surface-enhanced Raman spectroscopy. *Journal of Raman Spectroscopy*, *40*(4), 376-380.

[113] Soroushian, B., Lampre, I., Belloni, J., & Mostafavi, M. (2005). Radiolysis of silver ion solutions in ethylene glycol: solvated electron and radical scavenging yields. *Radiation Physics and Chemistry*, *72*(2), 111-118.

[114] Messina, E., D'Urso, L., Fazio, E., Satriano, C., Donato, M. G., D'Andrea, C., ... & Neri, F. (2012). Tuning the structural and optical properties of gold/silver nano-alloys prepared by laser ablation in liquids for optical limiting, ultra-sensitive spectroscopy, and optical trapping. *Journal of Quantitative Spectroscopy and Radiative Transfer*, *113*(18), 2490-2498.

[115] Iravani, S. (2011). Green synthesis of metal nanoparticles using plants. *Green Chemistry*, *13*(10), 2638-2650.

[116] Katz, E., & Willner, I. (2004). Integrated nanoparticle–biomolecule hybrid systems: synthesis, properties, and applications. *Angewandte Chemie International Edition*, *43*(45), 6042-6108.

[117] Li, H., & Rothberg, L. (2004). Colorimetric detection of DNA sequences based on electrostatic interactions with unmodified gold nanoparticles. *Proceedings of the National Academy of Sciences of the United States of America*, *101*(39), 14036-14039.

[118] Ravindran, A., Chandrasekaran, N., & Mukherjee, A. (2012). Studies on differential behavior of silver nanoparticles towards thiol containing amino acids. *Current Nanoscience*, *8*(1), 141-149.

[119] Niemeyer, C. M. (2001). Nanoparticles, proteins, and nucleic acids: biotechnology meets materials science. *Angewandte Chemie International Edition*, *40*(22), 4128-4158.

[120] (a) Satriano, C., Messina, G. M., Marino, C., Aiello, I., Conte, E., La Mendola, D., ... & Impellizzeri, G. (2010). Surface immobilization of fibronectin-derived PHSRN peptide on functionalized polymer films–Effects on fibroblast spreading. *Journal of colloid and interface science*, *341*(2), 232-239; (b) Satriano, C., Fragalà, M. E., Forte, G., Santoro, A. M., La Mendola, D., & Kasemo, B. (2012). Surface adsorption of fibronectin-

derived peptide fragments: the influence of electrostatics and hydrophobicity for endothelial cells adhesion. *Soft Matter*, *8*(1), 53-56.

[121] (a) Travaglia, A., Satriano, C., Giuffrida, M. L., La Mendola, D., Rampazzo, E., Prodi, L., & Rizzarelli, E. (2013). Electrostatically driven interaction of silica-supported lipid bilayer nanoplatforms and a nerve growth factor-mimicking peptide. *Soft Matter*, *9*(18), 4648-4654; (b) Satriano, C., Edvardsson, M., Ohlsson, G., Wang, G., Svedhem, S., & Kasemo, B. (2010). Plasma Oxidized Polyhydroxymethylsiloxane- A New Smooth Surface for Supported Lipid Bilayer Formation. *Langmuir*, *26*(8), 5715-5725.

[122] Satriano, C., Svedhem, S., & Kasemo, B. (2012). Well-defined lipid interfaces for protein adsorption studies. *Physical Chemistry Chemical Physics*, *14*(48), 16695-16698.

[123] Zhu, L., & Torchilin, V. P. (2013). Stimulus-responsive nanopreparations for tumor targeting. *Integrative Biology*, *5*(1), 96-107.

[124] Allen, S. J., Watson, J. J., Shoemark, D. K., Barua, N. U., & Patel, N. K. (2013). GDNF, NGF and BDNF as therapeutic options for neurodegeneration. *Pharmacology & therapeutics*, *138*(2), 155-175.

[125] Levi-Montalcini, R., & Hamburger, V. (1951). Selective growth stimulating effects of mouse sarcoma on the sensory and sympathetic nervous system of the chick embryo. *Journal of Experimental Zoology Part A: Ecological Genetics and Physiology*, *116*(2), 321-361.

[126] Levi-Montalcini, R., & Cohen, S. (1960). Effects of the extract of the mouse submaxillary salivary glands on the sympathetic system of mammals. *Annals of the New York Academy of Sciences*, *85*(1), 324-341.

[127] Woo, N. H., Teng, H. K., Siao, C. J., Chiaruttini, C., Pang, P. T., Milner, T. A., ... & Lu, B. (2005). Activation of p75NTR by proBDNF facilitates hippocampal long-term depression. *Nature neuroscience*, *8*(8), 1069-1077.

[128] Wiesmann, C., Ultsch, M. H., Bass, S. H., & de Vos, A. M. (1999). Crystal structure of nerve growth factor in complex with the ligand-binding domain of the TrkA receptor. *Nature*, *401*(6749), 184-188.

[129] Banfield, M. J., Naylor, R. L., Robertson, A. G., Allen, S. J., Dawbarn, D., & Brady, R. L. (2001). Specificity in Trk receptor: neurotrophin interactions: the crystal structure of TrkB-d5 in complex with neurotrophin-4/5. *Structure*, *9*(12), 1191-1199.

[130] Schramm, A., Schulte, J. H., Astrahantseff, K., Apostolov, O., van Limpt, V., Sieverts, H., ... & Eggert, A. (2005). Biological effects of TrkA and TrkB receptor signaling in neuroblastoma. *Cancer letters*, *228*(1), 143-153.

[131] Travaglia, A., Arena, G., Fattorusso, R., Isernia, C., La Mendola, D., Malgieri, G., ... & Rizzarelli, E. (2011). The Inorganic Perspective of Nerve

Growth Factor: Interactions of Cu2+ and Zn2+ with the N-Terminus Fragment of Nerve Growth Factor Encompassing the Recognition Domain of the TrkA Receptor. *Chemistry–A European Journal*, *17*(13), 3726-3738.

[132] Travaglia, A., La Mendola, D., Magrì, A., Nicoletti, V. G., Pietropaolo, A., & Rizzarelli, E. (2012). Copper, BDNF and Its N-terminal Domain: Inorganic Features and Biological Perspectives. *Chemistry–A European Journal*, *18*(49), 15618-15631.

[133] Forte, G., Travaglia, A., Magrì, A., Satriano, C., & La Mendola, D. (2014). Adsorption of NGF and BDNF derived peptides on gold surfaces. *Physical Chemistry Chemical Physics*, *16*(4), 1536-1544.

[134] Sfrazzetto, G. T., Satriano, C., Tomaselli, G. A., & Rizzarelli, E. (2016). Synthetic fluorescent probes to map metallostasis and intracellular fate of zinc and copper. *Coordination Chemistry Reviews*, *311*, 125-167.

[135] (a) Grubman, A., & White, A. R. (2014). Copper as a key regulator of cell signalling pathways. *Expert reviews in molecular medicine*, *16*, e11; (b) La Mendola, D., Giacomelli, C., & Rizzarelli, E. (2016). Intracellular bioinorganic chemistry and cross talk among different-omics. *Current Topics in Medicinal Chemistry*, *16*(27), 3103-3130..

[136] (a) Travaglia, A., Arena, G., Fattorusso, R., Isernia, C., La Mendola, D., Malgieri, G., ... & Rizzarelli, E. (2011). The Inorganic Perspective of Nerve Growth Factor: Interactions of Cu2+ and Zn2+ with the N-Terminus Fragment of Nerve Growth Factor Encompassing the Recognition Domain of the TrkA Receptor. *Chemistry–A European Journal*, *17*(13), 3726-3738; (b) Travaglia, A., La Mendola, D., Magrì, A., Nicoletti, V. G., Pietropaolo, A., & Rizzarelli, E. (2012). Copper, BDNF and Its N-terminal Domain: Inorganic Features and Biological Perspectives. *Chemistry–A European Journal*, *18*(49), 15618-15631.

[137] Travaglia, A., Pietropaolo, A., La Mendola, D., Nicoletti, V. G., & Rizzarelli, E. (2012). The inorganic perspectives of neurotrophins and Alzheimer's disease. *Journal of inorganic biochemistry*, *111*, 130-137.

[138] Satriano, C., Forte, G., Magrì, A., Di Pietro, P., Travaglia, A., Pandini, G., ... & La Mendola, D. (2016). Neurotrophin-mimicking peptides at the biointerface with gold respond to copper ion stimuli. *Physical Chemistry Chemical Physics*, *18*(44), 30595-30604.

[139] Sauerbrey, G. (1959). Verwendung von Schwingquarzen zur Wägung dünner Schichten und zur Mikrowägung. *Zeitschrift für physik*, *155*(2), 206-222..

[140] Vogt, B. D., Lin, E. K., Wu, W. L., & White, C. C. (2004). Effect of film thickness on the validity of the Sauerbrey equation for hydrated

polyelectrolyte films. *The Journal of Physical Chemistry B*, *108*(34), 12685-12690.

[141] Cho, N. J., Frank, C. W., Kasemo, B., & Höök, F. (2010). Quartz crystal microbalance with dissipation monitoring of supported lipid bilayers on various substrates. *nature protocols*, *5*(6), 1096-1106.

[142] Lee, H. S., Contarino, M., Umashankara, M., Schön, A., Freire, E., Smith, A. B., ... & Penn, L. S. (2010). Use of the quartz crystal microbalance to monitor ligand-induced conformational rearrangements in HIV-1 envelope protein gp120. *Analytical and bioanalytical chemistry*, *396*(3), 1143-1152.

[143] (a) Fytianos, K., Rodriguez-Lorenzo, L., Clift, M. J., Blank, F., Vanhecke, D., Von Garnier, C., ... & Rothen-Rutishauser, B. (2015). Uptake efficiency of surface modified gold nanoparticles does not correlate with functional changes and cytokine secretion in human dendritic cells in vitro. *Nanomedicine: Nanotechnology, Biology and Medicine*, *11*(3), 633-644; (b) Hofstetter, W., Sehr, H., Wild, M. D., Portenier, J., Gobrecht, J., & Hunziker, E. B. (2013). Modulation of human osteoblasts by metal surface chemistry. *Journal of Biomedical Materials Research Part A*, *101*(8), 2355-2364; (c) Tang, R., Moyano, D. F., Subramani, C., Yan, B., Jeoung, E., Tonga, G. Y., ... & Rotello, V. M. (2014). Rapid coating of surfaces with functionalized nanoparticles for regulation of cell behavior. *Advanced Materials*, *26*(20), 3310-3314.

[144] Bush, A. I., & Tanzi, R. E. (2008). Therapeutics for Alzheimer's disease based on the metal hypothesis. *Neurotherapeutics*, *5*(3), 421-432.

[145] Obianyo, O., & Ye, K. (2013). Novel small molecule activators of the Trk family of receptor tyrosine kinases. *Biochimica et Biophysica Acta (BBA)-Proteins and Proteomics*, *1834*(10), 2213-2218.

[146] Daneman, R. (2012). The blood–brain barrier in health and disease. *Annals of neurology*, *72*(5), 648-672.

[147] Liu, S., Agalliu, D., Yu, C., & Fisher, M. (2012). The role of pericytes in blood-brain barrier function and stroke. *Current pharmaceutical design*, *18*(25), 3653-3662.

[148] Cipolla, M. J. (2009). Control of cerebral blood flow.

[149] Banerjee, J., Shi, Y., & Azevedo, H. S. (2016). In vitro blood–brain barrier models for drug research: state-of-the-art and new perspectives on reconstituting these models on artificial basement membrane platforms. *Drug discovery today*, *21*(9), 1367-1386.

[150] Obermeier, B., Daneman, R., & Ransohoff, R. M. (2013). Development, maintenance and disruption of the blood-brain barrier. *Nature medicine*, *19*(12), 1584-1596.

[151] De Jong, W. H., & Borm, P. J. (2008). Drug delivery and nanoparticles: applications and hazards. *International journal of nanomedicine*, *3*(2), 133.

[152] (a) Goldsmith, M., Abramovitz, L., & Peer, D. (2014). Precision nanomedicine in neurodegenerative diseases. *ACS nano*, *8*(3), 1958-1965.; (b) Patel, T., Zhou, J., Piepmeier, J. M., & Saltzman, W. M. (2012). Polymeric nanoparticles for drug delivery to the central nervous system. *Advanced drug delivery reviews*, *64*(7), 701-705; (c) Kreuter, J. (1994). Drug targeting with nanoparticles. *European journal of drug metabolism and pharmacokinetics*, *19*(3), 253-256; (d) Kreuter, J. (2014). Drug delivery to the central nervous system by polymeric nanoparticles: what do we know?. *Advanced drug delivery reviews*, *71*, 2-14.

[153] (a) Gao, X., Qian, J., Zheng, S., Changyi, Y., Zhang, J., Ju, S., ... & Li, C. (2014). Overcoming the blood–brain barrier for delivering drugs into the brain by using adenosine receptor nanoagonist. *ACS nano*, *8*(4), 3678-3689; (b) Choi, C. H. J., Alabi, C. A., Webster, P., & Davis, M. E. (2010). Mechanism of active targeting in solid tumors with transferrin-containing gold nanoparticles. *Proceedings of the National Academy of Sciences*, *107*(3), 1235-1240.

[154] Wiley, D. T., Webster, P., Gale, A., & Davis, M. E. (2013). Transcytosis and brain uptake of transferrin-containing nanoparticles by tuning avidity to transferrin receptor. *Proceedings of the National Academy of Sciences*, *110*(21), 8662-8667.

[155] (a) Song, Q., Huang, M., Yao, L., Wang, X., Gu, X., Chen, J., ... & Rong, Z. (2014). Lipoprotein-based nanoparticles rescue the memory loss of mice with Alzheimer's disease by accelerating the clearance of amyloid-beta. *ACS nano*, *8*(3), 2345-2359; (b) Song, Q., Huang, M., Yao, L., Wang, X., Gu, X., Chen, J., ... & Rong, Z. (2014). Lipoprotein-based nanoparticles rescue the memory loss of mice with Alzheimer's disease by accelerating the clearance of amyloid-beta. *ACS nano*, *8*(3), 2345-2359.

[156] Koffie, R. M., Farrar, C. T., Saidi, L. J., William, C. M., Hyman, B. T., & Spires-Jones, T. L. (2011). Nanoparticles enhance brain delivery of blood–brain barrier-impermeable probes for in vivo optical and magnetic resonance imaging. *Proceedings of the National Academy of Sciences*, *108*(46), 18837-18842.

[157] Kong, S. D., Lee, J., Ramachandran, S., Eliceiri, B. P., Shubayev, V. I., Lal, R., & Jin, S. (2012). Magnetic targeting of nanoparticles across the intact blood–brain barrier. *Journal of controlled release*, *164*(1), 49-57..

[158] (a) Ashley, C. E., Carnes, E. C., Phillips, G. K., Padilla, D., Durfee, P. N., Brown, P. A., ... & Carroll, N. J. (2011). The targeted delivery of multicomponent cargos to cancer cells by nanoporous particle-supported

lipid bilayers. *Nature materials*, *10*(5), 389-397; (b) Irvine, D. J. (2011). Drug delivery: One nanoparticle, one kill. *Nature materials*, *10*(5), 342-343.

[159] Ashley, C. E., Carnes, E. C., Phillips, G. K., Padilla, D., Durfee, P. N., Brown, P. A., ... & Carroll, N. J. (2011). The targeted delivery of multicomponent cargos to cancer cells by nanoporous particle-supported lipid bilayers. *Nature materials*, *10*(5), 389-397.

[160] Torchilin, V. P. (2005). Recent advances with liposomes as pharmaceutical carriers. *Nature reviews Drug discovery*, *4*(2), 145-160.

[161] Zuccarello, L., Rampazzo, E., Petrizza, L., Prodi, L., & Satriano, C. (2016). The influence of fluorescent silica nanoparticle surface chemistry on the energy transfer processes with lipid bilayers. *RSC Advances*, *6*(58), 52674-52682.

[162] Travaglia, A., Satriano, C., Giuffrida, M. L., La Mendola, D., Rampazzo, E., Prodi, L., & Rizzarelli, E. (2013). Electrostatically driven interaction of silica-supported lipid bilayer nanoplatforms and a nerve growth factor-mimicking peptide. *Soft Matter*, *9*(18), 4648-4654.

[163] P. Di Pietro, N. Caporarello, C. D. Anfuso, G. Lupo, A. Magrì, D. La Mendola, C. Satriano. (2017) Lipid bilayer-mediated immobilisation of neurotrophin peptides on gold nanoparticles: a new multipotential therapeutic nanoplatform for CNS disorders. Submitted to *ChemComm*

[164] Turkevich, J., Stevenson, P. C., & Hillier, J. (1951). A study of the nucleation and growth processes in the synthesis of colloidal gold. *Discussions of the Faraday Society*, *11*, 55-75.

[165] Frens, G. (1973). Controlled nucleation for the regulation of the particle size in monodisperse gold suspensions. *Nature*, *241*(105), 20-22.

[166] dos Santos Guimarães, I., Daltoé, R. D., Herlinger, A. L., Madeira, K. P., Ladislau, T., Valadão, I. C., ... & Demuth, K. R. (2013). Conventional Cancer Treatment. *Cancer Treatment-Conventional and Innovative approaches*.

[167] Catania, A., Barrajón-Catalán, E., Nicolosi, S., Cicirata, F., & Micol, V. (2013). Immunoliposome encapsulation increases cytotoxic activity and selectivity of curcumin and resveratrol against HER2 overexpressing human breast cancer cells. *Breast cancer research and treatment*, *141*(1), 55-65.

[168] Satriano, C., Svedhem, S., & Kasemo, B. (2012). Well-defined lipid interfaces for protein adsorption studies. *Physical Chemistry Chemical Physics*, *14*(48), 16695-16698.

[169] Zhao, P., Li, N., & Astruc, D. (2013). State of the art in gold nanoparticle synthesis. *Coordination Chemistry Reviews*, *257*(3), 638-665.

[170] Forte, G., Travaglia, A., Magrì, A., Satriano, C., & La Mendola, D. (2014). Adsorption of NGF and BDNF derived peptides on gold surfaces. *Physical Chemistry Chemical Physics*, *16*(4), 1536-1544.

[171] Satriano, C., Forte, G., Magrì, A., Di Pietro, P., Travaglia, A., Pandini, G., ... & La Mendola, D. (2016). Neurotrophin-mimicking peptides at the biointerface with gold respond to copper ion stimuli. *Physical Chemistry Chemical Physics*, *18*(44), 30595-30604.

[172] Satriano, C., Forte, G., Magrì, A., Di Pietro, P., Travaglia, A., Pandini, G., ... & La Mendola, D. (2016). Neurotrophin-mimicking peptides at the biointerface with gold respond to copper ion stimuli. *Physical Chemistry Chemical Physics*, *18*(44), 30595-30604.

[173] Ferrara, N., & Gerber, H. P. (1999). Vascular endothelial growth factor molecular and biological aspects. *Advances in Organ Biology*, *7*, 25-57.

[174] Ferrara, N., & Henzel, W. J. (1989). Pituitary follicular cells secrete a novel heparin-binding growth factor specific for vascular endothelial cells. *Biochemical and biophysical research communications*, *161*(2), 851-858.

[175] Germain, S., Monnot, C., Muller, L., & Eichmann, A. (2010). Hypoxia-driven angiogenesis: role of tip cells and extracellular matrix scaffolding. *Current opinion in hematology*, *17*(3), 245-251.

[176] Mandal, K., Uppalapati, M., Ault-Riché, D., Kenney, J., Lowitz, J., Sidhu, S. S., & Kent, S. B. (2012). Chemical synthesis and X-ray structure of a heterochiral {D-protein antagonist plus vascular endothelial growth factor} protein complex by racemic crystallography. *Proceedings of the National Academy of Sciences*, *109*(37), 14779-14784.

[177] Li, X., & Eriksson, U. (2001). Novel vegf family members: Vegf-b, vegf-c and vegf-d. *The international journal of biochemistry & cell biology*, *33*(4), 421-426.

[178] Tischer, E., Mitchell, R., Hartman, T., Silva, M., Gospodarowicz, D., Fiddes, J. C., & Abraham, J. A. (1991). The human gene for vascular endothelial growth factor. Multiple protein forms are encoded through alternative exon splicing. *Journal of Biological Chemistry*, *266*(18), 11947-11954.

[179] Houck, K. A., Ferrara, N., Winer, J., Cachianes, G., Li, B., & Leung, D. W. (1991). The vascular endothelial growth factor family: identification of a fourth molecular species and characterization of alternative splicing of RNA. *Molecular endocrinology*, *5*(12), 1806-1814.

[180] Houck, K. A., Leung, D. W., Rowland, A. M., Winer, J., & Ferrara, N. (1992). Dual regulation of vascular endothelial growth factor bioavailability

by genetic and proteolytic mechanisms. *Journal of Biological Chemistry*, *267*(36), 26031-26037.

[181] De Vries, C., & Escobedo, J. A. (1992). The fms-like tyrosine kinase, a receptor for vascular endothelial growth factor. *Science*, *255*(5047), 989.

[182] Waltenberger, J., Claesson-Welsh, L., Siegbahn, A., Shibuya, M., & Heldin, C. H. (1994). Different signal transduction properties of KDR and Flt1, two receptors for vascular endothelial growth factor. *Journal of Biological Chemistry*, *269*(43), 26988-26995.

[183] Zhong, H., & Phillip Bowen, J. (2011). Recent advances in small molecule inhibitors of VEGFR and EGFR signaling pathways. *Current topics in medicinal chemistry*, *11*(12), 1571-1590.

[184] Finetti, F., Basile, A., Capasso, D., Di Gaetano, S., Di Stasi, R., Pascale, M., ... & D'Andrea, L. D. (2012). Functional and pharmacological characterization of a VEGF mimetic peptide on reparative angiogenesis. *Biochemical pharmacology*, *84*(3), 303-311.

[185] Xie, H., & Kang, Y. J. (2009). Role of copper in angiogenesis and its medicinal implications. *Current medicinal chemistry*, *16*(10), 1304-1314.

[186] Feng, W., Ye, F., Xue, W., Zhou, Z., & Kang, Y. J. (2009). Copper regulation of hypoxia-inducible factor-1 activity. *Molecular pharmacology*, *75*(1), 174-182.

[187] Pan, Q., Kleer, C. G., Van Golen, K. L., Irani, J., Bottema, K. M., Bias, C., ... & Brewer, G. J. (2002). Copper deficiency induced by tetrathiomolybdate suppresses tumor growth and angiogenesis. *Cancer research*, *62*(17), 4854-4859.

[188] Grasso, G., Santoro, A. M., Magrì, A., La Mendola, D., Tomasello, M. F., Zimbone, S., & Rizzarelli, E. (2016). The Inorganic Perspective of VEGF: Interactions of Cu 2+ with Peptides Encompassing a Recognition Domain of the VEGF Receptor. *Journal of inorganic biochemistry*, *159*, 149-158.

[189] Arvizo, R. R., Rana, S., Miranda, O. R., Bhattacharya, R., Rotello, V. M., & Mukherjee, P. (2011). Mechanism of anti-angiogenic property of gold nanoparticles: role of nanoparticle size and surface charge. *Nanomedicine: Nanotechnology, Biology and Medicine*, *7*(5), 580-587.

[190] (a) Gurunathan, S., Lee, K. J., Kalishwaralal, K., Sheikpranbabu, S., Vaidyanathan, R., & Eom, S. H. (2009). Antiangiogenic properties of silver nanoparticles. *Biomaterials*, *30*(31), 6341-6350; (b) Sriram, M. I., Kanth, S. B. M., Kalishwaralal, K., & Gurunathan, S. (2010). Antitumor activity of silver nanoparticles in Dalton's lymphoma ascites tumor model. *Int J Nanomedicine*, *5*(1), 753-762.

[191] Bhattacharya, R., Mukherjee, P., Xiong, Z., Atala, A., Soker, S., & Mukhopadhyay, D. (2004). Gold nanoparticles inhibit VEGF165-induced proliferation of HUVEC cells. *Nano Letters*, *4*(12), 2479-2481.

[192] Semenov, A., Spatz, J. P., Möller, M., Lehn, J. M., Sell, B., Schubert, D., ... & Schubert, U. S. (1999). Controlled arrangement of supramolecular metal coordination arrays on surfaces. *Angewandte Chemie International Edition*, *38*(17), 2547-2550.

[193] Hu, Z., & Ritzdorf, T. (2006). Superconformal electrochemical deposition of gold for metallization in microelectronic devices. *Journal of The Electrochemical Society*, *153*(7), C467-C471.

[194] Zhong, C. J., & Porter, M. D. (1994). Evidence for carbon-sulfur bond cleavage in spontaneously adsorbed organosulfide-based monolayers at gold. *Journal of the American chemical society*, *116*(25), 11616-11617.

[195] Castner, D. G., Hinds, K., & Grainger, D. W. (1996). X-ray photoelectron spectroscopy sulfur 2p study of organic thiol and disulfide binding interactions with gold surfaces. *Langmuir*, *12*(21), 5083-5086.

[196] Stadtman, E. R., Van Remmen, H., Richardson, A., Wehr, N. B., & Levine, R. L. (2005). Methionine oxidation and aging. *Biochimica et Biophysica Acta (BBA)-Proteins and Proteomics*, *1703*(2), 135-140.

[197] (a) Jimenez, A. M. J., Rodrigo, M. A. M., Milosavljevic, V., Krizkova, S., Kopel, P., Heger, Z., & Adam, V. (2017). Gold nanoparticles-modified nanomaghemite and quantum dots-based hybridization assay for detection of HPV. *Sensors and Actuators B: Chemical*, *240*, 503-510.; (b) Frasconi, M., Marotta, R., Markey, L., Flavin, K., Spampinato, V., Ceccone, G., ... & Giordani, S. (2015). Multi-Functionalized Carbon Nano-onions as Imaging Probes for Cancer Cells. *Chemistry–A European Journal*, *21*(52), 19071-19080.

[198] Eriksson, L., Byrne, T., Johansson, E., Trygg, J., & Vikström, C. (2013). *Multi-and megavariate data analysis basic principles and applications*. Umetrics Academy.

[199] Marelli, U. K., Rechenmacher, F., Sobahi, T. R. A., Mas-Moruno, C., & Kessler, H. (2013). Tumor targeting via integrin ligands.

[200] Marelli, U. K., Rechenmacher, F., Sobahi, T. R. A., Mas-Moruno, C., & Kessler, H. (2013). Tumor targeting via integrin ligands.

[201] Humphries, J. D., Byron, A., & Humphries, M. J. (2006). Integrin ligands at a glance. *Journal of cell science*, *119*(19), 3901-3903.

[202] Avraamides, C. J., Garmy-Susini, B., & Varner, J. A. (2008). Integrins in angiogenesis and lymphangiogenesis. *Nature Reviews Cancer*, *8*(8), 604-617.

[203] Sillerud, L. O., & Larson, R. S. (2005). Design and structure of peptide and peptidomimetic antagonists of protein-protein interaction. *Current Protein and Peptide Science*, *6*(2), 151-169.

[204] (a) Barczyk, M., Carracedo, S., & Gullberg, D. (2010). At-a-glance article. *Cell Tissue Res*, *339*, 269-280. (b) Giancotti, F. G., & Ruoslahti, E. (1999). Integrin signaling. *Science*, *285*(5430), 1028-1033.

[205] Giancotti, F. G., & Ruoslahti, E. (1999). Integrin signaling. *Science*, *285*(5430), 1028-1033.

[206] Desgrosellier, J. S., & Cheresh, D. A. (2010). Integrins in cancer: biological implications and therapeutic opportunities. *Nature Reviews Cancer*, *10*(1), 9-22.

[207] Pfaff, M., Tangemann, K., Müller, B., Gurrath, M., Müller, G., Kessler, H., ... & Engel, J. (1994). Selective recognition of cyclic RGD peptides of NMR defined conformation by alpha IIb beta 3, alpha V beta 3, and alpha 5 beta 1 integrins. *Journal of Biological Chemistry*, *269*(32), 20233-20238.

[208] Sheldrake, H. M., & Patterson, L. H. (2009). Function and Antagonism of β. *Current cancer drug targets*, *9*(4), 519-540.

[209] Desgrosellier, J. S., & Cheresh, D. A. (2010). Integrins in cancer: biological implications and therapeutic opportunities. *Nature Reviews Cancer*, *10*(1), 9-22.

[210] Ruoslahti, E., & Pierschbacher, M. D. (1987). New perspectives in cell adhesion: RGD and integrins. *Science*, *238*(4826), 491-498.

[211] Sheldrake, H. M., & Patterson, L. H. (2014). Strategies To Inhibit Tumor Associated Integrin Receptors: Rationale for Dual and Multi-Antagonists: Miniperspective. *Journal of medicinal chemistry*, *57*(15), 6301-6315.

[212] (a) Shannon, K. E., Keene, J. L., Settle, S. L., Duffin, T. D., Nickols, M. A., Westlin, M., ... & Griggs, D. W. (2004). Anti-metastatic properties of RGD-peptidomimetic agents S137 and S247. *Clinical & experimental metastasis*, *21*(2), 129-138. (b) Liu, S. (2006). Radiolabeled multimeric cyclic RGD peptides as integrin αvβ3 targeted radiotracers for tumor imaging. *Molecular pharmaceutics*, *3*(5), 472-487.

[213] Kang, B., Mackey, M. A., & El-Sayed, M. A. (2010). Nuclear targeting of gold nanoparticles in cancer cells induces DNA damage, causing cytokinesis arrest and apoptosis. *Journal of the American Chemical Society*, *132*(5), 1517-1519.

[214] Krpetic, Z., Nativo, P., Porta, F., & Brust, M. (2009). A multidentate peptide for stabilization and facile bioconjugation of gold nanoparticles. *Bioconjugate chemistry*, *20*(3), 619-624.

[215] Sharma, H., Mishra, P. K., Talegaonkar, S., & Vaidya, B. (2015). Metal nanoparticles: a theranostic nanotool against cancer. *Drug Discovery Today*, *20*(9), 1143-1151.

[216] Lee, K. S., & El-Sayed, M. A. (2006). Gold and silver nanoparticles in sensing and imaging: sensitivity of plasmon response to size, shape, and metal composition. *The Journal of Physical Chemistry B*, *110*(39), 19220-19225.

[217] Dastjerdi, R., & Montazer, M. (2010). A review on the application of inorganic nano-structured materials in the modification of textiles: focus on anti-microbial properties. *Colloids and Surfaces B: Biointerfaces*, *79*(1), 5-18.

[218] Rai, M., Yadav, A., & Gade, A. (2009). Silver nanoparticles as a new generation of antimicrobials. *Biotechnology advances*, *27*(1), 76-83.

[219] Patra, C. R., Mukherjee, S., & Kotcherlakota, R. (2014). Biosynthesized silver nanoparticles: a step forward for cancer theranostics?. *Nanomedicine*, *9*(10), 1445-1448.

[220] Austin, L. A., Kang, B., Yen, C. W., & El-Sayed, M. A. (2011). Plasmonic imaging of human oral cancer cell communities during programmed cell death by nuclear-targeting silver nanoparticles. *Journal of the American Chemical Society*, *133*(44), 17594-17597.

[221] Sun, S., Zhou, C., Chen, S., Liu, J., Yu, J., Chilek, J., ... & Zheng, J. (2014). Surface-Chemistry Effect on Cellular Response of Luminescent Plasmonic Silver Nanoparticles. *Bioconjugate chemistry*, *25*(3), 453-459.

[222] Kalishwaralal, K., BarathManiKanth, S., Pandian, S. R. K., Deepak, V., & Gurunathan, S. (2010). Silver nano—a trove for retinal therapies. *Journal of Controlled Release*, *145*(2), 76-90.

[223] Di Pietro, P., Zaccaro, L., Comegna, D., Del Gatto, A., Saviano, M., Snyders, R., ... & Rizzarelli, E. (2016). Silver nanoparticles functionalized with a fluorescent cyclic RGD peptide: a versatile integrin targeting platform for cells and bacteria. *RSC Advances*, *6*(113), 112381-112392.

[224] Mulfinger, L., Solomon, S. D., Bahadory, M., Jeyarajasingam, A. V., Rutkowsky, S. A., & Boritz, C. (2007). Synthesis and study of silver nanoparticles. *J. Chem. Educ*, *84*(2), 322.

[225] Zitzmann, S., Ehemann, V., & Schwab, M. (2002). Arginine-glycine-aspartic acid (RGD)-peptide binds to both tumor and tumor-endothelial cells in vivo. *Cancer research*, *62*(18), 5139-5143.

[226] Choi, E. H., Rettig, W. J., Wayner, E. A., Srour, M. L., & Clegg, D. O. (1994). Functional identification of integrin laminin receptors that mediate process outgrowth by human SY5Y neuroblastoma cells. *Journal of neuroscience research*, *37*(4), 475-488; (b) Venkatasubramaniam, A., Drude, A., & Good, T. (2014). Role of N-terminal residues in Aβ interactions with integrin receptor and cell surface. *Biochimica et Biophysica Acta (BBA)-Biomembranes*, *1838*(10), 2568-2577.

[227] Ruoslahti, E. (1996). Integrin signaling and matrix assembly. *Tumor biology*, *17*(2), 117-124.

[228] Hauck, C. R., Agerer, F., Muenzner, P., & Schmitter, T. (2006). Cellular adhesion molecules as targets for bacterial infection. *European journal of cell biology*, *85*(3), 235-242.

[229] Cue, D., Southern, S. O., Southern, P. J., Prabhakar, J., Lorelli, W., Smallheer, J. M., ... & Cleary, P. P. (2000). A nonpetide integrin antagonist can inhibit epithelial cell ingestion of Streptococcus pyogenes by blocking formation of integrin α5β1-fibronectin-M1 protein complexes. *Proceedings of the National Academy of Sciences*, *97*(6), 2858-2863.

[230] Blystone, S. D., Graham, I. L., Lindberg, F. P., & Brown, E. J. (1994). Integrin Differentially Regulates Adhesive and Phagocytic Functions of the Fibronectin Receptor-s/l. *The Journal of Cell Biology*, *127*(4), 1129-1137.

[231] Guo, S., & Dong, S. (2011). Graphene nanosheet: synthesis, molecular engineering, thin film, hybrids, and energy and analytical applications. *Chemical Society Reviews*, *40*(5), 2644-2672.

[232] Zhu, Y., Murali, S., Cai, W., Li, X., Suk, J. W., Potts, J. R., & Ruoff, R. S. (2010). Graphene and graphene oxide: synthesis, properties, and applications. *Advanced materials*, *22*(35), 3906-3924.

[233] Rao, C. E. E., Sood, A. E., Subrahmanyam, K. E., & Govindaraj, A. (2009). Graphene: the new two-dimensional nanomaterial. *Angewandte Chemie International Edition*, *48*(42), 7752-7777.

[234] Novoselov, K. S., Geim, A. K., Morozov, S. V., Jiang, D., Zhang, Y., Dubonos, S. V., ... & Firsov, A. A. (2004). Electric field effect in atomically thin carbon films. *science*, *306*(5696), 666-669.

[235] Lotya, M., Hernandez, Y., King, P. J., Smith, R. J., Nicolosi, V., Karlsson, L. S., ... & Duesberg, G. S. (2009). Liquid phase production of graphene by exfoliation of graphite in surfactant/water solutions. *Journal of the American Chemical Society*, *131*(10), 3611-3620.

[236] Sun, Z., Yan, Z., Yao, J., Beitler, E., Zhu, Y., & Tour, J. M. (2010). Growth of graphene from solid carbon sources. *Nature*, *468*(7323), 549-552.

[237] Huang, X., Qi, X., Boey, F., & Zhang, H. (2012). Graphene-based composites. *Chemical Society Reviews*, *41*(2), 666-686.

[238] Shen, H., Zhang, L., Liu, M., & Zhang, Z. (2012). Biomedical applications of graphene. *Theranostics*, *2*(3), 283-294.

[239] Yang, W., Ratinac, K. R., Ringer, S. P., Thordarson, P., Gooding, J. J., & Braet, F. (2010). Carbon nanomaterials in biosensors: should you use nanotubes or graphene?. *Angewandte Chemie International Edition*, *49*(12), 2114-2138.

[240] Dreyer, D. R., Park, S., Bielawski, C. W., & Ruoff, R. S. (2010). The chemistry of graphene oxide. *Chemical Society Reviews*, *39*(1), 228-240.

[241] Yang, K., Feng, L., Shi, X., & Liu, Z. (2013). Nano-graphene in biomedicine: theranostic applications. *Chemical Society Reviews*, *42*(2), 530-547.

[242] Shen, H., Zhang, L., Liu, M., & Zhang, Z. (2012). Biomedical applications of graphene. *Theranostics*, *2*(3), 283-294.

[243] Cheon, Y. A., Bae, J. H., & Chung, B. G. (2016). Reduced graphene oxide nanosheet for chemo-photothermal therapy. *Langmuir*, *32*(11), 2731-2736.

[244] Wei, Y., Zhou, F., Zhang, D., Chen, Q., & Xing, D. (2016). A graphene oxide based smart drug delivery system for tumor mitochondria-targeting photodynamic therapy. *Nanoscale*, *8*(6), 3530-3538.

[245] Chung, C., Kim, Y. K., Shin, D., Ryoo, S. R., Hong, B. H., & Min, D. H. (2013). Biomedical applications of graphene and graphene oxide. *Accounts of chemical research*, *46*(10), 2211-2224.

[246] Lee, J., Kim, J., Kim, S., & Min, D. H. (2016). Biosensors based on graphene oxide and its biomedical application. *Advanced drug delivery reviews*, *105*, 275-287.

[247] Sun, X., Fan, J., Zhang, Y., Chen, H., Zhao, Y., & Xiao, J. (2016). A graphene oxide-based FRET sensor for rapid and specific detection of unfolded collagen fragments. *Biosensors and Bioelectronics*, *79*, 15-21.

[248] (a) Cohen-Karni, T., Qing, Q., Li, Q., Fang, Y., & Lieber, C. M. (2010). Graphene and nanowire transistors for cellular interfaces and electrical recording. *Nano letters*, *10*(3), 1098-1102. (b) Hess, L. H., Jansen, M., Maybeck, V., Hauf, M. V., Seifert, M., Stutzmann, M., ... & Garrido, J. A. (2011). Graphene transistor arrays for recording action potentials from electrogenic cells. *Advanced Materials*, *23*(43), 5045-5049.

[249] Xie, L., Ling, X., Fang, Y., Zhang, J., & Liu, Z. (2009). Graphene as a substrate to suppress fluorescence in resonance Raman spectroscopy. *Journal of the American Chemical Society*, *131*(29), 9890-9891.

[250] Zhang, J., Dong, X., Cheng, J., Li, J., & Wang, Y. (2011). Efficient analysis of non-polar environmental contaminants by MALDI-TOF MS with graphene as matrix. *Journal of the American Society for Mass Spectrometry*, *22*(7), 1294-1298.

[251] Brodie, B. C. (1859). On the atomic weight of graphite. *Philosophical Transactions of the Royal Society of London*, *149*, 249-259.

[252] Staudenmaier, L. (1898). Verfahren zur darstellung der graphitsäure. *European Journal of Inorganic Chemistry*, *31*(2), 1481-1487.

[253] Hummers, W.S. and Offeman, R. E. (1958) Preparation of Graphene Oxide. *J. Am. Chem. Soc., 80*, 1339.

[254] Guerrero-Contreras, J., & Caballero-Briones, F. (2015). Graphene oxide powders with different oxidation degree, prepared by synthesis variations of the Hummers method. *Materials Chemistry and Physics*, *153*, 209-220.

[255] McAllister, M. J., Li, J. L., Adamson, D. H., Schniepp, H. C., Abdala, A. A., Liu, J., ... & Aksay, I. A. (2007). Single sheet functionalized graphene by oxidation and thermal expansion of graphite. *Chemistry of materials*, *19*(18), 4396-4404.

[256] Kim, J., Cote, L. J., Kim, F., Yuan, W., Shull, K. R., & Huang, J. (2010). Graphene oxide sheets at interfaces. *Journal of the American Chemical Society*, *132*(23), 8180-8186.

[257] Karlicky, F., Kumara Ramanatha Datta, K., Otyepka, M., & Zboril, R. (2013). Halogenated graphenes: rapidly growing family of graphene derivatives. *ACS nano*, *7*(8), 6434-6464.

[258] Bagri, A., Mattevi, C., Acik, M., Chabal, Y. J., Chhowalla, M., & Shenoy, V. B. (2010). Structural evolution during the reduction of chemically derived graphene oxide. *Nature chemistry*, *2*(7), 581-587.

[259] Stankovich, S., Dikin, D. A., Piner, R. D., Kohlhaas, K. A., Kleinhammes, A., Jia, Y., ... & Ruoff, R. S. (2007). Synthesis of graphene-based nanosheets via chemical reduction of exfoliated graphite oxide. *carbon*, *45*(7), 1558-1565.

[260] Shin, H. J., Kim, K. K., Benayad, A., Yoon, S. M., Park, H. K., Jung, I. S., ... & Lee, Y. H. (2009). Efficient reduction of graphite oxide by sodium borohydride and its effect on electrical conductance. *Advanced Functional Materials*, *19*(12), 1987-1992.

[261] Kang, S. J., Kocabas, C., Ozel, T., Shim, M., Pimparkar, N., Alam, M. A., ... & Rogers, J. A. (2007). High-performance electronics using dense, perfectly aligned arrays of single-walled carbon nanotubes. *Nature nanotechnology*, *2*(4), 230-236.

[262] Ambrosi, A., Chua, C. K., Bonanni, A., & Pumera, M. (2012). Lithium aluminum hydride as reducing agent for chemically reduced graphene oxides. *Chemistry of Materials*, *24*(12), 2292-2298.

[263] Wang, G., Yang, J., Park, J., Gou, X., Wang, B., Liu, H., & Yao, J. (2008). Facile synthesis and characterization of graphene nanosheets. *The Journal of Physical Chemistry C*, *112*(22), 8192-8195.

[264]Wu, Z. S., Ren, W., Gao, L., Liu, B., Jiang, C., & Cheng, H. M. (2009). Synthesis of high-quality graphene with a pre-determined number of layers. *Carbon*, *47*(2), 493-499.

[265] Fan, X., Peng, W., Li, Y., Li, X., Wang, S., Zhang, G., & Zhang, F. (2008). Deoxygenation of exfoliated graphite oxide under alkaline conditions: a green route to graphene preparation. *Advanced Materials*, *20*(23), 4490-4493.

[266] Gao, W., Majumder, M., Alemany, L. B., Narayanan, T. N., Ibarra, M. A., Pradhan, B. K., & Ajayan, P. M. (2011). Engineered graphite oxide materials for application in water purification. *ACS applied materials & interfaces*, *3*(6), 1821-1826.

[267] (a) Dua, V., Surwade, S. P., Ammu, S., Agnihotra, S. R., Jain, S., Roberts, K. E., ... & Manohar, S. K. (2010). All-organic vapor sensor using inkjet-printed reduced graphene oxide. *Angewandte Chemie International Edition*, *49*(12), 2154-2157. (b) Fernández-Merino, M. J., Guardia, L., Paredes, J. I., Villar-Rodil, S., Solís-Fernández, P., Martínez-Alonso, A., & Tascón, J. M. D. (2010). Vitamin C is an ideal substitute for hydrazine in the reduction of graphene oxide suspensions. *The Journal of Physical Chemistry C*, *114*(14), 6426-6432.

[268] Liu, J., Fu, S., Yuan, B., Li, Y., & Deng, Z. (2010). Toward a universal "adhesive nanosheet" for the assembly of multiple nanoparticles based on a protein-induced reduction/decoration of graphene oxide. *Journal of the American Chemical Society*, *132*(21), 7279-7281.

[269] Salas, E. C., Sun, Z., Lüttge, A., & Tour, J. M. (2010). Reduction of graphene oxide via bacterial respiration. *AcS Nano*, *4*(8), 4852-4856.

[270] Zhou, M., Wang, Y., Zhai, Y., Zhai, J., Ren, W., Wang, F., & Dong, S. (2009). Controlled synthesis of large-area and patterned electrochemically reduced graphene oxide films. *Chemistry–A European Journal*, *15*(25), 6116-6120.

[271] (a) McAllister, M. J., Li, J. L., Adamson, D. H., Schniepp, H. C., Abdala, A. A., Liu, J., ... & Aksay, I. A. (2007). Single sheet functionalized graphene by oxidation and thermal expansion of graphite. *Chemistry of materials*, *19*(18), 4396-4404. (b) Chen, X., Meng, D., Wang, B., Li, B. W.,

Li, W., Bielawski, C. W., & Ruoff, R. S. (2016). Rapid thermal decomposition of confined graphene oxide films in air. *Carbon*, *101*, 71-76.

[272] Park, S., Dikin, D. A., Nguyen, S. T., & Ruoff, R. S. (2009). Graphene oxide sheets chemically cross-linked by polyallylamine. *The Journal of Physical Chemistry C*, *113*(36), 15801-15804.

[273] Abdelsayed, V., Moussa, S., Hassan, H. M., Aluri, H. S., Collinson, M. M., & El-Shall, M. S. (2010). Photothermal deoxygenation of graphite oxide with laser excitation in solution and graphene-aided increase in water temperature. *The Journal of Physical Chemistry Letters*, *1*(19), 2804-2809.

[274] Vinodgopal, K., Neppolian, B., Lightcap, I. V., Grieser, F., Ashokkumar, M., & Kamat, P. V. (2010). Sonolytic design of graphene− Au nanocomposites. simultaneous and sequential reduction of graphene oxide and Au (III). *The Journal of Physical Chemistry Letters*, *1*(13), 1987-1993.

[275] Hassan, H. M., Abdelsayed, V., Abd El Rahman, S. K., AbouZeid, K. M., Terner, J., El-Shall, M. S., ... & El-Azhary, A. A. (2009). Microwave synthesis of graphene sheets supporting metal nanocrystals in aqueous and organic media. *Journal of Materials Chemistry*, *19*(23), 3832-3837.

[276] Ding, Y. H., Zhang, P., Zhuo, Q., Ren, H. M., Yang, Z. M., & Jiang, Y. (2011). A green approach to the synthesis of reduced graphene oxide nanosheets under UV irradiation. *Nanotechnology*, *22*(21), 215601.

[277] Compagnini, G., Russo, P., Tomarchio, F., Puglisi, O., D'Urso, L., & Scalese, S. (2012). Laser assisted green synthesis of free standing reduced graphene oxides at the water–air interface. *Nanotechnology*, *23*(50), 505601.

[278] S. Park and R. S. Ruoff, Chemical methods for the production of graphenes. Nat. Nanotechnol., 2009, 4, 217.

[279] (a) Liu, Z., Cai, W., He, L., Nakayama, N., Chen, K., Sun, X., ... & Dai, H. (2007). In vivo biodistribution and highly efficient tumour targeting of carbon nanotubes in mice. *Nature nanotechnology*, *2*(1), 47-52. (b) Yang, K., Wan, J., Zhang, S., Zhang, Y., Lee, S. T., & Liu, Z. (2010). In vivo pharmacokinetics, long-term biodistribution, and toxicology of PEGylated graphene in mice. *ACS nano*, *5*(1), 516-522.

[280] Wang, B., Yang, D., Zhang, J. Z., Xi, C., & Hu, J. (2011). Stimuli-responsive polymer covalent functionalization of graphene oxide by Ce (IV)-induced redox polymerization. *The Journal of Physical Chemistry C*, *115*(50), 24636-24641.

[281] Hsiao, M. C., Liao, S. H., Yen, M. Y., Liu, P. I., Pu, N. W., Wang, C. A., & Ma, C. C. M. (2010). Preparation of covalently functionalized graphene using residual oxygen-containing functional groups. *ACS applied materials & interfaces*, *2*(11), 3092-3099.

[282] Shan, C., Yang, H., Han, D., Zhang, Q., Ivaska, A., & Niu, L. (2009). Water-soluble graphene covalently functionalized by biocompatible poly-L-lysine. *Langmuir*, *25*(20), 12030-12033.

[283] Sun, S., Cao, Y., Feng, J., & Wu, P. (2010). Click chemistry as a route for the immobilization of well-defined polystyrene onto graphene sheets. *Journal of Materials Chemistry*, *20*(27), 5605-5607.

[284] (a) Karousis, N., Sandanayaka, A. S., Hasobe, T., Economopoulos, S. P., Sarantopoulou, E., & Tagmatarchis, N. (2011). Graphene oxide with covalently linked porphyrin antennae: Synthesis, characterization and photophysical properties. *Journal of Materials Chemistry*, *21*(1), 109-117. (b) Zhang, X., Feng, Y., Huang, D., Li, Y., & Feng, W. (2010). Investigation of optical modulated conductance effects based on a graphene oxide–azobenzene hybrid. *Carbon*, *48*(11), 3236-3241.

[285] Yang, K., Wan, J., Zhang, S., Tian, B., Zhang, Y., & Liu, Z. (2012). The influence of surface chemistry and size of nanoscale graphene oxide on photothermal therapy of cancer using ultra-low laser power. *Biomaterials*, *33*(7), 2206-2214.

[286] Feng, L., Zhang, S., & Liu, Z. (2011). Graphene based gene transfection. *Nanoscale*, *3*(3), 1252-1257.

[287] Depan, D., Shah, J., & Misra, R. D. K. (2011). Controlled release of drug from folate-decorated and graphene mediated drug delivery system: synthesis, loading efficiency, and drug release response. *Materials Science and Engineering: C*, *31*(7), 1305-1312.

[288] Hatamie, S., Akhavan, O., Sadrnezhaad, S. K., Ahadian, M. M., Shirolkar, M. M., & Wang, H. Q. (2015). Curcumin-reduced graphene oxide sheets and their effects on human breast cancer cells. *Materials Science and Engineering: C*, *55*, 482-489.

[289] Novoselov, K. S., Fal, V. I., Colombo, L., Gellert, P. R., Schwab, M. G., & Kim, K. (2012). A roadmap for graphene. *Nature*, *490*(7419), 192-200.

[290] Yang, K., Feng, L., Shi, X., & Liu, Z. (2013). Nano-graphene in biomedicine: theranostic applications. *Chemical Society Reviews*, *42*(2), 530-547.

[291] Wang, Z., Dong, Y., Li, H., Zhao, Z., Wu, H. B., Hao, C., ... & Lou, X. W. D. (2014). Enhancing lithium–sulphur battery performance by strongly binding the discharge products on amino-functionalized reduced graphene oxide. *Nature communications*, *5*.

[292] Fazaeli, Y., Akhavan, O., Rahighi, R., Aboudzadeh, M. R., Karimi, E., & Afarideh, H. (2014). In vivo SPECT imaging of tumors by 198,199 Au-

labeled graphene oxide nanostructures. *Materials Science and Engineering: C*, *45*, 196-204.

[293] Chaban, V. V., & Prezhdo, O. V. (2015). Synergistic amination of graphene: molecular dynamics and thermodynamics. *The journal of physical chemistry letters*, *6*(21), 4397-4403.

[294] Yi, P., & Chen, K. L. (2013). Interaction of multiwalled carbon nanotubes with supported lipid bilayers and vesicles as model biological membranes. *Environmental science & technology*, *47*(11), 5711-5719.

[295] Frost, R., Jönsson, G. E., Chakarov, D., Svedhem, S., & Kasemo, B. (2012). Graphene oxide and lipid membranes: interactions and nanocomposite structures. *Nano letters*, *12*(7), 3356-3362.

[296] Liu, X., & Chen, K. L. (2015). Interactions of graphene oxide with model cell membranes: probing nanoparticle attachment and lipid bilayer disruption. *Langmuir*, *31*(44), 12076-12086.

[297] Plunkett, P., Camley, B. A., Weirich, K. L., Israelachvili, J., & Atzberger, P. J. (2013). Simulation of edge facilitated adsorption and critical concentration induced rupture of vesicles at a surface. *Soft Matter*, *9*(35), 8420-8427.

[298] (a) Brian, A.A., McConnell, H.M. (1984) Allogeneic stimulation of cytotoxic T cells by supported planar membranes. *PNAS, 81,* 6159–6163. (b) McConnell, H. M., Watts, T. H., Weis, R. M., & Brian, A. A. (1986). Supported planar membranes in studies of cell-cell recognition in the immune system. *Biochimica et Biophysica Acta (BBA)-Reviews on Biomembranes*, *864*(1), 95-106.

[299] (a) Tien, H. T., & Salamon, Z. (1989). Formation of self-assembled lipid bilayers on solid substrates. *Journal of electroanalytical chemistry and interfacial electrochemistry*, *276*(3), 211-218. (b) Kalb, E., Frey, S., & Tamm, L. K. (1992). Formation of supported planar bilayers by fusion of vesicles to supported phospholipid monolayers. *Biochimica et Biophysica Acta (BBA)-Biomembranes*, *1103*(2), 307-316.

[300] Tero, R. (2012). Substrate effects on the formation process, structure and physicochemical properties of supported lipid bilayers. *Materials*, *5*(12), 2658-2680.

[301] (a) Reimhult, E., Höök, F., & Kasemo, B. (2002). Vesicle adsorption on SiO 2 and TiO 2: dependence on vesicle size. *The Journal of chemical physics*, *117*(16), 7401-7404. (b) Reimhult, E., Höök, F., & Kasemo, B. (2003). Intact vesicle adsorption and supported biomembrane formation from vesicles in solution: influence of surface chemistry, vesicle size, temperature, and osmotic pressure. *Langmuir*, *19*(5), 1681-1691.

[302] Satriano, C., Edvardsson, M., Ohlsson, G., Wang, G., Svedhem, S., & Kasemo, B. (2010). Plasma Oxidized Polyhydroxymethylsiloxane A New Smooth Surface for Supported Lipid Bilayer Formation. *Langmuir*, *26*(8), 5715-5725.

[303] Ratto, T. V., & Longo, M. L. (2002). Obstructed diffusion in phase-separated supported lipid bilayers: a combined atomic force microscopy and fluorescence recovery after photobleaching approach. *Biophysical journal*, *83*(6), 3380-3392.

[304] (a) Reimhult, E., Höök, F., & Kasemo, B. (2003). Intact vesicle adsorption and supported biomembrane formation from vesicles in solution: influence of surface chemistry, vesicle size, temperature, and osmotic pressure. *Langmuir*, *19*(5), 1681-1691. (b) Jing, Y., Trefna, H., Persson, M., Kasemo, B., & Svedhem, S. (2014). Formation of supported lipid bilayers on silica: relation to lipid phase transition temperature and liposome size. *Soft Matter*, *10*(1), 187-195.

[305] (a) Keller, C. A., & Kasemo, B. (1998). Surface specific kinetics of lipid vesicle adsorption measured with a quartz crystal microbalance. *Biophysical journal*, *75*(3), 1397-1402. (b) Edvardsson, M., Svedhem, S., Wang, G., Richter, R., Rodahl, M., & Kasemo, B. (2008). QCM-D and reflectometry instrument: applications to supported lipid structures and their biomolecular interactions. *Analytical chemistry*, *81*(1), 349-361.

[306] Reimhult, E., Larsson, C., Kasemo, B., & Höök, F. (2004). Simultaneous surface plasmon resonance and quartz crystal microbalance with dissipation monitoring measurements of biomolecular adsorption events involving structural transformations and variations in coupled water. *Analytical chemistry*, *76*(24), 7211-7220.

[307] Striebel, C., Brecht, A., & Gauglitz, G. (1994). Characterization of biomembranes by spectral ellipsometry, surface plasmon resonance and interferometry with regard to biosensor application. *Biosensors and Bioelectronics*, *9*(2), 139-146.

[308] Jass, J., Tjärnhage, T., & Puu, G. (2000). From liposomes to supported, planar bilayer structures on hydrophilic and hydrophobic surfaces: an atomic force microscopy study. *Biophysical journal*, *79*(6), 3153-3163.

[309] Simons, K., & Gerl, M. J. (2010). Revitalizing membrane rafts: new tools and insights. *Nature reviews Molecular cell biology*, *11*(10), 688-699.

[310] Soumpasis, D. M. (1983). Theoretical analysis of fluorescence photobleaching recovery experiments. *Biophysical journal*, *41*(1), 95-97.

[311] Macháň, R., & Hof, M. (2010). Recent developments in fluorescence correlation spectroscopy for diffusion measurements in planar lipid membranes. *International journal of molecular sciences*, *11*(2), 427-457.

[312] Schmidt, T., Schütz, G. J., Baumgartner, W., Gruber, H. J., & Schindler, H. (1996). Imaging of single molecule diffusion. *Proceedings of the National Academy of Sciences*, *93*(7), 2926-2929.

[313] Axelrod, D., Koppel, D. E., Schlessinger, J., Elson, E., & Webb, W. W. (1976). Mobility measurement by analysis of fluorescence photobleaching recovery kinetics. *Biophysical journal*, *16*(9), 1055-1069.

[314] Raudino, A., Cambria, A., Sarpietro, M. G., & Satriano, C. (2000). Binding of lipid vesicles to protein-coated solid polymer surfaces: a model for cell adhesion to artificial biocompatible materials. *Journal of colloid and interface science*, *231*(1), 66-73.

[315] Frost, R., Jönsson, G. E., Chakarov, D., Svedhem, S., & Kasemo, B. (2012). Graphene oxide and lipid membranes: interactions and nanocomposite structures. *Nano letters*, *12*(7), 3356-3362.

[316] Wu, L., Zeng, L., & Jiang, X. (2015). Revealing the nature of interaction between graphene oxide and lipid membrane by surface-enhanced infrared absorption spectroscopy. *Journal of the American Chemical Society*, *137*(32), 10052-10055.

[317] Hatcher, H., Planalp, R., Cho, J., Torti, F. M., & Torti, S. V. (2008). Curcumin: from ancient medicine to current clinical trials. *Cellular and Molecular Life Sciences*, *65*(11), 1631-1652.

[318] (a) Lee, K. H., Aziz, F. H. A., Syahida, A., Abas, F., Shaari, K., Israf, D. A., & Lajis, N. H. (2009). Synthesis and biological evaluation of curcumin-like diarylpentanoid analogues for anti-inflammatory, antioxidant and anti-tyrosinase activities. *European journal of medicinal chemistry*, *44*(8), 3195-3200. (b) Prasad, S., Tyagi, A. K., & Aggarwal, B. B. (2014). Recent developments in delivery, bioavailability, absorption and metabolism of curcumin: the golden pigment from golden spice. *Cancer research and treatment: official journal of Korean Cancer Association*, *46*(1), 2-18.

[319] Sharma, R. A., Steward, W. P., & Gescher, A. J. (2007). Pharmacokinetics and pharmacodynamics of curcumin. In *The molecular targets and therapeutic uses of curcumin in health and disease* (pp. 453-470). Springer US.

[320] Rao, K. M., Rao, K. K., Ramanjaneyulu, G., & Ha, C. S. (2015). Curcumin encapsulated pH sensitive gelatin based interpenetrating polymeric network nanogels for anti cancer drug delivery. *International journal of pharmaceutics*, *478*(2), 788-795.

[321] (a) Dhule, S. S., Penfornis, P., Frazier, T., Walker, R., Feldman, J., Tan, G., ... & Pochampally, R. (2012). Curcumin-loaded γ-cyclodextrin liposomal nanoparticles as delivery vehicles for osteosarcoma. *Nanomedicine: Nanotechnology, Biology and Medicine*, *8*(4), 440-451. (b) Chen, Y., Wu, Q.,

Zhang, Z., Yuan, L., Liu, X., & Zhou, L. (2012). Preparation of curcumin-loaded liposomes and evaluation of their skin permeation and pharmacodynamics. *Molecules*, *17*(5), 5972-5987.

[322] Yallapu, M. M., Jaggi, M., & Chauhan, S. C. (2010). β-Cyclodextrin-curcumin self-assembly enhances curcumin delivery in prostate cancer cells. *Colloids and surfaces B: Biointerfaces*, *79*(1), 113-125.

[323] Singh, D. K., Jagannathan, R., Khandelwal, P., Abraham, P. M., & Poddar, P. (2013). In situ synthesis and surface functionalization of gold nanoparticles with curcumin and their antioxidant properties: an experimental and density functional theory investigation. *Nanoscale*, *5*(5), 1882-1893.

[324] Hatamie, S., Akhavan, O., Sadrnezhaad, S. K., Ahadian, M. M., Shirolkar, M. M., & Wang, H. Q. (2015). Curcumin-reduced graphene oxide sheets and their effects on human breast cancer cells. *Materials Science and Engineering: C*, *55*, 482-489.

[325] Di Pietro, P., Forte, G., D'Urso, L., & Satriano, C. The hybrid nanobiointerface between nitrogen-doped graphene oxide and lipid membranes: a theoretical and experimental study. *biological membranes*, *12*, 13.

[326] Cheng, Y. C., Kaloni, T. P., Zhu, Z. Y., & Schwingenschlögl, U. (2012). Oxidation of graphene in ozone under ultraviolet light. *Applied Physics Letters*, *101*(7), 073110.

[327] Hummers Jr, W. S., & Offeman, R. E. (1958). Preparation of graphitic oxide. *Journal of the American Chemical Society*, *80*(6), 1339-1339.

[328] Ren, P. G., Wang, H., Huang, H. D., Yan, D. X., & Li, Z. M. (2014). Characterization and performance of dodecyl amine functionalized graphene oxide and dodecyl amine functionalized graphene/high-density polyethylene nanocomposites: A comparative study. *Journal of Applied Polymer Science*, *131*(2).

[329] Compton, O. C., Dikin, D. A., Putz, K. W., Brinson, L. C., & Nguyen, S. T. (2010). Electrically conductive "alkylated" graphene paper via chemical reduction of amine-functionalized graphene oxide paper. *Advanced Materials*, *22*(8), 892-896.

[330] Ren, P. G., Wang, H., Huang, H. D., Yan, D. X., & Li, Z. M. (2014). Characterization and performance of dodecyl amine functionalized graphene oxide and dodecyl amine functionalized graphene/high-density polyethylene nanocomposites: A comparative study. *Journal of Applied Polymer Science*, *131*(2).

[331] Bourlinos, A. B., Gournis, D., Petridis, D., Szabó, T., Szeri, A., & Dékány, I. (2003). Graphite oxide: chemical reduction to graphite and surface

modification with primary aliphatic amines and amino acids. *Langmuir*, *19*(15), 6050-6055.

[332] D'Urso, L., Satriano, C., Forte, G., Compagnini, G., & Puglisi, O. (2012). Water structure and charge transfer phenomena at the liquid–graphene interface. *Physical Chemistry Chemical Physics*, *14*(42), 14605-14610.

[333] Eda, G.; Lin, Y.Y.; Mattevi, C.; et al. Adv Mater 2010, 22, 505–509.

[334] Dementjev, A. P., De Graaf, A., Van de Sanden, M. C. M., Maslakov, K. I., Naumkin, A. V., & Serov, A. A. (2000). X-ray photoelectron spectroscopy reference data for identification of the C 3 N 4 phase in carbon–nitrogen films. *Diamond and Related Materials*, *9*(11), 1904-1907.

[335] Petit, C., Seredych, M., & Bandosz, T. J. (2009). Revisiting the chemistry of graphite oxides and its effect on ammonia adsorption. *Journal of Materials Chemistry*, *19*(48), 9176-9185.

[336] Mungse, H. P., Singh, R., Sugimura, H., Kumar, N., & Khatri, O. P. (2015). Molecular pillar supported graphene oxide framework: conformational heterogeneity and tunable d-spacing. *Physical Chemistry Chemical Physics*, *17*(32), 20822-20829.

[337] Satriano, C., Svedhem, S., & Kasemo, B. (2012). Well-defined lipid interfaces for protein adsorption studies. *Physical Chemistry Chemical Physics*, *14*(48), 16695-16698.

[338] Axelrod, D., Koppel, D. E., Schlessinger, J., Elson, E., & Webb, W. W. (1976). Mobility measurement by analysis of fluorescence photobleaching recovery kinetics. *Biophysical journal*, *16*(9), 1055-1069.

[339] Satriano, C., Marletta, G., & Kasemo, B. (2008). Oxygen plasma-induced conversion of polysiloxane into hydrophilic and smooth SiOx surfaces. *Surface and Interface Analysis*, *40*(3-4), 649-656.

[340] Tsukamoto, M., Kuroda, K., Ramamoorthy, A., & Yasuhara, K. (2014). Modulation of raft domains in a lipid bilayer by boundary-active curcumin. *Chemical Communications*, *50*(26), 3427-3430.

[341] Giannakoudakis, D. A., & Bandosz, T. J. (2014). Zinc (hydr) oxide/graphite oxide/AuNPs composites: Role of surface features in H 2 S reactive adsorption. *Journal of colloid and interface science*, *436*, 296-305.

[342] Kuila, T., Bose, S., Mishra, A. K., Khanra, P., Kim, N. H., & Lee, J. H. (2012). Chemical functionalization of graphene and its applications. *Progress in Materials Science*, *57*(7), 1061-1105.

[343] Vesali-Naseh, M., Mortazavi, Y., Khodadadi, A. A., Parsaeian, P., & Moosavi-Movahedi, A. A. (2013). Plasma thiol-functionalized carbon nanotubes decorated with gold nanoparticles for glucose biosensor. *Sensors and Actuators B: Chemical*, *188*, 488-495.

[344] Humeres, E., Debacher, N. A., Smaniotto, A., de Castro, K. M., Benetoli, L. O., de Souza, E. P., ... & Santaballa, J. A. (2014). Selective Insertion of Sulfur Dioxide Reduction Intermediates on Graphene Oxide. *Langmuir*, *30*(15), 4301-4309.

[345] (a) Jiang, Z., Xia, D., Li, Y., Li, J., Li, Q., Chen, M., ... & Dong, M. (2013). Facilitating the mechanical properties of a high-performance pH-sensitive membrane by cross-linking graphene oxide and polyacrylic acid. *Nanotechnology*, *24*(33), 335704. (b) Li, Z., Shen, J., Ma, H., Lu, X., Shi, M., Li, N., & Ye, M. (2013). Preparation and characterization of pH-and temperature-responsive nanocomposite double network hydrogels. *Materials Science and Engineering: C*, *33*(4), 1951-1957.

[346] Liu, S., Hu, M., Zeng, T. H., Wu, R., Jiang, R., Wei, J., ... & Chen, Y. (2012). Lateral dimension-dependent antibacterial activity of graphene oxide sheets. *Langmuir*, *28*(33), 12364-12372.

[347] Xu, M., Zhu, J., Wang, F., Xiong, Y., Wu, Y., Wang, Q., ... & Liu, S. (2016). Improved in vitro and in vivo biocompatibility of graphene oxide through surface modification: poly (acrylic acid)-functionalization is superior to PEGylation. *ACS nano*, *10*(3), 3267-3281.

[348] Hlady, V., & Buijs, J. (1996). Protein adsorption on solid surfaces. *Current Opinion in Biotechnology*, *7*(1), 72-77.

[349] (a) Dockal, M., Carter, D. C., & Rüker, F. (1999). The three recombinant domains of human serum albumin structural characterization and ligand binding properties. *Journal of Biological Chemistry*, *274*(41), 29303-29310.; (b) He, X. M., & Carter, D. C. (1992). Atomic structure and chemistry of human serum albumin.

[350] Elzoghby, A. O., Samy, W. M., & Elgindy, N. A. (2012). Albumin-based nanoparticles as potential controlled release drug delivery systems. *Journal of Controlled Release*, *157*(2), 168-182.

[351] Xiong, H., Guo, Z., Zhang, W., Zhong, H., Liu, S., & Ji, Y. (2014). Redox-responsive biodegradable PEGylated nanographene oxide for efficiently chemo-photothermal therapy: A comparative study with non-biodegradable PEGylated nanographene oxide. *Journal of Photochemistry and Photobiology B: Biology*, *138*, 191-201.

[352] Bertucci, C., Cimitan, S., Riva, A., & Morazzoni, P. (2006). Binding studies of taxanes to human serum albumin by bioaffinity chromatography and circular dichroism. *Journal of pharmaceutical and biomedical analysis*, *42*(1), 81-87.

[353] John, T. A.; Vogel, S. M. Tiruppathi, C.; Malik, A. B. and Minshall, R. D. Am. J. Physiol.: Lung Cell. Mol. Physiol., 2003, 284, 187.

[354] Basu, N., Bhattacharya, R., & Mukherjee, P. (2008). Protein-mediated autoreduction of gold salts to gold nanoparticles. *Biomedical Materials*, *3*(3), 034105.

[355] Liu, J., Fu, S., Yuan, B., Li, Y., & Deng, Z. (2010). Toward a universal "adhesive nanosheet" for the assembly of multiple nanoparticles based on a protein-induced reduction/decoration of graphene oxide. *Journal of the American Chemical Society*, *132*(21), 7279-7281.

[356] Wu, S., Zhao, X., Li, Y., Du, Q., Sun, J., Wang, Y., ... & Xia, L. (2013). Adsorption properties of doxorubicin hydrochloride onto graphene oxide: equilibrium, kinetic and thermodynamic studies. *Materials*, *6*(5), 2026-2042.

[357] Cheon, Y. A., Bae, J. H., & Chung, B. G. (2016). Reduced graphene oxide nanosheet for chemo-photothermal therapy. *Langmuir*, *32*(11), 2731-2736.

[358] Wang, W. N., & He, X. (2016). Aerosol processing of crumpled graphene oxide-based nanocomposites for drug delivery. *Current pharmaceutical design*, *22*(17), 2491-2500.

[359] Ma, N., Liu, J., He, W., Li, Z., Luan, Y., Song, Y., & Garg, S. (2017). Folic acid-grafted bovine serum albumin decorated graphene oxide: An efficient drug carrier for targeted cancer therapy. *Journal of Colloid and Interface Science*, *490*, 598-607..

[360] Cheon, Y. A., Bae, J. H., & Chung, B. G. (2016). Reduced graphene oxide nanosheet for chemo-photothermal therapy. *Langmuir*, *32*(11), 2731-2736.

[361] P. Di Pietro, G. Consiglio, L. D'Urso, G. Forte, G. Grasso, C. Sgarlata, D. Cossement, R. Snyders, C. Satriano. (2017) Lateral-size controlled graphene oxide functionalised by polyacrylate grafting: an experimental and theoretical study for applications in theranostics. Submitted to *RSC Advances*.

[362] Qi, X., Zhou, T., Deng, S., Zong, G., Yao, X., & Fu, Q. (2014). Size-specified graphene oxide sheets: ultrasonication assisted preparation and characterization. *Journal of Materials Science*, *49*(4), 1785-1793.

[363] Yang, K., Li, Y., Tan, X., Peng, R., & Liu, Z. (2013). Behavior and toxicity of graphene and its functionalized derivatives in biological systems. *Small*, *9*(9-10), 1492-1503.

[364] Lai, Q., Zhu, S., Luo, X., Zou, M., & Huang, S. (2012). Ultraviolet-visible spectroscopy of graphene oxides. *AIP Advances*, *2*(3), 032146.

[365] Mermoux, M., Chabre, Y., & Rousseau, A. (1991). FTIR and 13C NMR study of graphite oxide. *Carbon*, *29*(3), 469-474.

[366] Hummers Jr, W. S., & Offeman, R. E. (1958). Preparation of graphitic oxide. *Journal of the American Chemical Society*, *80*(6), 1339-1339.

[367] Yumitori, S. (2000). Correlation of C1s chemical state intensities with the O1s intensity in the XPS analysis of anodically oxidized glass-like carbon samples. *Journal of materials science*, *35*(1), 139-146.

[368] Dietrich, P. M., Hennig, A., Holzweber, M., Thiele, T., Borcherding, H., Lippitz, A., ... & Unger, W. E. (2014). Surface analytical study of poly (acrylic acid)-grafted microparticles (beads): characterization, chemical derivatization, and quantification of surface carboxyl groups. *The Journal of Physical Chemistry C*, *118*(35), 20393-20404.

[369] Yang, D., Velamakanni, A., Bozoklu, G., Park, S., Stoller, M., Piner, R. D., ... & Ruoff, R. S. (2009). Chemical analysis of graphene oxide films after heat and chemical treatments by X-ray photoelectron and Micro-Raman spectroscopy. *Carbon*, *47*(1), 145-152.

[370] Li, X., Wang, H., Robinson, J. T., Sanchez, H., Diankov, G., & Dai, H. (2009). Simultaneous nitrogen doping and reduction of graphene oxide. *Journal of the American Chemical Society*, *131*(43), 15939-15944.

[371] Louette, P., Bodino, F., & Pireaux, J. J. (2005). Poly (acrylic acid)(PAA) XPS reference core level and energy loss spectra. *Surface Science Spectra*, *12*(1), 22-26.

[372] Lai, Q., Zhu, S., Luo, X., Zou, M., & Huang, S. (2012). Ultraviolet-visible spectroscopy of graphene oxides. *AIP Advances*, *2*(3), 032146.

[373] Wang, W. N., & He, X. (2016). Aerosol processing of crumpled graphene oxide-based nanocomposites for drug delivery. *Current pharmaceutical design*, *22*(17), 2491-2500.

[374] Li, S., Aphale, A. N., Macwan, I. G., Patra, P. K., Gonzalez, W. G., Miksovska, J., & Leblanc, R. M. (2012). Graphene oxide as a quencher for fluorescent assay of amino acids, peptides, and proteins. *ACS applied materials & interfaces*, *4*(12), 7069-7075.

PAPER I

Neurotrophin-mimicking peptides at the biointerface with gold respond to copper ions stimuli.

C. Satriano, G. Forte, A. Magrì, P. Di Pietro, A. Travaglia, G. Pandini, F. Gianì, D. La Mendola. *PCCP,* 2016, 18, 30595-30604.

PCCP

View Article Online
DOI: 10.1039/C6CP05476E

ARTICLE

Neurotrophin-mimicking peptides at the biointerface with gold respond to copper ions stimuli

Received 00th January 20xx,
Accepted 00th January 20xx

DOI: 10.1039/x0xx00000x

www.rsc.org/

C. Satriano,[a*] G. Forte,[b] A. Magrì,[c] P. Di Pietro,[a] A. Travaglia,[d] G. Pandini,[e] F. Gianì[e] and D. La Mendola[f,*]

The peptide fragments NGF_{1-14} and $BDNF_{1-12}$, encompassing the N-terminal domains respectively of the proteins nerve growth factor (NGF) and brain-derived neurotrophic factor (BDNF) respectively, were used in this study for the fabrication of a hybrid gold/peptide biointerface. These peptides mimic the Trk receptor activation of the respective whole protein - with a crucial role played by copper ions – and exhibit, in bulk solution, a pH-dependent capability to complex copper. We demonstrate here the maintenance of peptide-specific responses on different pH values as well as in the copper binding also for the adlayers formed upon physisorption at the gold surface. The physicochemical properties, including viscoelastic behavior of the adlayer and competitive *vs.* synergic interactions in sequential adsorption processes were addressed both experimentally, by quartz crystal microbalance with dissipation monitoring (QCM-D), circular dichroism (CD), and theoretically, by molecular dynamics (MD) calculations. Proof-of work biological assays with the neuroblastoma SY-SH5H cell line demonstrated that the developed hybrid Au/peptide nanoplatforms are very promising for the implementation into pH- and metal-responsive systems for application in nanomedicine.

1. Introduction

The assembling of hybrid nano-biointerfaces is very promising for biomaterial science, nanomedicine and biosensors.[1, 2]
In particular, the use of a metal surface at the biointerface[3] offers several advantages in the initial phases of design, surface engineering[4] and then the investigation of the material-biological environment interactions.[5]
Gold surfaces are extensively used as biomaterial for (bio)molecule immobilization, via either covalent or non-specific physisorption interactions.[6] Additionally, gold nanoparticles are a great promise as therapeutic delivery vectors and intracellular imaging agents.[7, 8]
Neurotrophin proteins are essential for the neuronal maintenance and to modulate synaptic transmission.[9] Among them, Nerve Growth Factor (NGF) and the Brain-Derived Neurotrophic Factor (BDNF) are the most studied and have recently gained interest as therapeutic agent for neurological pathologies, such as schizophrenia and Alzheimer's disease.[10, 11]

The N-terminal domains of NGF and BDNF are critical for the selective binding and activation of their cognate TrK receptor, TrkA and TrkB, respectively. These receptors are involved in triggering pro-survival signalling cascade.[12, 13]
Following a peptidomimetic approach,[14] we use herein two peptides, NGF_{1-14} and $BDNF_{1-12}$, which encompass the N-terminal sequence of their respective whole protein, and mimic their biological activity.
For example, NGF_{1-14} has been recently demonstrated to have an effective and specific NGF-like action on some crucial intermediates of the whole protein intracellular targets, such as Akt and the transcription factor cAMP response element-binding protein (CREB).[15] The aptitude of NGF_{1-14}[16] and $BDNF_{1-12}$[17] peptides to specifically bind TrK receptors suggests their potential use as drugs, to overcome the current pharmacological limits and side effects of the related NGF and BDNF whole proteins, including the activation of p75 receptor and its pro-apoptotic signalling cascade, and the painful administration.[18]
Another interesting property that both NGF_{1-14} and $BDNF_{1-12}$ exhibit is their capability of response to the stimulus induced by copper addition.[16, 17]
Noteworthy, a strong decrease of the proliferative activity of both $BDNF_{1-12}$ and the whole protein on a SY-SH5H neuroblastoma cell line was found after treatment in the presence of Cu^{2+}.[17] The effect of metal addition is opposite to that observed for the analogous fragment of NGF protein,

[a.] Department of Chemical Sciences, University of Catania, Viale Andrea Doria, 6. I-95125 Catania, Italy.
[b.] Department of Pharmaceutical Sciences, University of Catania, Viale Andrea Doria, 6. I-95125 Catania, Italy.
[c.] Institute of Biostructures and Bioimages – Catania, National Council of Research (IBB-CNR), Via Paolo Gaifami, 16, I-95125 Catania, Italy.
[d.] Centre for Neural Science, New York University, Washington Place, 4. New York, NY 10003, USA.
[e.] Endocrinology, Department of Clinical and Experimental Medicine, Garibaldi-Nesima Medical Center, University of Catania, via Palermo n. 636, 95122 Catania, Italy.
[f.] Department of Pharmacy, University of Pisa, via Bonanno Pisano, 6. I-56100 Pisa, Italy.
* Corresponding authors: csatriano@unict.it ; lamendola@farm.unipi.it
See DOI: 10.1039/x0xx00000x

PAPER II

Lipid bilayer-mediated immobilisation of neurotrophin peptides on gold nanoparticles: a new multipotential therapeutic nanoplatform for CNS disorders.

P. Di Pietro, N. Caporarello, C. D. Anfuso, G. Lupo, A. Magrì, D. La Mendola, C. Satriano. Submitted to *Chem. Comm*.

ChemComm

COMMUNICATION

Immobilisation of neurotrophin peptides on gold nanoparticles by direct and lipid-mediated interaction: a new multipotential therapeutic nanoplatform for CNS disorders

Received 00th January 20xx,
Accepted 00th January 20xx

DOI: 10.1039/x0xx00000x

www.rsc.org/

P. Di Pietro,[a] N. Caporarello,[b] C. Daniela A.,[b] G. Lupo,[b] A. Magrì,[c] D. La Mendola[d]*, C. Satriano,[a]*

In this work we demonstrate, for the first time, an efficient and tunable approach for the functionalisation of gold nanoparticles with neurotrophin-mimicking peptides; the promising potentialities in theranostics and the capability to cross the blood brain barrier are addressed.

Nanoparticle-based platforms are nowadays attracting a great deal for the delivery of drugs and molecules with neuroprotective and regenerative activity that, in normal conditions, would not be able passing the blood brain barrier (BBB). Neurotrophin proteins, produced by cells of the central nervous system (CNS), are growth factors regulating the neuron division, survival, and neurite outgrowth.[1, 2] A forefront research area deals with making neurotrophins a clinical realness for people suffering from disorders involving neuronal degeneration (such as Alzheimer's, Huntington's, and Parkinson's Disease)[3], and physical trauma resulting in the severing of nerve connections (i.e., accidents and sports-related injuries).[4] Some neurotrophins are already licensed for use in humans, for administering opioids for chronic pain management and in antisplasticity drugs for spinal cord injury.[4] Notwithstanding their great potentialities in the therapeutic action, their clinical application has been limited owing to their poor plasma stability and penetration in the BBB, and serious side effects, such as pain.[5, 6]

A promising strategy involves new hybrid systems comprising both peptides able to mimic neurotrophins by retaining the functionality of neurotrophic action,[7] and nanoparticles that can transport the drugs adsorbed or bound covalently to them.[8] In such a way the drug delivery and the ability to cross the BBB can be finely controlled over their size, surface charge, hydrophobicity, shape, coating, and chemistry.[9-11]

We recently demonstrated that peptide sequences encompassing the N-terminal domain of nerve growth factor (NGF) and brain-derived neurotrophic factor (BDNF) exhibit neurotrophin-mimicking capabilities also upon immobilisation on solid gold surface.[12, 13] In the present work, we move a step forward on the fabrication and biological validation of the hybrid nanobio interface established between neurotrophin peptides and gold nanoparticles (AuNPs), which represent an attractive scaffold to construct a multifaceted drug delivery platform (Scheme 1).

AuNPs have intrinsic anti-angiogenic and anti-inflammatory activities;[14] owing to their plasmonic properties, they are suitable for light-triggered response (*e.g.*, hyperthermia in tumour treatment) and optical imaging (biosensing).[14] Moreover, drug-functionalised AuNPs might be able to cross the BBB and to allow for a target-specific delivery of the active molecules to the neurons of the CNS.[11] To enhance the image-contrast capability of the theranostic platform, the NGF- and BDNF-like peptides were dye-labelled with carboxyfluorescein (Fam) through an additional lysine (K) residue at the C-terminus, to obtain SSSHPIFHRGEFSV-K-Fam (NGFpF) and HSDPARRGELSV-K-Fam (BDNFpF), respectively.

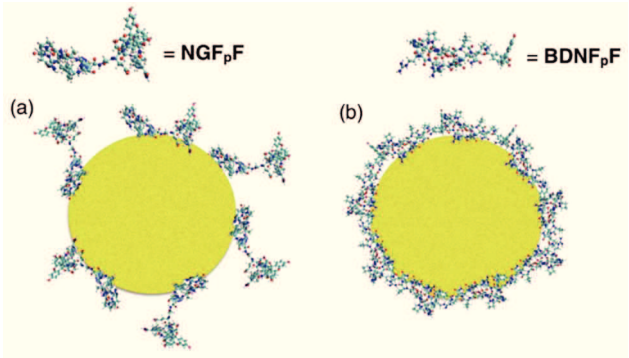

Scheme 1- Representative picture of the hybrid gold nanoparticle-peptide interface for NGF$_p$F (a) and BDNF$_p$F (b) peptides.

[a] Department of Chemical Sciences, University of Catania, Viale Andrea Doria, 6, 95125 Catania, Italy. E-mail: csatriano@unict.it
[b] Department of Biomedical and Biotechnological Sciences, University of Catania, Viale Andrea Doria, 6, 95125 Catania, Italy
[c] Institute of Biostructures and Bioimages – Catania, National Council of Research (IBB-CNR), Via Paolo Gaifami, 16, I-95125 Catania, Italy
[d] Department of Pharmacy, University of Pisa, via Bonanno Pisano, 6, I-56100 Pisa, Italy. E-mail: lamendola@farm.unipi.it

† Electronic Supplementary Information (ESI) available: a) Experimental details. b) Figure S0-S2, centrifugation and UV-visible analyses; Figure S3, AFM analysis; Table S1 and Figure S4, XPS analysis; Figure S5 cell viability assay. See DOI: 10.1039/x0xx00000x

PAPER IV

Silver nanoparticles functionalized with a fluorescent cyclic RGD peptide: a versatile integrin targeting platform for cells and bacteria.

P. Di Pietro, L. Zaccaro, D. Comegna, A. Del Gatto, M. Saviano, R. Snyders, D. Cossement, C. Satriano, E. Rizzarelli. *RSC Adv*. 2016, 6, 112381-112392.

RSC Advances

PAPER

View Article Online
View Journal | View Issue

Cite this: *RSC Adv.*, 2016, **6**, 112381

Silver nanoparticles functionalized with a fluorescent cyclic RGD peptide: a versatile integrin targeting platform for cells and bacteria†

P. Di Pietro,[a] L. Zaccaro,[b] D. Comegna,[b] A. Del Gatto,[b] M. Saviano,[c] R. Snyders,[de] D. Cossement,[e] C. Satriano*[a] and Enrico Rizzarelli[af]

Received 28th August 2016
Accepted 18th November 2016

DOI: 10.1039/c6ra21568h

www.rsc.org/advances

The arginine–glycine–aspartic acid (RGD) peptide sequence is known to specifically interact with integrins, which are chief receptors participating at various stages of cancer disease and in bacterial adhesion/invasion processes. In particular, vitronectin receptor ($\alpha_v\beta_3$) and fibronectin receptor ($\alpha_5\beta_1$) integrins are involved respectively in tumour cell targeting and bacteria internalization inhibition. Silver nanoparticles (AgNPs) have elicited a lot of interest as a theranostic platform, owing to their unique optoelectronic as well as self-therapeutic properties as bactericides. The goal of this work was the comprehensive physicochemical characterization of a hybrid peptide–metal nanoparticle biointerface fabricated by the immobilisation, through thiol chemistry, of a fluorescent cyclic RGD peptide onto AgNPs of 13 nm diameter. RGD peptide-functionalized AgNPs were investigated by a multi-technique approach, including various spectroscopic (XPS, FTIR and UV-visible), spectrometric (ToF-SIMS) and microscopic (SEM, TEM, AFM) methods as well as dynamic light scattering and ζ-potential measurements. Proof-of-work experiments by confocal microscopy imaging of the cellular uptake by human neuroblastoma SH-SY5Y and chronic myelogenous leukaemia K562 cells, overexpressing respectively $\alpha_v\beta_3$ and $\alpha_5\beta_1$ integrins, demonstrated a receptor-specific activity of the RGD peptide-functionalised AgNPs, which make them very promising as a multifaceted platform in applications with cells and bacteria.

1 Introduction

Multifunctional nanoparticles (NPs) offer great promise for early diagnosis and targeted therapy, which is a hot area of nanomedicine.[1] Nanomaterials, owing to their extremely high surface-to-volume ratio, offer an ideal versatile platform for polyvalent presentation on account of their tunable size and shape, surface chemistry, biocompatibility and, in general, non-toxicity. Furthermore, an increased ability of targeting and efficiency of drug loading/release as well as image contrast capability, for instance, due to their optical or magnetic properties, are major advantages of nanoparticles for theranostic applications.[2,3]

An enormous research effort has been devoted to the search for suitable materials to achieve targeted delivery, for example polymers/inorganic mesoporous nanoparticles,[4] hollow nanocapsules based on polymers,[5,6] liposomes,[7] inorganic metals and oxides.[8]

In particular, metal NPs, with their unique optoelectronic properties[9] as well as their self-therapeutics features, including anti-angiogenic gold nanoparticles (AuNPs) and antibacterial silver nanoparticles (AgNPs),[10] attract a large interest as ideal candidates for tumour diagnosis and therapy.[3,11]

Different functionalization and/or surface modification strategies, including the surface-anchoring of protein-mimicking peptides as bioactive moieties,[12–14] can be used to trigger the response of a solid surface at the hybrid biointerface, thus modulating the interaction with lipid membranes,[15–17] mammalian cells[18–20] or bacteria.[21–23]

Surface-engineered nanoparticles may intrude cells by active targeting but also by passive penetration of the plasma membrane.[24] Nanoparticles adhere to and penetrate cell

[a]*Department of Chemical Sciences, University of Catania, Consorzio Interuniversitario di Ricerca in Chimica dei Metalli nei Sistemi Biologici (C.I.R.C.M.S.B.), viale Andrea Doria 6, 95125 Catania, Italy. E-mail: csatriano@unict.it; Tel: +39 0957385136*

[b]*Institute of Biostructure and Bioimaging (IBB) of the Italian National Research Council (CNR), Via Mezzocannone, 16, Napoli, Italy*

[c]*Institute of Crystallography (IC) of the Italian National Research Council (CNR), Via Amendola 122/O, 70126, Bari, Italy*

[d]*Chimie des Interactions Plasma Surface (ChIPS), Research Institute for Materials Science and Engineering, Université de Mons (UMONS), Belgium*

[e]*Materia Nova Research Center, 1, Avenue Copernic, 7000 Mons, Belgium*

[f]*Institute of Biostructure and Bioimaging (IBB) of the Italian National Research Council (CNR), 18, Via Paolo Gaifami 18, Catania, Italy*

† Electronic supplementary information (ESI) available: Fig. S1: UV-visible spectra of AgNP and peptide–AgNP upon NaCl addition; Fig. S2: FT-IR analysis of hybrid AgNP/peptide systems compared to the reference peptides and bare AgNPs; Table S1: surface atomic composition of bare and peptide-functionalized AgNPs; Fig. S3: positive ToF-SIMS spectra; Table S2: significant peaks from PCA analysis of negative ToF-SIMS spectra. Fig. S4: fluorescence spectra. See DOI: 10.1039/c6ra21568h

PAPER V

The hybrid nanobiointerface between amine-functionalized graphene oxide and lipid membranes: a theoretical and experimental study.

P. Di Pietro, G. Forte, L. D'Urso, C. Satriano.
Special topic "Graphene" - AIMS Materials Science 2017, 4(1), 43-60.

AIMS Materials Science, 4(1): 43-60.
DOI: 10.3934/matersci.2017.1.43
Received: 31 October 2016
Accepted: 15 December 2016
Published: 21 December 2016

http://www.aimspress.com/journal/Materials

Research article

The hybrid nanobiointerface between nitrogen-doped graphene oxide and lipid membranes: a theoretical and experimental study

P. Di Pietro [1], G. Forte [2,*], L. D'Urso [3], and C. Satriano [1,*]

[1] Nanobiohybrid Interfaces Laboratory (NIL), Department of Chemical Sciences, University of Catania, Viale Andrea Doria, 6, I-95125 Catania, Italy
[2] Department of Pharmaceutical Sciences, University of Catania, Viale Andrea Doria, 6, I-95125 Catania, Italy
[3] Department of Chemical Sciences, University of Catania, Viale Andrea Doria, 6, I-95125 Catania, Italy

* **Correspondence:** Email: gforte@unict.it; csatriano@unict.it.

Abstract: In this study, we present a comparison between graphene oxide (GO) and nitrogen-doped GO (N-GO) in terms of spectroscopic properties and biomolecule-binding potentiality features. Specifically, GO nanosheets, both in aqueous dispersion and in solid state, were successfully modified with different amino-containing moieties, in order to obtain graphene-based nanostructures able to respond to chemical stimuli (e.g., pH) and with tunable surface properties. The physisorption of dye-labelled lipid vesicles loaded with curcumin, was scrutinised both theoretically and experimentally. The energetics of the hybrid lipid membrane-curcumin-GO interface at different pH values, representative respectively of physiological (7.4) and pathological (5.5) environment, were estimated by molecular dynamics (MD) simulations. The GO and GO-N samples characterization by Raman, fluorescence, and UV-vis spectroscopies, as well as confocal microscopy demonstrated promising features of the (N-)GO/lipid platforms for fluorescence imaging and drug delivery applications.

Keywords: 2D nanomaterials; supported lipid bilayers; surface functionalisation; molecular dynamics; confocal microscopy

PAPER VI

Lateral-size controlled graphene oxide functionalised by polyacrylate grafting: an experimental and theoretical study for applications in theranostics.

G. Consiglio, P. Di Pietro, L. D'Urso, G. Forte, G. Grasso, C. Sgarlata, D. Cossement, R. Snyders, C. Satriano. Submitted to *RSC Advances*

RSC Advances

ARTICLE

Tuning the response of graphene oxide at the biointerface for theranostic applications

Received 00th January 20xx,
Accepted 00th January 20xx

DOI: 10.1039/x0xx00000x

www.rsc.org/

G. Consiglio,[a‡] P. Di Pietro, [a‡] L. D'Urso,[a*] G. Forte,[b] G. Grasso,[a] C. Sgarlata,[a] D. Cossement,[c] R. Snyders[c,d] and C. Satriano[a*]

A facile strategy of polyacrylate (PAA) grafting was used to develop a pH stimuli-responsive theranostic platform based on graphene oxide (GO) nanosheets of homogeneous size. Indeed, the GO lateral size was found to significantly affect its surface charge, optical properties as well as the cellular uptake. The actual surface termination of the GO/polymer hybrid, prepared at two different acrylate grafting ratios, was scrutinised by a multitechnique approach, including spectroscopic (UV-visible, fluorescence, Raman, ATR-FTIR, XPS), spectrometric (ToF-SIMS and –for the first time- ESI-MS) and microscopic (AFM, confocal microscopy) methods. Both theoretical and experimental investigations on the optical response of water/GO and water/GO-PAA interface, at different pH values, showed that the platform could be used not only to exploit a pH-triggered drug release but also for a modulation of the GO intrinsic emission properties. Fluorescence resonance energy transfer (FRET) experiments in solution of the graphene oxide/fluorescein-labelled albumin/doxorubicin assembly showed significant differences for GO and GO-PAA, thus demonstrating the occurrence of different electronic processes at the hybrid nano-bio-interfaces. Confocal microscopy studies of cellular uptake in neuroblastoma cells confirmed the promising potentialities of the developed nanoplatform for theranostics.

1. Introduction

The main text of the article should appear here with headings as appropriate. Two-dimensional graphene-related materials have shown great potential for biomedical engineering applications, especially bioimaging[1] and tissue engineering,[2] due their unique physicochemical characteristics, including optoelectronic properties, mechanical strength, and biocompatibility.[3]

In particular, graphene oxide (GO) is increasingly used in biomedical applications because it possesses not only the unique graphene properties of large surface area and flexibility but also hydrophilicity and dispersibility in aqueous solutions.[4] GO has been proposed as an effective antibacterial agent in commercial packaging,[5] capable of generating synergistic topographical stimulation to enhance integrin clustering, focal adhesion, and neuronal differentiation in human neural stem cells,[6] as electrochemical biosensor for cancer diagnosis[7] and as alternative to metal nanocarriers[8] for targeted drug delivery[9] and tumour microenvironment-responsive triggered drug release.[10]

Doxorubicin hydrochloride (DOX) is an effective anticancer agent for leukemia chemotherapy but its clinical use has been limited because of side effects; thus, its delivery by various nanoparticles has been largely investigated.[11-13] GO and reduced GO (rGO) have been already demonstrated to be promising nanocarriers for DOX. Thermodynamic studies indicated that the adsorption of DOX on GO is spontaneous and endothermic in nature.[13]

Recently, a prostate cancer-targeted GO, grafted with dendrimers capped with amino groups and loaded with DOX was demonstrated very effective for magnetic resonance imaging and drug delivery.[14] Also, *in vitro* cell cytotoxicity and cellular uptake studies of folic acid-albumin/GO/DOX assembly suggested that the nanohybrids construct significantly enhanced the anticancer activity.[15]

Another popular strategy for the imaging properties of GO is fluorescence, which arises from the radiative recombination of electron–hole pairs among the confined cluster originating from the small and isolated sp^2 carbon domains embedded in the sp^3 matrix.[16] Poly(N-isopropylacrylamide)-grafted graphene oxide loaded with DOX was internalised by cells, as evidenced both from optical and fluorescence imaging of live cells, with a significant improvement of the efficiency of drug in the loaded system.[17] In the same work the authors explain

[a] Department of Chemical Sciences, University of Catania, viale Andrea Doria 6, 95125 Catania, Italy.
[b] Department of Pharmaceutical Sciences, University of Catania, viale Andrea Doria 6, 95125 Catania, Italy.
[c] Materia Nova Research Center, Avenue Copernic 1, 7000 Mons, Belgium.
[d] Chimie des Interactions Plasma Surface (ChIPS), Research Institute for Materials Science and Engineering, Université de Mons, 7000 Mons, Belgium.
‡ These authors contributed equally.
* Correspondence to: Luisa D'Urso, tel. +39 (0)957385129, e-mail: ldurso@unict.it; Cristina Satriano, tel. +39 (0)957385136, e-mail: csatriano@unict.it

Electronic Supplementary Information (ESI) available: [TGA of pristine and sonicated GO (Figure S1). Characterisation of GO and GO-PAA by: significant ToF-SIMS peaks from PCA (Table S1); peaks assignment of ESI-MS spectra (Table S2); TGA (Figure S2); zeta potential (Figure S3); UV-vis characterisation of response to pH and ionic strength stimuli (Figures S4-S7); ATR/FTIR and Raman spectra (Figure S8); XPS characterisation (Figure S9, Tables S3-S4); excitation spectra for the FRET experiments (Figure 10).]. See DOI: 10.1039/x0xx00000x

PAPER VII

Gold and Silver Nanoparticles for Applications in Theranostics. *Review*

P. Di Pietro, G. Strano, L. Zuccarello, C. Satriano.
Curr. Top. Med. Chem., 2016, 16 (27), 3069-3102.

Current Topics in Medicinal Chemistry, 2016, *16*, 3069-3102

REVIEW ARTICLE

Gold and Silver Nanoparticles for Applications in Theranostics

Patrizia Di Pietro[a], Gaetano Strano[b], Lidia Zuccarello[a] and Cristina Satriano[a,*]

[a]*Department of Chemical Sciences, University of Catania, viale Andrea Doria, 6, 95125 Catania, Italy;* [b]*Ri.MED Foundation, Via Bandiera 11, 90133 Palermo, Italy*

ARTICLE HISTORY

Received: April 24, 2016
Revised: June 14, 2016
Accepted: June 16, 2016

DOI: 10.2174/1568026616666160715163346

Abstract: Noble metal nanomaterials, such as gold or silver nanoparticles, exhibit unique photonic, electronic, catalytic and therapeutic properties. The high versatility in their synthesis, especially size and shape features, as well as in the surface functionalization by, *e.g.,* physisorption, direct chemisorption of thiol derivatives and covalent binding through bifunctional linkers or specific affinity interactions, prompted their widespread and rising use as multifunctional platforms for theranostic purposes. In this paper, the recent developments of gold and silver nanoparticles for application in biosensing, medical imaging, diagnosis and therapy is reviewed from the following five aspects: (1) the gold and silver nanomaterials intrinsic properties of biomedical interest; (2) the synthesis of noble metal nanoparticles by chemical, physical and biological/green processes; (3) the applications of gold and silver nanoparticles in imaging, diagnostic and therapeutic mode; (4) the surface functionalization processes for targeting, controlled drug loading and release, triggered pathways of cellular uptake and tissue distribution; and (5) nanotoxicity. The historical developments and the most recent applications have been focused on, together with suggested strategies for future more efficacious, targeted delivery.

Cristina Satriano

Keywords: Drug delivery, Imaging, Metal nanoparticle, Nanomaterial synthesis, Nanotoxicity, Plasmonics, Surface functionalization.

1. INTRODUCTION

Recent advances in nanotechnology have stimulated huge advances in nanomedicine, where nanoparticles (NPs) are employed as versatile platform with a variety of biomedical applications, such as highly sensitive diagnostic assays [1,2] thermal ablation and radiotherapy [3], non-toxic carriers for drugs and gene delivery [4-6]. Often, the goal is to construct multifunctional structures that simultaneously combine the therapeutic capability with imaging and sensing properties, known as "theranostics" [7].

Noble metal NPs, particularly gold (AuNP) and silver (AgNP), have elicited a lot of interest as model theranostic platforms owing to their apparently low toxicity [8], ease of synthesis [9] and versatility in functionalization with various moieties [10] (including antibodies [11], peptides [12] and DNA/RNA [5]) to get specific cell targeting [13] or coating with biocompatible polymers such as polyethylene glycol (PEG) to prolong *in vivo* circulation [14]. Recent investigations are demonstrating another promising application of gold and silver nanomaterials as self-therapeutics [3].

Nanomaterials exhibit completely new or improved properties, compared to bulk of the same chemical composition. Their extremely small size and the higher surface-to-volume ratio with decreasing the size lead to chemical, physical and biological differences in their properties [15]. Metal nanoparticles exhibit size and shape-dependent properties [16] that are of interest for applications ranging from chemical sensing [17] and biosensing [18] to catalysis [19], optics [20], antimicrobial activity [21], computer transistors and wireless electronic logic and memory schemes [22-23]. These particles have also many applications in the specific biomedical field such as for medical imaging [23], nanocomposites [24], drug delivery [25], and hyperthermia of tumours [26]. In particular, the unique modification of the metal surface reactivity by changing the surface-to-volume ratio makes them very attractive for application in the clinical field for cancer therapy [27]. For example, the specific surface area is especially relevant for catalytic reactivity and other related properties, including the antimicrobial activity in silver nanoparticles: as specific surface area of NPs augments, their biological effectiveness normally rises, owing to the increase in surface energy [28].

Site-specific drug delivery is a topic of considerable significance for achieving enhanced therapeutic efficacy and mitigating the adverse side effects. Noble metal NPs can provide theranostic performances, owing to their unique properties for better penetration of therapeutic moieties and tracking within the body, a guided release and a more efficient therapy (with reduced risks) in comparison to conventional therapies [21]. Furthermore, AuNPs and AgNPs are particularly interesting due to their size and shape dependent optoelectronic properties [29,30]. These properties can be easily tuned to desirable wavelengths according to their size (*e.g.,* 1 to 100 nm), shape (*e.g.,* nanospheres, nanowires, nanoshells, nanorods, etc.) and composition (*e.g.,* core/shell

*Address correspondence to this author at the Department of Chemical Sciences, Catania University, P.O. Box: 95125, Catania, Italy; Tel/Fax: ++39-095-7385136; +39-095-580138; E-mail: csatriano@unict.it

1873-5294/16 $58.00+.00